

UNDERSTANDING CLIMATE VARIABILITY AND  
GLOBAL CLIMATE CHANGE USING HIGH-RESOLUTION GCM SIMULATIONS

by

Xuelei Feng  
A Dissertation  
Submitted to the  
Graduate Faculty  
of  
George Mason University  
In Partial fulfillment of  
The Requirements for the Degree  
of  
Doctor of Philosophy  
Climate Dynamics

Committee:

Boh Huang

Dr. Bohua Huang, Dissertation Director

Long S Chiu (BAK)

Dr. Long S. Chiu, Committee Member

Jian Lu (BAK)

Dr. Jian Lu, Committee Member

Paul Dirmeyer

Dr. Paul Dirmeyer, Committee Member

Daniel B. Carr (WFR)

Dr. Daniel B. Carr, Committee Member

Cristiana Stan

Dr. Cristiana Stan, Acting Department Chair

Donna M. Fox

Dr. Donna M. Fox, Associate Dean, Office  
of Student Affairs & Special Programs,  
College of Science

P. Agouris

Dr. Peggy Agouris, Dean, College  
of Science

Date: 07/27/2016

Summer Semester 2016  
George Mason University  
Fairfax, VA

Understanding Climate Variability and Global Climate Change Using High-resolution  
GCM Simulations

A dissertation submitted in partial fulfillment of the requirements for the degree of  
Doctor of Philosophy at George Mason University

By

Xuelei Feng  
Bachelor of Science  
Lanzhou University, 2004

Director: Dr. Bohua Huang, Professor  
Department of Atmospheric, Oceanic, and Earth Sciences

Summer Semester 2016  
George Mason University  
Fairfax, VA

Copyright © 2016 by Xuelei Feng  
All Rights Reserved

## Acknowledgments

I would like to show my acknowledgement to everyone who made this dissertation possible.

First and foremost, I am and will always be forever grateful to my supervisor, Dr. Bohua Huang, for his invaluable guidance and inspirational encouragement. His profound knowledge and patient explanation enable me to develop a good understanding of these subjects. Without him, this dissertation would not have been completed.

I would also like to thank all my committee members: Dr. Long S. Chiu, Dr. Jian Lu, Dr. Paul Dirmeyer, Dr. Daniel B. Carr, for their encouraging words, thoughtful criticism, and valuable time as well as attention.

I am thankful to Jannifer Adams and Thomas Wakefield for their technical support, and many research scientists in COLA for the scientific communications during past few years. Also, thank you to my friends in Climate Dynamics program for helping me and cheering me along the way.

I acknowledge the Department of Atmospheric, Oceanic and Earth Sciences, George Mason University and Center for Ocean-Land-Atmosphere Studies for providing financial support and other necessary resources for completing my doctoral program.

Finally, thanks to my wife, Baohua Chen, my parents and sisters for believing in me and encouraging me to never give up even at those really tough and stressful times. They always stood by my side and kept me strong and positive. I also like to thank my son, my biggest blessing, Johnlin. Thank you for being my motivations, my inspiration! It is because of you I strive to be a better version of myself everyday.

# Table of Contents

	Page
List of Tables . . . . .	vi
List of Figures . . . . .	vii
Abstract . . . . .	xv
1 Motivation . . . . .	1
2 Model simulations and observational data . . . . .	5
2.1 Athena atmospheric simulations . . . . .	5
2.1.1 ECMWF IFS hindcasts runs with different resolutions . . . . .	6
2.1.2 ECMWF IFS AMIP runs with different resolutions . . . . .	7
2.1.3 Time-slice experiments . . . . .	8
2.2 Minerva simulations . . . . .	8
2.3 CCSM3.5 simulations . . . . .	9
2.4 Observational datasets . . . . .	11
3 A multi-model analysis of the resolution influence on precipitation climatology in Gulf Stream region . . . . .	12
3.1 Introduction . . . . .	12
3.2 Precipitation climatology in the Gulf Stream region . . . . .	14
3.2.1 The Athena simulations . . . . .	15
3.2.2 The effects of air-sea coupling . . . . .	23
3.3 Potential mechanisms . . . . .	28
3.3.1 Annual mean pattern . . . . .	30
3.3.2 Summer pattern . . . . .	38
3.4 Summary and discussion . . . . .	43
4 Rainfall frequency and distribution changes associated with global warming in 16 km Athena simulations . . . . .	46
4.1 Introduction of changes in precipitation characteristics in a warm climate . . . . .	46
4.2 Data and analysis method . . . . .	48
4.3 Results . . . . .	48
4.3.1 Latitudinal distribution of precipitation change in amount, intensity and frequency . . . . .	48

4.3.2	Change of precipitation rates in different climatological regions . . .	63
4.4	Summary and discussion . . . . .	70
5	Northern Hemisphere mid-latitude storm track inter-annual variability and seasonal prediction . . . . .	73
5.1	Introduction of NH midlatitude storm track interannual variability . . . . .	73
5.2	Hemispheric patterns of storm track activity: the relationship between the North Pacific and Atlantic basins . . . . .	77
5.3	Sectorial patterns of the storm track activity: connection to the atmospheric low-frequency variability . . . . .	80
5.3.1	Leading modes in individual sectors . . . . .	81
5.3.2	Connections to atmospheric low-frequency variability . . . . .	85
5.4	Northern Hemisphere storm track DJF mean predictability . . . . .	89
5.4.1	Prediction skill and skillful regions . . . . .	90
5.4.2	Potential mechanism of the predictability . . . . .	100
5.5	Summary . . . . .	105
6	Summary . . . . .	108
	Bibliography . . . . .	113

## List of Tables

Table		Page
4.1	Average rain rate (intensity) for each rain category at T159 and T1279 resolution for AMIP and TS simulations . . . . .	53
4.2	Frequency of each rain category at T159 and T1279 for AMIP and TS simulations. Each row sums to 365.2 day . . . . .	54
5.1	Correlation coefficients between first two leading PCs of Minerva T319 and observed four leading PCs of NH DJF mean $vv_{250}$ . . . . .	96

## List of Figures

Figure	Page
<p>3.1 Annual precipitation climatology (unit: mm day<sup>-1</sup>; shading) in the Gulf Stream region (25°N~50°N, 30°W~90°W) from TMPA observations and Athena IFS simulations for 01/1998~11/2008. The superimposed contours are the observed SST (°C)climatology for the same period from the OI-daily observations and the SST climatologies in model simulation panels from their corresponding run outputs. Panel (a) shows the observed mean rainfall derived from TMPA monthly precipitation. The IFS mean precipitations are averaged from the last 12 months of the 13 month hindcast runs initialized at 12Z, November 1 for each year from 01/1998~11/2008. Approximately 12 hindcasts in total are averaged to form the mean state. The IFS hindcasts are conducted with different resolutions from T159 (b), T511 (d) and T1279 (f). The model outputs in these three panels are presented on the same grid network, with the T511 and T1279 output truncated to the Gaussian grid T159. The T511 and T1279 output on their native grids are shown in (c) and (e), respectively. . . . .</p>	15
3.2 As in Fig. 3.1 but for DJF Climatology . . . . .	18
3.3 As in Fig. 3.1 but for MAM Climatology . . . . .	19
3.4 As in Fig. 3.1 but for JJA Climatology . . . . .	20
3.5 As in Fig. 3.1 but for SON Climatology . . . . .	21
<p>3.6 The Climatological annual mean precipitation (shading) and SST (contour) from the Minerva hindcasts for 1980-2011 (left column) and CCSM3.5 (right column). Within the left (right) column, the panels from top downward correspond to the increasing atmospheric (oceanic) resolutions. The contour interval is 2°C and the shading scale is shown on the right . . . . .</p>	23

3.7	(a) Mean SST error of Minerva T319 runs. (b) Mean SST difference between Minerva T639 and T319 (T639-T319), and (c) difference between Minerva T1279 and T639 (T1279-T639). (d) Mean SST error of CCSM LRC07, and (e) CCSM HRC06. (f) Mean SST difference between CCSM HRC06 and LRC07 (HRC06-LRC07) . . . . .	24
3.8	Seasonal precipitation climatology (shading) of Minerva simulations at the resolutions of T319 (left panels), T639 (middle panels) and T1279 (right panels). The color bar of precipitation (unit: mm day <sup>-1</sup> ) is on the right. The seasonal SST climatology (°C; contours) from the corresponding runs is overlaid on each panel. The contour interval is 2°C. Within each column, the seasonal means of DJF, MAM, JJA and SON are organized from top to bottom . . . . .	26
3.9	Seasonal precipitation climatology (unit: mm day <sup>-1</sup> ; shading) from CCSM3.5 LRC07 and HRC06 coupled model simulations. The model corresponding seasonal SST climatologies are superimposed as contours on the corresponding panels. The contour interval is 2°C. The seasonal means for DJF, MAM, JJA and SON are organized from top to bottom panels and LRC07 and HRC06 runs are in the left and right panels, respectively. . . . .	27
3.10	Shading: climatologies of (a) surface convergence (unit: s <sup>-1</sup> ), (b) negative Laplacian of SST (unit: °C m <sup>-2</sup> ), (c) 500-200 hPa divergence (unit: s <sup>-1</sup> ) and (d) SLP Laplacian (unit: Pa m <sup>-2</sup> ) based on ERA-Interim. The corresponding color bar is on the right of each panel. The SST climatology (°C) from ERA-Interim is overlaid as contours in each panel. The contour interval is 2°C. . . . .	30
3.11	Shading: climatologies of (a) surface convergence (unit: s <sup>-1</sup> ), (b) negative Laplacian of SST (°C m <sup>-2</sup> ), (c) 500-200 hPa divergence (unit: s <sup>-1</sup> ) and (d) SLP Laplacian (Unit: Pa m <sup>-2</sup> ) based on Athena T159. The corresponding color bar is on the right of each panel. The SST climatology (°C) from T159 is overlaid by contours in each panel. The contour interval is 2°C. . . . .	31

3.12	Shading: climatologies of (a) surface convergence (unit: $s^{-1}$ ), (b) negative Laplacian of SST (unit: $^{\circ}C\ m^{-2}$ ), (c) 500-200 hPa divergence (unit: $s^{-1}$ ) and (d) the SLP Laplacian (unit: $Pa\ m^{-2}$ ) based on Athena T1279. The corresponding color bar is on the right of each panel. The SST climatology ( $^{\circ}C$ ) from T1279 is overlaid as contours in each panel. The contour interval is $2^{\circ}C$ . . . . .	32
3.13	Shading: climatological differences (Athena T1279-T159) of (a) 500-200 hPa divergence (unit: $s^{-1}$ ), (b) surface convergence (unit: $s^{-1}$ ), (c) the SLP Laplacian (unit: $Pa\ m^{-2}$ ), (d) total precipitation, (e) convective precipitation and (f) stratiform precipitation. The unit of precipitation is (unit: $mm\ day^{-1}$ ). The corresponding color bar is on the right of each panel. The SST climatology ( $^{\circ}C$ ) from T159 is overlaid as contours in each panel. The contour interval is $2^{\circ}C$ . . . . .	33
3.14	Shading: climatology of (a) surface convergence (unit: $s^{-1}$ ), (b) negative laplacian of SST (unit: $^{\circ}C\ m^{-2}$ ), (c) 500-200 hPa divergence (unit: $s^{-1}$ ) and (d) the SLP Laplacian (unit: $Pa\ m^{-2}$ ) based on CCSM3.5 LRC07. The corresponding color bar is on the right of each panel. The model SST climatology ( $^{\circ}C$ ) is overlaid as contours in each panel. The contour interval is $2^{\circ}C$ . . . . .	35
3.15	Shading: climatology of (a) surface convergence (unit: $s^{-1}$ ), (b) negative Laplacian of SST (unit: $^{\circ}C\ m^{-2}$ ), (c) 500-200 hPa divergence (unit: $s^{-1}$ ) and (d) the SLP Laplacian (unit: $Pa\ m^{-2}$ ) based on CCSM3.5 HRC06. The corresponding color bar is on the right of each panel. The model SST climatology ( $^{\circ}C$ ) is overlaid as contours in each panel. The contour interval is $2^{\circ}C$ . . . . .	36

- 3.16 Climatological differences (shadings) between the CCSM3.5 HRC06 and LRC07 simulations. The SST climatology differences ( $^{\circ}\text{C m}^{-2}$ ) are overlaid as contours on all panels. Difference is defined as HRC06-LRC07. The order of this figure is (a) total precipitation climatology (unit:  $\text{mm day}^{-1}$ ), (b) SLP Laplacian (unit:  $\text{Pa m}^{-2}$ ), (c) 1000 hPa convergence (unit:  $\text{s}^{-1}$ ), (d) convective precipitation (unit:  $\text{mm day}^{-1}$ ), (e) negative SST Laplacian (unit:  $^{\circ}\text{C m}^{-2} \text{ m}^{-2}$ ) and (f) 500-200 hPa divergence (unit:  $\text{s}^{-1}$ ). The shading scales are on the right side of their corresponding panels . . . . . 37
- 3.17 The shading in the left panels shows the JJA climatologies of the 500-200 hPa divergence (unit:  $\text{s}^{-1}$ ) for (a) ERA-Interim, (b) Athena T159 and (c) Athena T1279. The corresponding shading scale is on the left of these panels. The shadings in the right panels show the JJA climatologies of the SLP Laplacian (unit:  $\text{Pa m}^{-2}$ ) for (d) ERA-Interim, (e) Athena T159 and (f) Athena T1279. The corresponding shading scale is on the right of these panels. The JJA climatologies of SST the ERA-Interim data and the Athena simulations are superimposed as contours with  $2^{\circ}\text{C}$  interval on the corresponding panels . . . . . 39
- 3.18 Shading: JJA climatological differences (Athena T1279-T159) of (a) 500-200 hPa divergence (unit:  $\text{s}^{-1}$ ), (b) surface convergence (unit:  $\text{s}^{-1}$ ), (c) the SLP Laplacian (unit:  $\text{Pa m}^{-2}$ ), (d) total precipitation, (e) convective precipitation and (f) stratiform precipitation. The unit of precipitation is (unit:  $\text{mm day}^{-1}$ ). The corresponding color bars are on the left side of left panels. The color bar for precipitation is on the right side of the right column. The SST climatology ( $^{\circ}\text{C}$ ) from T159 is overlaid as contours in each panel. The contour interval is  $2^{\circ}\text{C}$  . . . . . 41

3.19	The shading in the left panels shows the JJA climatologies of the precipitation (unit: mm day <sup>-1</sup> ) for (a) TMPA and the NICAM simulation on (b) native resolution and (c) reduced resolution (N80). The corresponding shading scale is on the left of these panels. The shadings in the right panels show the JJA climatologies of (d) 500-200 hPa divergence (unit: s <sup>-1</sup> ), (e) the SLP Laplacian (unit: Pa m <sup>-2</sup> ) and (f) SST Laplacian (unit: Pa m <sup>-2</sup> ) for the NICAM simulation. The corresponding shading scale is on the right of these panels. The JJA climatology of SST from the quarter-degree OISSTv2 data is superimposed as contours with 2°C interval on all panels. The climatology is based on the 9-year average from 2001 to 2009, except for 2003 . . . . .	42
4.1	Climatological mean rainfall for AMIP (color coded) and TS (contours) (a). Their difference (TS-AMIP) is shown in (b). Units mm day <sup>-1</sup> . . . . .	49
4.2	Latitudinal distribution of zonal mean rainfall (mm hr <sup>-1</sup> ) for AMIP (blue) and TS (red) and their difference (in black) . . . . .	50
4.3	Precipitation frequency distribution with intensity in each latitude from AMIP displayed in panel (a), time-slice in panel (b), and time-slice minus AMIP in panel (c). The corresponding frequency accumulation from AMIP demonstrated in panel (d), time-slice in panel (e) and their difference in panel (f)	51
4.4	Probability distribution of rain frequency and rainfall distribution of AMIP and TS simulation from T159 and T1279 (upper). The lower panels show their difference . . . . .	53
4.5	Frequency distribution for non-rain days for AMIP, TS and their difference (TS-AMIP) in day year <sup>-1</sup> . . . . .	56
4.6	Same as 4.5, except for drizzle with rain rate (0-0.1 mm day <sup>-1</sup> ) . . . . .	57
4.7	Same as 4.5, except for light rain with rain rate (0.1-1.2 mm day <sup>-1</sup> ) . . . . .	59
4.8	Same as 4.5, except for moderate rain with rain rate (1.2-15 mm day <sup>-1</sup> ) . . . . .	60
4.9	Same as 4.5, except for heavy rain with rain rate (>15 mm day <sup>-1</sup> ) . . . . .	62

4.10	Frequency of precipitation distribution with intensity in different AMIP climatology regions for AMIP run (a), time-slice (b), and time-slice minus AMIP (c) (shading). The corresponding accumulated distribution of precipitation from different intensity over each AMIP climatological regimes are in (d)-(f). Population percentage is overlaid in panel (c). The fraction of rainfall panel (f) denoted by black lines, as well as the PDF and accumulated PDF difference superimposed in corresponding panels by red lines, respectively	63
4.11	Tropical intensity dependent PDF difference on land in different climatology regions shown in panel (a), accumulated PDF difference on land in panel (b), while the PDF difference over ocean is displayed in panel (c). Accumulated PDF difference over ocean in panel (d). The format of panel (a) and panel (c) are the same as that of Fig. 10c, and the format of panel (b) and panel (d) the same as the one of Fig. 4.10f	66
4.12	Subtropical intensity dependent accumulated PDF on land in summer shown in panel (a), on land in winter in panel (b), over ocean in summer in panel (c) and over ocean in winter in panel (d). The format of all these panels is the same as Fig. 4.10f	67
4.13	Same as Fig. 4.12. except for mid-high latitudes	69
5.1	EOF1 (color shading) and the climatological mean (contours) of Northern Hemisphere monthly averaged $vv_{250}$ from the ERA-40 reanalysis for 1958-2001 in panel (a), as well as Athena IFS simulations at T159 in panel (b), T511 in panel (c), and T1279 in panel (d)	77
5.2	Same as Fig. 5.1 but for EOF2	79
5.3	EOF1 (color shading) of North Pacific sector, indicated by green lines, monthly averaged $vv_{250}$ from the ERA-40 reanalysis for 1958-2001 in panel (a), as well as Athena IFS simulations at T159 in panel (b), T511 in panel (c), and T1279 in panel (d). The climatological mean of Northern Hemisphere monthly averaged $vv_{250}$ from the corresponding dataset is overlaid by contours	81
5.4	Same as Fig 5.3 but for EOF2	82

5.5	EOF1 (color shading) of the North Atlantic sector, indicated by green lines, monthly averaged $vv_{250}$ from the ERA-40 reanalysis for 1958-2001 in panel (a), as well as Athena IFS simulations at T159 in panel (b), T511 in panel (c), and T1279 in panel (d). The climatological mean of Northern Hemisphere monthly averaged $vv_{250}$ from the corresponding dataset is overlaid by contours	83
5.6	Same as Fig. 5.5 but for EOF2 (color shading) of North Pacific sector	84
5.7	The correlation coefficients (color shading) and regression coefficients (contours) between PC1 of the North Pacific sector, indicated by green lines, monthly averaged $vv_{250}$ and the corresponding layer geopotential height fields from the ERA-40 reanalysis for 1958-2001 in panel (a), as well as Athena IFS simulations at T159 in panel (b), T511 in panel (c), and T1279 in panel (d). Only values of correlation coefficients that pass the significance test are displayed	85
5.8	The correlation coefficients (shading) and regression coefficients (contours) between PC2 of the North Pacific sector, indicated by green lines, monthly averaged $vv_{250}$ and the corresponding layer geopotential height fields from the ERA-40 reanalysis for 1958-2001 in panel (a), as well as Athena IFS simulations at T159 in panel (b), T511 in panel (c), and T1279 in panel (d). Only values of correlation coefficients that pass the significance test are displayed	87
5.9	Same as 5.8, but in Cartesian coordinate, rather than in spherical coordinate frame	88
5.10	The leading modes of the ensemble mean from Minerva simulated NH DJF mean $vv_{250}$ . EOF1 from T319 in (a), EOF2 from T319 in (b), EOF1 from T639 in (c), and EOF2 from T639 in (d)	90

5.11	Minerva T319 PC1 (blue solid) and T639 PC1 (red solid) of $vv_{250}$ , the time series of ERA-Interim $vv_{250}$ projected onto T319 PC1 (blue cross) and onto T639 PC1 (red cross), as well as the time series of T319 $vv_{250}$ from individual simulations projected onto T319 PC1 (blue dots) and the time series of T639 $vv_{250}$ from individual simulations projected onto T639 PC1 (blue dots) shown in (a). T319 PC2 (blue solid) and T639 PC2 (red solid) of $vv_{250}$ , the time series of ERA-Interim $vv_{250}$ projected onto T319 PC2 (blue cross) and onto T639 PC2 (red cross), as well as the time series of T319 $vv_{250}$ from individual simulations projected onto T319 PC2 (blue dots) and the time series of T639 $vv_{250}$ from individual simulations projected onto T639 PC2 (blue dots) shown in (b). All $vv_{250}$ in this figure are based on NH DJF mean . . . . .	92
5.12	The leading fourth modes of observed NH DJF mean $vv_{250}$ EOF1 in (a), EOF2 (b), EOF3 (c), and EOF4 in T639 (d) . . . . .	94
5.13	Minerva T319 PC1 and T639 PC1 of NH DJF mean $vv_{250}$ , and observed PCs significantly correlated with T319 PC1 in (a). T319 PC2 and T639 PC2, and observed PCs significantly correlated with T319 PC1 in (b) . . . . .	96
5.14	Correlation coefficients between Minerva T319 PC1 of NH DJF mean $vv_{250}$ and observed NH DJF mean $vv_{250}$ in (a), between observed PC2 and simulated T319 in (b), between observed PC3 and simulated T319 in (c), and between observed PC4 and simulated T319 in (d) . . . . .	98
5.15	Correlation coefficients between Minerva T319 PC1 of NH DJF mean $vv_{250}$ and SST in (a), between T319 PC1 and precipitation in (b), between T319 PC1 and SLP in (c), as well as between T319 PC1 and 250 hPa geopotential height in (d) . . . . .	101
5.16	Correlation coefficients between Minerva T319 PC1 of NH DJF mean $vv_{250}$ and observed SST in (a), between T319 PC1 and observed precipitation in (b), between T319 PC1 and observed SLP in (c), as well as between T319 PC1 and observed 250 hPa geopotential height in (d) . . . . .	103
5.17	Correlation coefficients between Minerva T319 PC2 of NH DJF mean $vv_{250}$ and SST in (a), between T319 PC2 and precipitation in (b), between T319 PC2 and SLP in (c), as well as between T319 PC2 and 250 hPa geopotential height in (d) . . . . .	104

## Abstract

UNDERSTANDING CLIMATE VARIABILITY AND GLOBAL CLIMATE CHANGE USING HIGH-RESOLUTION GCM SIMULATIONS

Xuelei Feng, PhD

George Mason University, 2016

Dissertation Director: Dr. Bohua Huang

In this study, three climate processes are examined using long-term simulations from multiple climate models with increasing horizontal resolutions. These simulations include the European Centre for Medium-range Weather Forecasts (ECMWF) atmospheric general circulation model (AGCM) runs forced with observed sea surface temperatures (SST) (the Athena runs) and a set of coupled ocean-atmosphere seasonal hindcasts (the Minerva runs). Both sets of runs use different AGCM resolutions, the highest at 16 km. A pair of the Community Climate System Model (CCSM) simulations with ocean general circulation model (OGCM) resolutions at 100 and 10 km are also examined. The higher resolution CCSM run fully resolves oceanic mesoscale eddies.

The resolution influence on the precipitation climatology over the Gulf Stream (GS) region is first investigated. In the Athena simulations, the resolution increase generates enhanced mean GS precipitation moderately in both large-scale and sub-scale rainfalls in the North Atlantic, with the latter more tightly confined near the oceanic front. However, the non-eddy resolving OGCM in the Minerva runs simulates a weaker oceanic front and weakens the mean GS precipitation response. On the other hand, an increase in CCSM oceanic resolutions from non-eddy-resolving to eddy resolving regimes greatly improves the

model's GS precipitation climatology, resulting in both stronger intensity and more realistic structure. Further analyses show that the improvement of the GS precipitation climatology due to resolution increases is caused by the enhanced atmospheric response to an increased SST gradient near the oceanic front, which leads to stronger surface convergence and upper level divergence.

Another focus of this study is on the global warming impacts on precipitation characteristic changes using the high-resolution Athena simulations under the SST forcing from the observations and a global warming scenario. As a comparison, results from the coarse resolution simulation are also analyzed to examine the dependence on resolution. The increasing rates of globally averaged precipitation amount for the high and low resolution simulations are  $1.7\% \text{ K}^{-1}$  and  $1.8\% \text{ K}^{-1}$ , respectively. The sensitivities for heavy, moderate, light and drizzle rain are 6.8, -1.2, 0.0,  $0.2\% \text{ K}^{-1}$  for low and 6.3, -1.5, 0.4,  $-0.2\% \text{ K}^{-1}$  for high resolution simulations. The number of rainy days decreases in a warming scenario, by 3.4 and  $4.2 \text{ day year}^{-1}$ , respectively. The most sensitive response of  $6.3\text{-}6.8\% \text{ K}^{-1}$  for the heavy rain approaches that of the  $7\% \text{ K}^{-1}$  for the Clausius-Clapeyron scaling limit. During the twenty-first century simulation, the increases in precipitation are larger over high latitude and wet regions in low and mid-latitudes. Over the dry regions, such as the subtropics, the precipitation amount and frequency decrease. There is a higher occurrence of low and heavy rain from the tropics to mid-latitudes at the expense of the decreases in the frequency of moderate rain. Major features of global precipitation, such as the ITCZ and SPCZ, have shifted southward significantly under the global warming scenario.

In the third part, the inter-annual variability of the northern hemisphere storm tracks is examined. In the Athena simulations, the leading modes of the observed storm track variability are reproduced realistically by all runs. In general, the fluctuations of the model storm tracks in the North Pacific and Atlantic basins are largely independent of each other. Within each basin, the variations are characterized by the intensity change near the climatological center and the meridional shift of the storm track location. These two modes are associated with major teleconnection patterns of the low frequency atmospheric variations.

These model results are not sensitive to resolution. Using the Minerva hindcast initialized in November, it is shown that a portion of the winter (December-January) storm track variability is predictable, mainly due to the influences of the atmospheric wave trains induced by the El Niño and Southern Oscillation.

## Chapter 1: Motivation

The earth climate is a profoundly nonlinear system, in which a variety of physical processes of different time and spatial scales evolve and interact with each other (Palmer, 1999). These scale-interactions have fundamental importance in maintaining the mean climate state, as well as the weather and climate variations on a variety of spatial and time scales. In both the atmosphere and ocean, the planetary and basin-wide processes set up the background stages for the synoptic and meso-scale processes to develop, which govern the local weather and facilitate energy cascade from large-scale to turbulent and micro-scale processes. On the other hand, the smaller scale processes have significant feedback to the large-scale circulation that impacts processes' evolution (Palmer et al., 2008). Since the climate models always have limited resolutions, some of these small-scale processes are inevitably parameterized. However, the climate models need to adopt adequate resolutions so that they can explicitly resolve the dynamical interactions of the variations on widely ranging space and time scales to accurately represent the major weather and climate processes (Shapiro and Thorpe, 2004).

At the current stage of the climate model development, increasing model resolution is likely to lead to significant improvement in the simulation of major weather and climate phenomenon and processes. For instance, state-of-the-art coupled climate models used in the Intergovernmental Panel on Climate Change (IPCC) Fourth Assessment Report (AR4); Solomon et al. (2007) have been limited to a relatively coarse resolution both in the atmosphere and in the ocean. In neither component are some key aspects of the climate system adequately represented. It is important to enhance the climate models' capabilities by incorporating the effects of these meso-scale processes with sharp gradients and to determine what model configurations are adequate to incorporate these effects. Recent

development of supercomputing technology has made it possible to conduct climate simulations at high resolutions to examine the importance of the scale interactions e.g., (Kinter et al., 2013). However, how to utilize the increasing computational resources to improve the climate simulations most efficiently is still a major issue to be explored. A number of studies have investigated the influence of horizontal resolution on simulated climate by resolving previously inaccessible finer-scale processes. Several recent studies have focused on the importance of atmospheric model resolution in climate simulation e.g., (Brankovic and Gregory, 2001; Gent et al., 2010; Hack et al., 2006; Kobayashi and Sugi, 2004; May and Roeckner, 2001; Navarra et al., 2008; Pope and Stratton, 2002). The reported results are still quite diverse, ranging from minor or no improvement to significant difference in the model mean state and variability, depending on the areas and phenomena examined. For oceanic high-resolution simulation, the current literature provides compelling evidence suggesting that an eddy-resolving ocean component model in a climate system will significantly impact the simulation of the large-scale climate (Kirtman et al., 2012). A major effort should be made to carefully evaluate the effects of model resolution increase on the climate systems.

In this study, we examine three phenomena simulated by climate models and evaluate the effects of increased model resolution in either the atmosphere or ocean. Firstly, we investigate the influences of horizontal resolution in both atmospheric and oceanic model components on the mean precipitation over the Gulf Stream (GS) region, using climate simulations from coupled European Centre for Medium-range Weather Forecasts (ECMWF) and NCAR Community Climate System Models (CCSM), as well as atmospheric ECMWF general circulation models. For this purpose, three sets of model experiments are analyzed. The first two examine the effects of increasing horizontal resolution of an atmospheric general circulation model (AGCM) gradually from around 100 to 10 km under fixed oceanic settings. Specifically, the ECMWF AGCM is either forced with prescribed observational sea surface temperature (SST) (the first case) or coupled to a non-eddy-resolving ocean general circulation model (OGCM) at a fixed horizontal resolution near 100 km (the second

case). The third set of experiments examines the effects of the oceanic resolution with a pair of long-term simulations by the CCSM coupled ocean-atmosphere general circulation model (CGCM), in which the OGCM is run respectively at non-eddy-resolving (100 km) and eddy-resolving (10 km) resolutions, while the AGCM resolution remains fixed at around 50 km for both runs.

The second focus of this study is the Greenhouse Gas (GHG) warming impacts on precipitation characteristic changes using very high resolution model simulations. We analyze changes in global precipitation and large-scale features associated with GHG from simulations obtained for the Atmospheric Model Inter-comparison Project (AMIP) and Time-slice experiments based on ECMWF Integrated Forecast System (IFS) runs as part of the Athena project. These data are at horizontal resolutions of 16-km grid (T1279) over 47 years and a temporal resolution of 6 hourly. For AMIP simulations, atmosphere-only integrations with the IFS were carried out for the period 1960-2007 with observed SST and sea ice fields. Time-slice simulations are performed under the Intergovernmental Panel on Climate Change (IPCC) Special Report on Emission Scenarios (SRES). Both SST and sea ice concentrations were modified by adding perturbations taken as the difference between the 2065-75 and 1965-1975 monthly climatologies from simulations with the Community Climate System Model (CCSM) (Collins et al., 2006). As a comparison, results from the coarse resolution of 126-km (T159) are also analyzed to examine the dependence on resolution.

After exploring the mid-latitude mean state climate in the first topic, we focus on the high frequency climate of the mid-latitudes. Using the monthly variance of high-pass filtered daily 250 hPa meridional wind as a storm-track indicator, we examine the model fidelity in simulating the Northern Hemisphere (NH) storm track monthly variability and its sensitivity to model horizontal resolution based on atmospheric ECMWF hindcast runs and coupled CCSM simulations. The filter used in this study is a 13<sup>th</sup>-order Butterworth filter with 50% cut-off signal at a period of 6 days. Most of the previous studies focus on the observations. In this study, based on model simulations, we analyze how well our

climate models reproduce the major features of the observed storm track variations and whether their results are sensitive to the model horizontal resolutions by means of empirical orthogonal function (EOF) analysis. In terms of the Northern Hemisphere as a whole, we investigate the relationships of the storm track variations between North Pacific sector and North Atlantic sector by altering resolutions and using EOF analysis. In individual sectors of North Pacific and North Atlantic, we evaluate the connections of the sectorial storm track variability and atmospheric low-frequency fluctuations, as well as with the underlying surface forcing, meanwhile examine the sensitivity of these relationships to model resolutions. In addition, the comparison of simulations from the atmospheric ECMWF IFS and coupled CCSM runs are made, which further reveals the roles played by the atmosphere and ocean components in the air-sea interaction process.

The analyses associated with storm track inter-annual variability imply the mid-latitude storm track variations over the North Pacific are connected with the tropics by ENSO-induced teleconnection. In general, the atmospheric anomalies induced by the underlying surface forcing is predictable on seasonal time scales, while the atmospheric internal variability has a shorter predictability, with a typical order of less than a month. Based on our previous results, we speculate that the low-frequency variations of the storm track strength over the North Pacific have high predictability on seasonal time scales. Considering this, in the last topic we examine the seasonal predictability of extra-tropical NH winter mean storm track using the ECMWF coupled model ensemble hindcast runs with two different atmospheric resolutions initialized at November 1 for 1979-2012. Moreover, the potential mechanism is likewise explored.

The rest of this study is structured as follows. Chapter 2 introduces data and model configuration. Horizontal resolution influences on mean state precipitation in Gulf Stream region are discussed in chapter 3. Chapter 4 investigates global warming impacts on precipitation characteristics based on high-resolution simulations. Chapter 5 examines the Northern Hemisphere (NH) mid-latitude storm track inter-annual variability, and seasonal predictability. Summary is given in Chapter 6.

## Chapter 2: Model Simulations and Observational Data

We use existing climate model simulations from several major modeling projects to examine their simulated GS precipitation. Three sets of experiments are analyzed. The first two examine the effects of increasing AGCM horizontal resolution forced with observational SST or coupled to an OGCM at a given resolution. The third set examines the effects of the oceanic resolution with a pair of long-term simulations by another CGCM, with its OGCM configured at non-eddy-resolving and eddy-resolving resolutions respectively while its AGCM resolution remains fixed. These simulations are described below. The observational datasets used in this study are also described.

### 2.1 Athena atmospheric simulations

The sensitivity to the horizontal resolution of an AGCM forced with observational SST is studied using simulations from Project Athena (Kinter et al., 2013). Athena is a pilot project. This collaboration project involves an international team of climate-weather modelers and high-end computing experts from five institutions to test whether representing mesoscale and subsynoptic atmospheric processes in climate models improves climate simulation and prediction. The Athena supercomputer was placed in dedicated mode for the period from 1 October 2009 to 1 April 2010. Numerical simulations were carried out with two different global atmospheric general circulation models: the European Centre for Medium-range Weather Forecasts (ECMWF) Integrated Forecast System (IFS), a hydrostatic spectral model used for operational seasonal forecast at the ECMWF, and the Non-hydrostatic ICosahedral Atmospheric Model (NICAM) global atmospheric model from the Japan Agency for Marine-Earth Science and Technology (JAMSTEC) and the University of Tokyo. Multiple simulations with different resolutions have been designed to increase

weather and climate model resolution to accurately resolve cloud systems and mesoscale atmospheric phenomena. Project Athena is the first project in which these models have been run over such long simulations at the highest possible resolution. More details about Project Athena are described in (Kinter et al., 2013).

### 2.1.1 ECMWF IFS hindcasts runs with different resolutions

The IFS hindcast runs contain four different horizontal resolutions, which are named according to the cutoff wavenumber used in the spherical harmonics expansion, T159 ( $\sim 126$  km), T511 ( $\sim 39$  km), T1279 ( $\sim 16$  km), and T2047 ( $\sim 10$  km), respectively. In the vertical, the IFS is discretized with 91 hybrid levels (top full level at 0.01 hPa) using a finite element scheme (Untch and Hortal, 2004). The model parameterization package of sub-scale physics is state-of-the-art and details of these physical parameterizations are given by (Jung et al., 2012). There is no tuning of the parameters in the parameterization schemes after the resolution changes so that most of the parameterizations were unchanged. For the convection scheme, however, the convective adjustment time has a resolution-dependence that is largest for relatively low resolutions (i.e., from T159 to T511). By design, the parameterized orographic gravity wave drag is also reduced with increased horizontal resolution (Brown, 2004).

The hindcast runs are comprised of 13-month long integrations starting on 1 November of each of the years 1960-2007 for T159, T511, and T1279. The atmospheric initial conditions are from the 40-year ECMWF reanalysis (ERA-40) over the period of 1960-1989 and ERA-interim over 1990-2007, which are linearly interpolated to the corresponding model resolutions. All integrations are carried out with the prescribed forcing from observed SST and sea ice fields. In particular, the SST forcings are from the UK Met Office HADISST1 monthly mean fields used for 1960-1981 (Rayner et al., 2003) and the weekly OISST-v2 for 1982-2001 (Reynolds et al., 2002). Both datasets are on a  $1^\circ$  latitude-longitude grid globally. For 2002-2008, daily SST from the operational ECMWF analysis is used by (Jung et al., 2012).

Our analysis is based on the monthly mean outputs from the last 12 months of the integration after a one-month spin-up. Most of the model outputs for T511, T1279, and T2047 results are truncated to T159 and interpolated to a corresponding N80 grid. Only a few selected fields, e.g., precipitation, are preserved on their more native grids, corresponding to 320, 1024, 2560 and 4096 grid points along the equator for the four sets of runs, respectively. Using the truncated outputs, we can directly compare features of the same spatial scales from different model runs to identify the resolution influences on them. The drawback of the truncation is that we cannot recover some fine scale contributions that may be crucial to explain the larger-scale differences. Corresponding runs for T2047 were only carried out for the years of 1989-2007. For the period consistency, we will not take T2047 into account in this analysis. To examine the summer precipitation, we have also used the output from the NICAM simulation. The NICAM model is non-hydrostatic and has a 7 km horizontal resolution. We have analyzed eight runs initialized on May 21 and finishing on August 31 for every year from 2001 to 2009, except for 2003 (Kinter et al., 2013).

### **2.1.2 ECMWF IFS AMIP runs with different resolutions**

For AMIP simulations, atmosphere-only integrations with the IFS are carried out for the period 1960-2007 with observed SST and sea ice fields at T159 and T1279. Atmospheric initial conditions and lower boundary fields are a combination of T159 data from the 40-yr ECMWF Re-analysis (ERA-40, covering 1960-89) and T255 data from ERA-Interim (1990-2007) interpolated spatially to the resolution of the model and, when necessary, linearly in time to obtain daily varying fields. For the period 1960-81, SST and sea ice fields are based on monthly mean values produced by the Met Office (Rayner et al., 2003). The weekly National Oceanic and Atmospheric Administration/National Centers for Environmental Prediction (NOAA/NCEP) two-dimensional variational data assimilation (2DVAR) dataset (Reynolds et al., 2002) is used until 2001 (ERA-Interim uses ERA-40 data until 2001). From 2002 onward, daily SST and sea (surface temperature) data from the operational ECMWF analysis are employed.

### 2.1.3 Time-slice experiments

The time-slice experiment is run by including the boundary conditions representing end-of-the-21st century conditions under climate change conditions. The time-slice experiment with the IFS covering the period 2070-2117 is carried out at T1279. The forecast is started using atmospheric initial conditions from ERA-40 from 1 November 1970. In the time-slice experiment, both SST and sea ice concentrations are modified by adding perturbations taken as the difference between the 2065-75 and 1965-1975 monthly climatologies from simulations with the Community Climate System Model (CCSM) (Collins et al., 2006). A more detailed description of the approach is given in (Schneider et al., 2009). Monthly values are then linearly interpolated to daily values. The CCSM experiment is carried out at T85 ( $1.4^\circ \times 1.4^\circ$ ) for the atmosphere and on an approximately  $1^\circ$  grid for the ocean and sea ice. The atmospheric greenhouse gas concentrations follow the Intergovernmental Panel on Climate Change (IPCC) emissions scenario A1B until the year 2100. Thereafter concentrations are held constant at their 2100 values. A1B describes the global population peaks in mid-century and declines thereafter with the assumption of a rapid economic growth in the future (Nakicenovic et al., 2003). In this study, we analyze the simulations only based on higher resolution (T1279) runs in both AMIP and Time-slice experiments because models in higher resolution are able to incorporate more physical processes on different spatial and time scales, and then better represent the real earth climate system (Palmer, 1999).

## 2.2 Minerva simulations

Since the Athena simulations described in subsection 2.1 are atmospheric runs only, we have supplemented them with a set of coupled model simulations with the IFS as its atmospheric component from another research project to assess the effect of air-sea feedback. Project Minerva was a collaboration between the ECMWF and the Center for Ocean-Land-Atmosphere Studies (COLA) as an extension of Project Athena (Zhu et al., 2015). In this

project, the ECMWF seasonal forecast system, version 4, is used for seasonal hindcast with a slightly updated IFS from the ones used in Athena with different horizontal resolutions as its atmosphere component. The ocean component uses Nucleus for European Modeling of the Ocean (NEMO), version 3.0 (Madec, 2008). Its horizontal configuration adopts the ORCA1 grid (<http://www.noc.soton.ac.uk/nemo/>), which has a horizontal resolution of approximately  $1^\circ$  degree (meridionally refined to  $1/3^\circ$  near the equator). It has 42 levels in the vertical, 18 of which are in the upper 200m. IFS and NEMO are coupled every 3 hours.

In Project Minerva, three sets of seasonal hindcasts were performed with different atmospheric horizontal resolutions T319 ( $\sim 62\text{km}$ ), T639 ( $\sim 31\text{km}$ ) and T1279 ( $\sim 16\text{km}$ ), while ocean resolution is fixed at the resolution comparable to that of the prescribed SST data in the Athena runs. The 7-month seasonal hindcasts of T319 (T639) with 51 (15) ensemble members are conducted with the observed initial conditions starting from May 1 during 1980-2011 and November 1 during 1980-2010 (Zhu et al., 2015). Considering the limitation of computing resources, the T1279 hindcasts only went back to 2000. The ensemble initialization for both IFS and NEMO follows the same procedure as that for the operational ECMWF System 4 (Molteni et al., 2011). In this study, we only use the first 15 ensemble members for all three sets of hindcasts. The first month of integrations is discarded as spin-up.

## 2.3 CCSM3.5 simulations

Both the Athena and Minerva simulations examine the influence of the AGCM resolution at moderate oceanic resolution in either forcing or model. As we will show in Section 3, the oceanic setting seems to play an important role in these experiments. In order to further examine the impacts of oceanic fronts and mesoscale eddies, we also examined a pair of sensitivity simulations by a pre-release of NCAR Community Climate System Model (CCSM) version 4.0. The CCSM is a state-of-the-art coupled climate model consisting of

atmosphere, ocean, land, and sea ice components. Details of the model configuration for this set of experiments are given in Kirtman et al. (2012). Briefly, the atmosphere component is the Community Atmosphere Model (CAM) that uses the finite volume discretization (Lin and Rood, 1997) and has 26 vertical levels in a hybrid coordinate. Its horizontal resolution is fixed at zonal resolution  $0.625^\circ$  and meridional resolution  $0.5^\circ$  in both experiments. The land component has the same horizontal resolution as the AGCM. The oceanic component has 42 levels vertically but different horizontal resolutions for the two runs, which will be discussed in more details in the next paragraph. All the component models communicate via the CCSM flux coupler (Craig et al., 2011) where the fluxes at the air-sea interface are calculated at 6-h intervals using atmospheric state variables interpolated onto the ocean model grid and conservatively remapped onto the other component model native grids. In this sensitivity experiment, the control run is a 155-year present-day climate simulation with CAM coupled to the oceanic and sea-ice components that have zonal resolution of  $1.2^\circ$  and meridional resolution varying from  $0.27^\circ$  at the equator to  $0.54^\circ$  in the mid-latitudes. The sensitivity run is carried out with the horizontal resolution of the oceanic and sea-ice component models increased to  $0.1^\circ$  in both latitude and longitude. In this case, the maximum grid spacing is 11 km at the equator, reducing to 2.5 km in high latitudes, which fully resolves the meso-scale eddies in ocean. The ocean model uses a biharmonic closure of horizontal mixing and diffusion for both momentum and tracers. Their hyperviscosity and diffusivity are resolution-dependent because they are scaled with the cube of the local grid spacing (Bryan et al., 2007). The initial conditions are the same for both the low and high-resolution simulations except that the ocean state are interpolated to their corresponding grids. For the high-resolution run, a filter is added to the polar winds to reduce computational instability. After 102 years of spin-up. The experiment is then extended to 155 years. Kirtman et al. (2012) found that, although the polar filter produces some differences to the earlier part of the simulation, these differences are very small compared to those between the high-resolution and low-resolution simulations. In this study, we examine the climatology and seasonal cycle in the GS region using the last

53 years of the high-resolution simulation (after the polar filter is applied). The low and high-resolution runs will be referred to as LRC07 and HRC06 hereafter, following Kirtman et al. (2012).

## 2.4 Observational datasets

Several observational datasets are used for model verification in this study. The Tropical Rainfall Measurement Mission Project (TRMM) multisatellite precipitation analysis (TMPA) daily rainfall estimate, version 7.0 (3B42 V7) covers the area from 50°S to 50°N with a spatial resolution of 0.25° latitude by 0.25° longitude. Its period is from January 1998 to October 2012. Additional observational datasets are the SLP and divergence on 23 pressure levels from ERA40, from September 1957 to August 2002. The ERA-40 data are originally in spectral format with a resolution of T85 and have been transformed to a regular 2.5° latitude x 2.5° longitude grid for SLP and winds at each pressure level. However, the surface winds are transformed to a Gaussian grid with  $256 \times 128$  data points globally.

The daily gridded SST field using optimum interpolation (OI) analysis of the Advanced Very High Resolution Radiometer (AVHRR) is used in this study for coupled model SST verification. The OI-daily SST has a spatial grid resolution of 0.25° that matches the TMPA precipitation in both spatial and temporal resolution and also better represents the SST front and meso-scale features in the Gulf Stream region. Both Pathfinder (from January 1985 to December 2005) and operational AVHRR data (2006 onward) are blended with in situ SST measurements from ships and buoys, with a large-scale adjustment of satellite biases with respect to the in situ data.

## **Chapter 3: A multi-model analysis of the resolution influence on precipitation climatology in Gulf Stream region**

### **3.1 Introduction**

Atmosphere and ocean are linked to each other by their exchanges of heat, water, gases and momentum on a variety of time and spatial scales. In particular, the air-sea interaction between the regional wind and SST play a critical role (Chelton and Xie, 2010). Before the turn of the century, most analyses about the space-time variability of winds over the ocean were based on reports from sparse ship measurements. These ship observations in conjunction with coupled climate models in comparably coarse resolutions demonstrate a negative correlation between SST and local wind speed (Xie, 2004) except in the tropics. This large-scale phenomenon can be explained as the oceanic response to wind-induced latent and sensible heat fluxes (Barsugli and Battisti, 1998; Frankignoul, 1985).

With the advance of satellite-based high-resolution remote sensing techniques, mid-latitude ocean-atmosphere coupling at oceanic mesoscales can be measured directly. As a result, a fundamentally different picture is revealed of the air-sea interaction on the spatial scales of 10-100 km than those on 1000 km and longer. Using the wind fields measured by the QuikSCAT scatterometer and SST from the Advanced Microwave Scanning Radiometer (AMSR-E) (Chelton and Wentz, 2005) on the Earth Observing System Aqua satellite, (O'Neill et al., 2005) first found a very strong positive correlation between wind and SST on the scales of 10-100 km over the Agulhas Return Current in the Southwest Indian Ocean. Thereafter, such potential SST forcing on local surface winds at mesoscales has been found in every region of strong SST fronts and active oceanic eddies from satellite observations (Chelton and Xie, 2010).

One explanation of the positive SST-wind correlation on oceanic mesoscales, mostly associated with the oceanic eddies and fronts, is that an intensive increase in local SST reduces the static stability of the near-surface atmosphere, causing enhanced turbulent mixing that draws momentum from aloft to accelerate the surface wind (Xie, 2004). Minobe et al. (2008) also point out that, in the marine boundary layer, the atmospheric pressure adjustments to sharp SST gradients lead to surface wind convergence. In general, this convergence is induced by winds across an SST front. On the other hand, winds parallel to the SST front generate additional vorticity. Both processes can be quantified by coupling coefficients between wind stress divergence (curl) and the downwind (crosswind) component of the SST gradient (Chelton and Xie, 2010). More recently, Schneider and Qiu (2015) used a linear boundary layer model to examine the relative effects of the SST-induced atmospheric pressure and vertical mixing on a background Ekman flow. Their results show that surface divergence can be caused by either large-scale wind or thermal circulation across the front. On the other hand, the wind stress curl generated by the SST front is weakened by geostrophic spin down.

Recent development of supercomputing technology has made it possible to conduct climate simulations at high resolutions to examine the importance of the scale interactions (e.g., Kinter et al. 2013). However, how to utilize the increasing computational resources to improve the climate simulations most efficiently is still a major issue to be explored. A number of studies have investigated the influence of horizontal resolution on simulated climate by resolving previously inaccessible finer-scale processes. Several recent studies have focused on the importance of atmospheric model resolution in climate simulation (Brankovic and Gregory, 2001; Gent et al., 2010; Hack et al., 2006; Kobayashi and Sugi, 2004; May and Roeckner, 2001; Navarra et al., 2008; Pope and Stratton, 2002). The reported results are still quite diverse, ranging from minor or no improvement to significant difference in the model mean state and variability, depending on the areas and phenomena examined. For oceanic high-resolution simulation, the current literature provides compelling evidence suggesting that an eddy-resolving ocean component model in a climate system will significantly impact

the simulation of the large-scale climate (Kirtman et al., 2012).

In this chapter, we assess the impacts of the atmosphere and ocean horizontal resolutions on precipitation climatology in the Gulf Stream (GS) region in current climate models. The GS region has the most active meso-scale air-sea interactions that significantly affect the regional climate. In particular, the sharp SST fronts in the regions associated with the off-shore western boundary current induces low sea level pressure (SLP) over its warm flank and produces a tight band of precipitation (Minobe et al., 2010, 2008; Song et al., 2006; Sweet et al., 1981; Wai and Stage, 1989; Warner et al., 1990). The enhanced surface baroclinicity also influences the Atlantic storm track (Nakamura et al., 2004). These effects of the intense oceanic front on the storm track pattern and intensity have been investigated using idealized aquaplanet experiments (Brayshaw et al., 2008; Sampe et al., 2010). In this study, we concentrate on whether the current atmospheric and oceanic resolutions of the climate models adequately represent the effects of the SST front on the mean precipitation in the GS region and how effectively an increase in the atmospheric and/or oceanic resolution can improve the simulation. Ideally, these questions should be tackled using a single climate system through a series of sensitivity experiments with different oceanic and atmospheric resolutions under both coupled and uncoupled framework. However, given the tremendous resources required for such a project, no such extensive sensitivity experiment from a single system exists, as far as we know. In this study, we demonstrate that useful information can be gained by analyzing the extensive resolution-related simulations from several coupled and uncoupled climate systems.

## **3.2 Precipitation climatology in the Gulf Stream region**

This section investigates the impacts of horizontal resolution on precipitation climatology in the Gulf Stream region. First, we focus on the Athena simulations with different IFS resolutions, forced by prescribed SST from the observations. Then the effects of air-sea coupling will be further examined using the coupled runs.

### 3.2.1 The Athena simulations

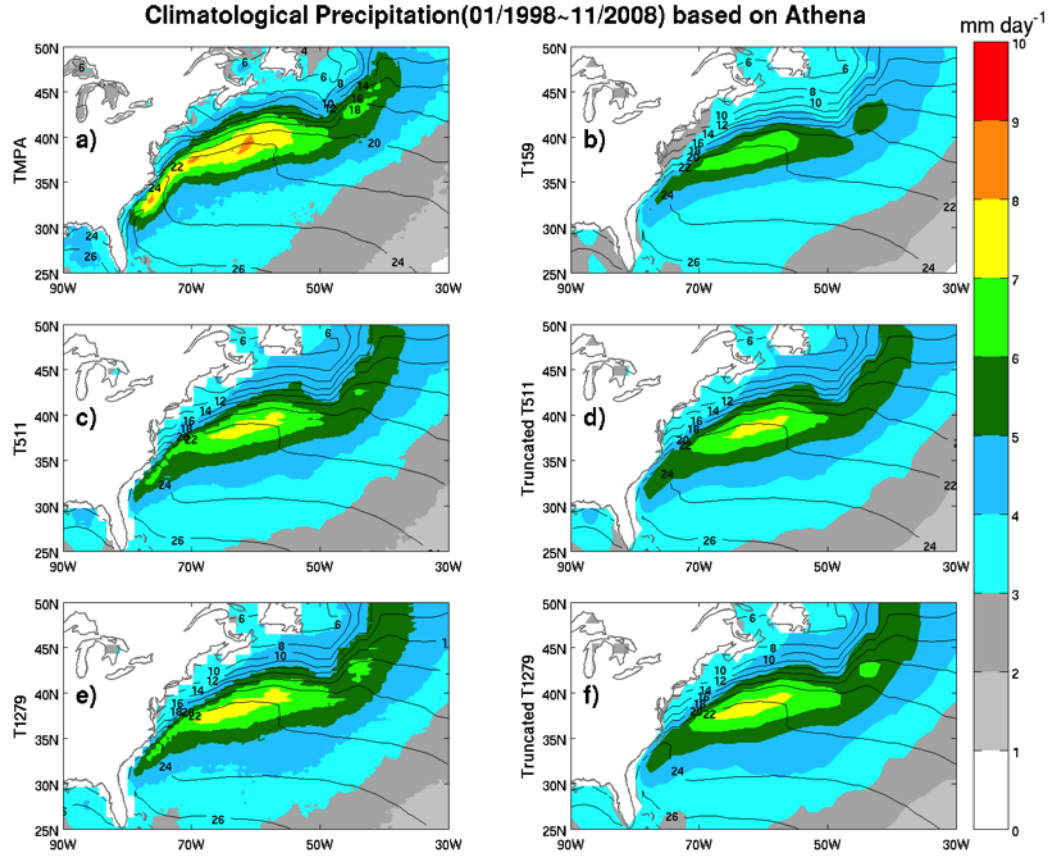


Figure 3.1: Annual precipitation climatology (unit:  $\text{mm day}^{-1}$ ; shading) in the Gulf Stream region ( $25^{\circ}\text{N}\sim 50^{\circ}\text{N}$ ,  $30^{\circ}\text{W}\sim 90^{\circ}\text{W}$ ) from TMPA observations and Athena IFS simulations for 01/1998~11/2008. The superimposed contours are the observed SST climatology ( $^{\circ}\text{C}$ ) for the same period from the OI-daily observations and the SST climatologies in model simulation panels from their corresponding run outputs. Panel (a) shows the observed mean rainfall derived from TMPA monthly precipitation. The IFS mean precipitations are averaged from the last 12 months of the 13 month hindcast runs initialized at 12Z, November 1 for each year from 01/1998~11/2008. Approximately 12 hindcasts in total are averaged to form the mean state. The IFS hindcasts are conducted with different resolutions from T159 (b), T511 (d) and T1279 (f). The model outputs in these three panels are presented on the same grid network, with the T511 and T1279 output truncated to the Gaussian grid T159. The T511 and T1279 output on their native grids are shown in (c) and (e), respectively.

Figure 3.1 displays the annual climatological precipitations (shading) in the Gulf Stream region from the TMPA observations (Fig. 3.1a) and the IFS simulations (Figs. 3.1b-f), overlaid by the observed annual SST climatologies (contour). The SST field superimposed in TMPA precipitation (Fig. 3.1a) is from OI-daily, while the SST overlaid in the remaining panels are from the corresponding prescribed SSTs in each of the IFS simulations. For simulations at T511 and T1279, the mean precipitation is plotted on the native grids of their special truncations (left panels) and the grids with the spectrum truncated at T159 (right panels) equivalent to that of the lowest resolution run (Fig. 3.1b)). The averaged precipitation of the Athena simulations are for the period 1998-2008, consistent with the period of the high-resolution TMPA observations. We have also examined the climatologies of the Athena model precipitation for the whole period of 1960-2008 and the period of 1982-2008 forced with the weekly OISST. Although the characteristics of the model differences are qualitatively similar among the three periods, the qualitative difference is largest in the last period (1998-2008). This is possibly because the SST boundary condition since 2002 is based on the higher-resolution Real-Time Global (RTG) analysis on a  $0.5^\circ \times 0.5^\circ$  grid (Thibaux et al., 2003). Previous studies have shown that the RTG SST forcing generates stronger atmospheric responses in the operational ECMWF numerical weather prediction model, e.g. (Chelton, 2005; Song et al., 2009).

The TMPA observations (Fig. 3.1a) show a narrow band of strong precipitation over the North Atlantic Ocean closely attached to the sharp SST gradient, the oceanic front associated with the Gulf Stream and its extension. This rain band ( $\geq 5\text{mm day}^{-1}$ , green shading) extends from the southwest Florida Coast to the Gulf Stream (GS) extension, and then turns northeastward with the North Atlantic Current (NAC). The strongest precipitation is located at the southern edge of the SST front where the water temperature is higher. The largest rainfall occurs near and to the south of the  $20^\circ\text{C}$  isotherm of SST, and the strong rain belt of intensity higher than  $7\text{ mm day}^{-1}$  closely follows the SST isotherm starting from the east coast of Florida at about  $30^\circ\text{N}$ , extending first northeastward along the coast, then more eastward to  $40^\circ\text{N}$  and close to  $50^\circ\text{W}$  (yellow shading). Within this

rain belt, there are localized centers of rainfall above  $8 \text{ mm day}^{-1}$  (orange shading).

All the IFS simulations in the remaining panels reproduce these characteristics qualitatively although they underestimate the precipitation intensity of this rain band with reference to the TMPA (Fig. 3.1a). The T159 simulation is the weakest. Its main area of precipitation over  $5 \text{ mm day}^{-1}$  is confined within the GS extension region between  $50^\circ\text{W}$  and  $70^\circ\text{W}$ , which is weakened significantly close to the coast between  $20^\circ\text{N}$  and  $30^\circ\text{N}$  and further northeastward (Fig. 3.1b). The southwestern branch never reaches the rainfall level of  $6 \text{ mm day}^{-1}$ . Over the NAC area, only a small area is about  $5 \text{ mm day}^{-1}$ , which is detached from those further to the southwest. In addition, the main precipitation region in  $50^\circ\text{-}70^\circ$  is also narrower meridionally than in observations because its northern edge retreats southward. As the IFS resolution increases, the simulated mean precipitation tends to increase along the track of the GS extension and NAC and agrees more closely to the observations. The T511 run (Figs. 3.1c and 3.1d) shows significant rainfall enhancement over that of the T159 run throughout the GS region as measured by the expansion of the area with precipitation over  $5 \text{ mm day}^{-1}$ . In the northeast, this area extends farther north than the observed area. The rain band also extends its southern end southward along the coast to be more consistent with the observations. At the center, the rain band expands meridionally with maximum intensity increasing to over  $7 \text{ mm day}^{-1}$ . The highest resolution (T1279) run (Figs. 3.1e and f) shows further enhancement in all of these aspects and yields the best pattern and magnitude of the primary precipitation centers. In particular, a clearly defined maximum appears over the NAC at around  $42^\circ\text{N}$  and  $45^\circ\text{W}$  to represent the secondary center on the NAC track more realistically.

For both T511 and T1279 runs, the precipitation bands from the native grids (Figs. 3.1c and 3.1e) show similar patterns to the truncated ones (Figs. 3.1d and 3.1f) and slight improvement in the intensity. This suggests that the improvements generated by increased model horizontal resolution occur mostly on relatively large scales. As a result, the data truncation serves primarily as a smoother in the simulated precipitation. However, the precipitations on native grids do show the narrow band of enhancement in the southwest

over  $6 \text{ mm day}^{-1}$  in both T511 and T1279 that has been smoothed out by the truncation.

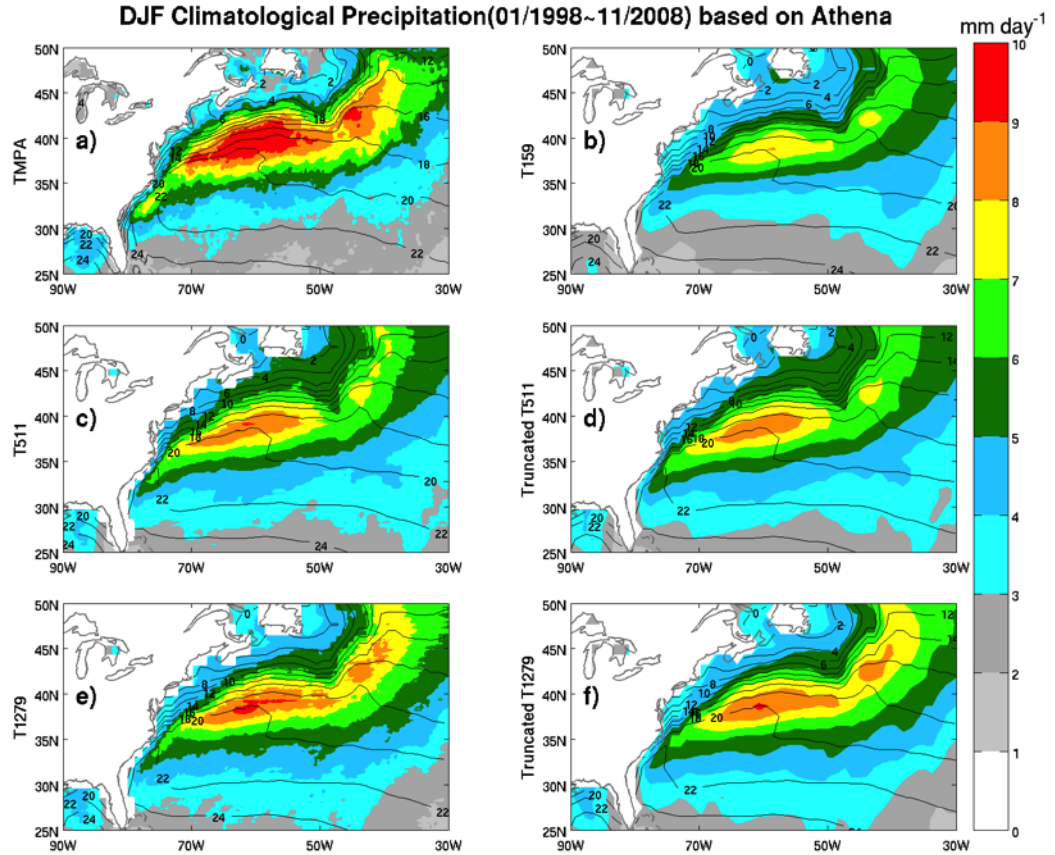


Figure 3.2: As in Fig. 3.1 but for DJF Climatology

The improvements of the GS precipitation with higher model resolution can also be seen seasonally. Figure 3.2 shows the seasonal climatology of the observed and simulated precipitations in boreal winter, averaged for December-February (DJF). The pattern of the observed DJF precipitation is similar to that of the annual mean (Fig. 3.1a), with a main center along the GS extension between  $50^{\circ}\text{W}$ - $70^{\circ}\text{W}$  and a secondary one on the NAC track around  $40^{\circ}\text{W}$ . The precipitation, however, is much stronger than the annual mean (over  $10 \text{ mm day}^{-1}$  in both centers) and with a broader range across the oceanic front. All

resolution simulations (Figs. 3.2b-f) capture these general characteristics but underestimate the rainfall intensity. The lowest resolution run (T159) especially has the weakest rainfall and largely fails to reproduce the NAC center (Fig. 3.2b). The increases in resolution enhance the rain band and expand its range, as seen by the widening edges of the 7 mm day<sup>-1</sup> shading. The T1279 run apparently achieves the best results.

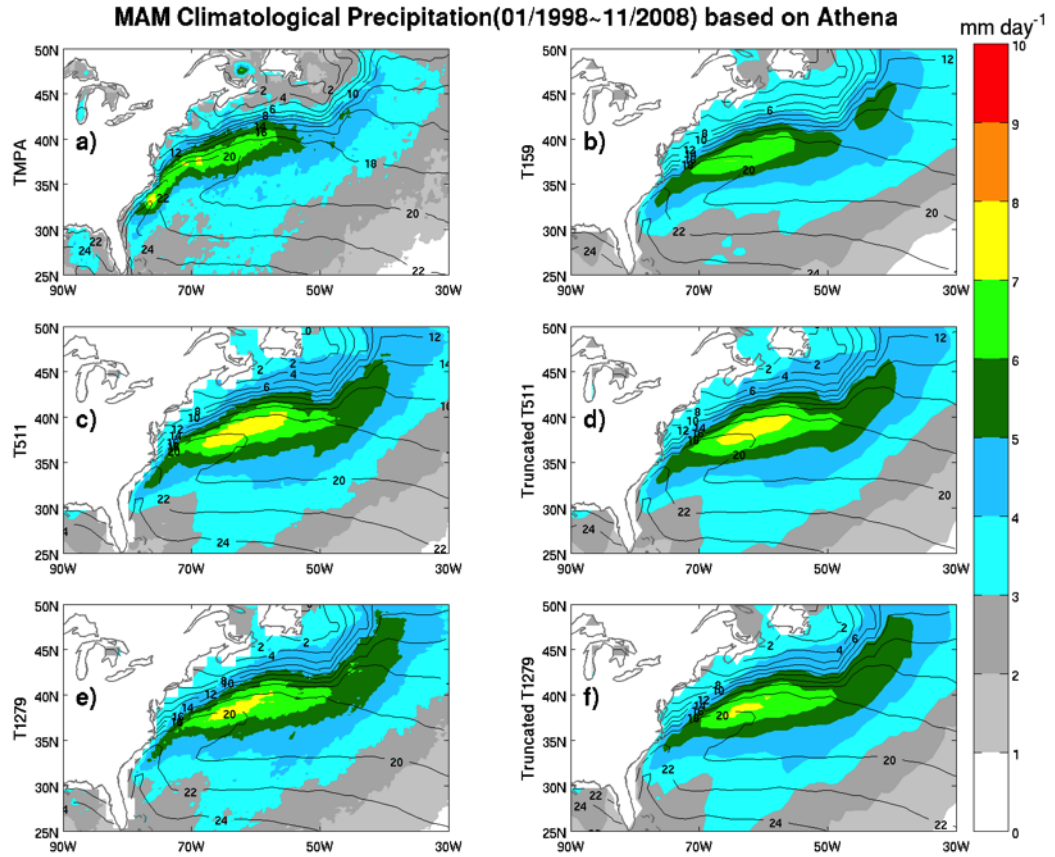


Figure 3.3: As in Fig. 3.1 but for MAM Climatology

By boreal spring, the observed GS precipitation averaged in March-May (MAM. Fig. 3.3a) is weakened dramatically to around 6-7 mm day<sup>-1</sup> in maxima. The rain belt ( $\geq 5$  mm day<sup>-1</sup>, green shading) also shrinks southwestward, to be confined over the warm waters of

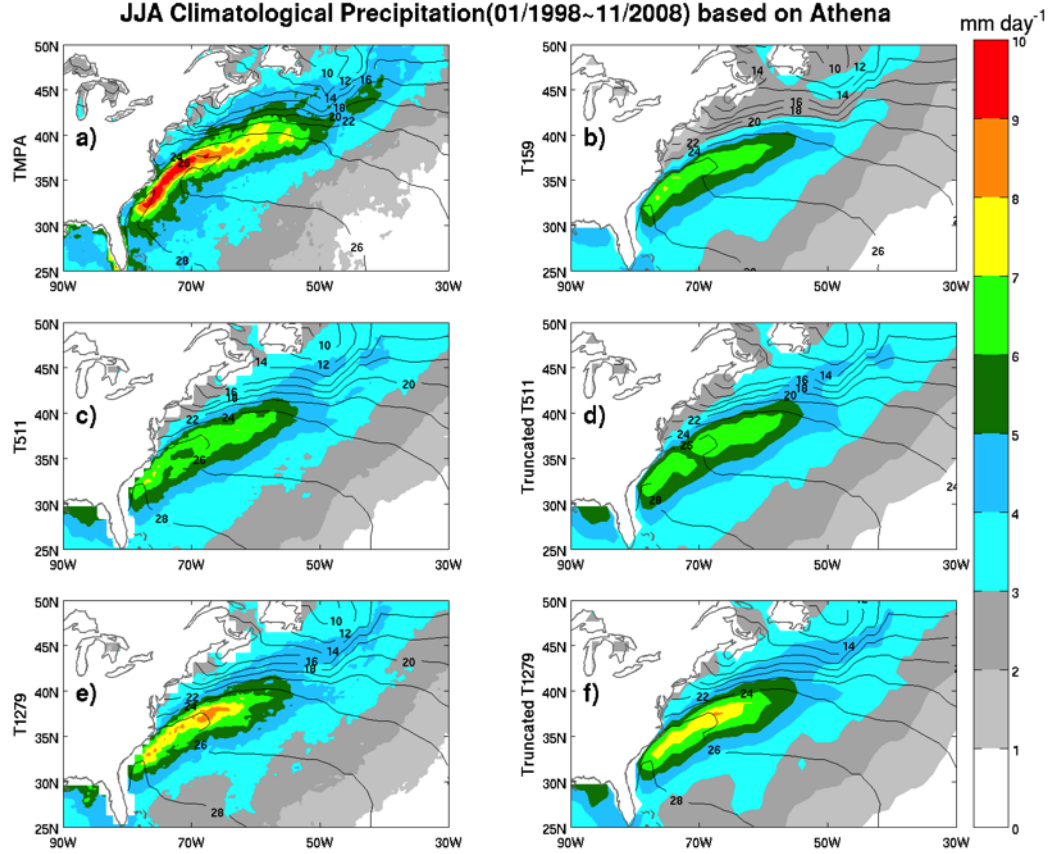


Figure 3.4: As in Fig. 3.1 but for JJA Climatology

the Florida Current and western GS. As a result, the NAC center vanishes and the main rain belt is narrowed. The simulations (Figs. 3.3b-f), though showing a reduction of precipitation from DJF, maintain an excessively strong and broad rain band with a center over the GS extension. The area of large rainfall ( $\geq 5 \text{ mm day}^{-1}$ ) also extends too far north along the NAC track. Overall, the model rainfall pattern in spring is similar to the winter one without showing a clear seasonal transition in runs of all resolutions. Curiously, the precipitation center is stronger at T511 (Figs. 3.3c and 3.3d) than those at lower (Fig. 3.3b) or higher resolutions (Figs. 3.3e and 3.3f).

In June-August (JJA), the observed summer precipitation (Fig. 3.4a) has largely the

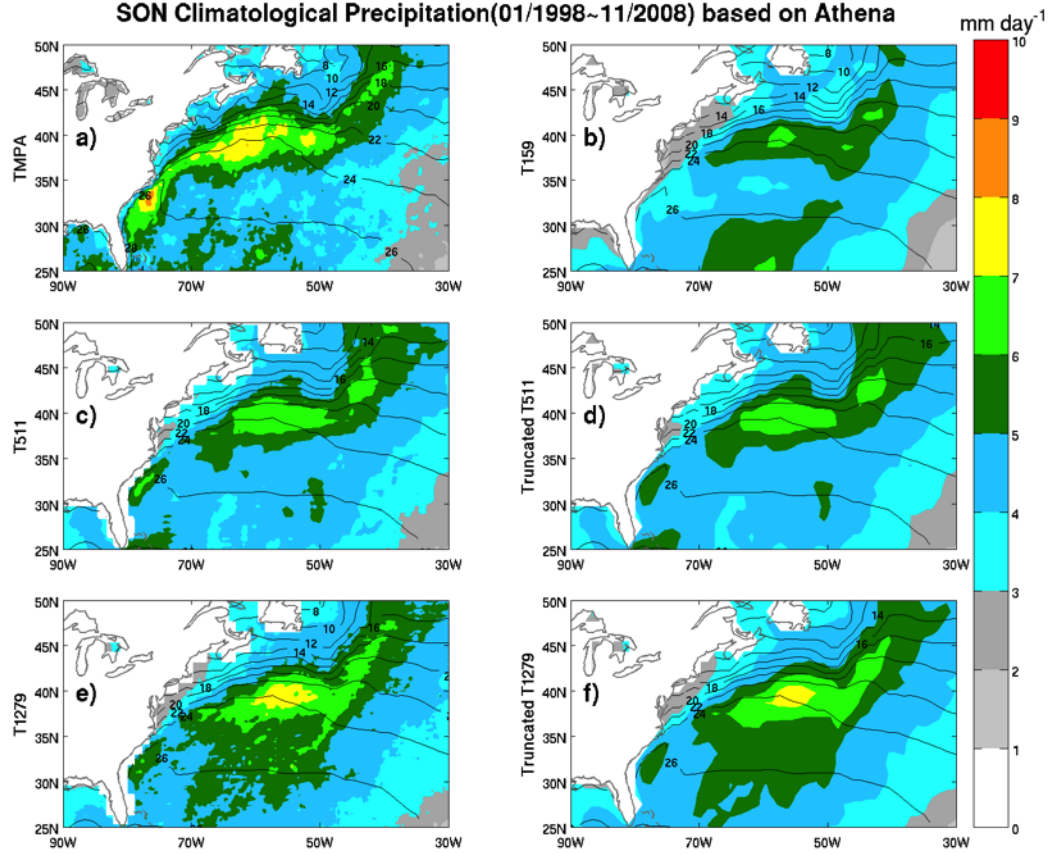


Figure 3.5: As in Fig. 3.1 but for SON Climatology

same pattern as that of MAM but the mean precipitation is significantly intensified over the Florida Current and western GS, possibly because the underlying SST is much warmer. By this season, the IFS simulations have also completed the seasonal transition to the summer pattern, with NAC weakened rainfall and shifted main rain belt to the Florida Current and western GS, although all models underestimate the precipitation there (Figs. 3.4b-f). The T1279 model simulates the JJA precipitation most realistically (Fig. 3.4e-f).

In September-November (SON), the observed precipitation centers on the GS extension and the NAC track are re-established while the rainfalls over the Florida Current is weakened (Figs. 3.5a). As a result, the mean precipitation in SON highlights a northward shift toward

the DJF rainfall pattern. Furthermore, there is a general increase of precipitation over a broader area of the North Atlantic, as seen by the expansion of precipitation over 3-4 mm day<sup>-1</sup> (blue shadings). The simulations (Figs. 3.5b-f) reproduce this seasonal transition well, including the shift of the GS precipitation center and broadening of rainfall area over the North Atlantic. Again, the T1279 run produces the most realistic precipitation in the GS extension and NAC track (Figs. 3.5e and 3.5f). This run, however, overestimates the precipitation in the subtropical Atlantic between 30°N-35°N.

Overall, the TMPA Observations show two distinctive precipitation patterns over the Gulf Stream region in boreal winter (DJF) and summer (JJA), featuring strong precipitations over the GS extension and NAC track in the former and over the Florida Current and western GS in the latter. A quick seasonal transition occurs in the spring (MAM) while a more gradual one occurs during the fall (SON). The seasonal change is associated with a transition of rainfall regimes, with an SST gradient-driven convergence within the marine boundary layer over the GS extension and the NAC track but a convective heating over the warm water of the Florida Current and western GS (Minobe et al., 2010). The IFS generally produces a realistic seasonal cycle of the precipitations. The major shortcomings are that the seasonal transition in boreal spring seems to be significantly delayed in all resolution runs and the overall intensity of rainfall is underestimated although the resolution increases do improve the latter. In particular, the IFS simulation on the order of 10 km produces the best simulation in both the magnitude and meridional range of the precipitation over both the Florida Current and the GS extension. It also improves the precipitation over the NAC track significantly.

### 3.2.2 The effects of air-sea coupling

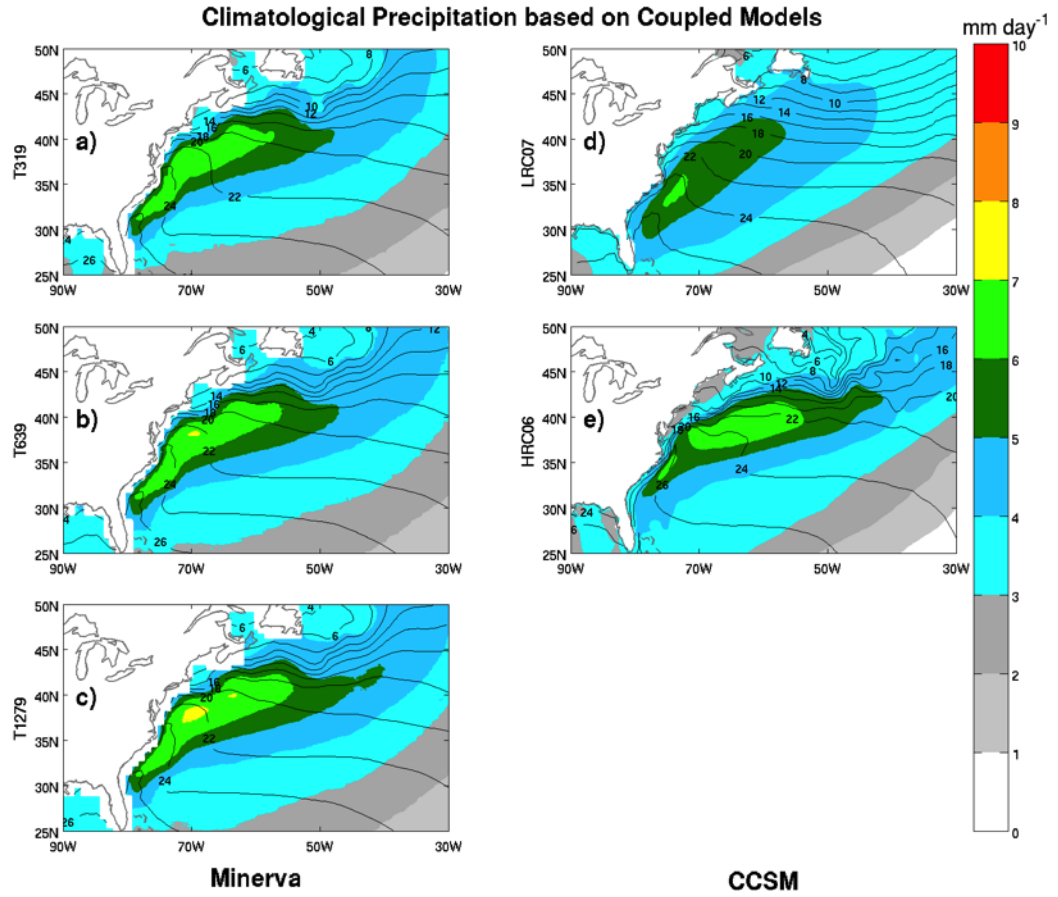


Figure 3.6: The Climatological annual mean precipitation (shading) and SST (contour) from the Minerva hindcasts for 1980-2011 (left column) and CCSM3.5 (right column). Within the left (right) column, the panels from top downward correspond to the increasing atmospheric (oceanic) resolutions. The contour interval is 2C and the shading scale is shown on the right.

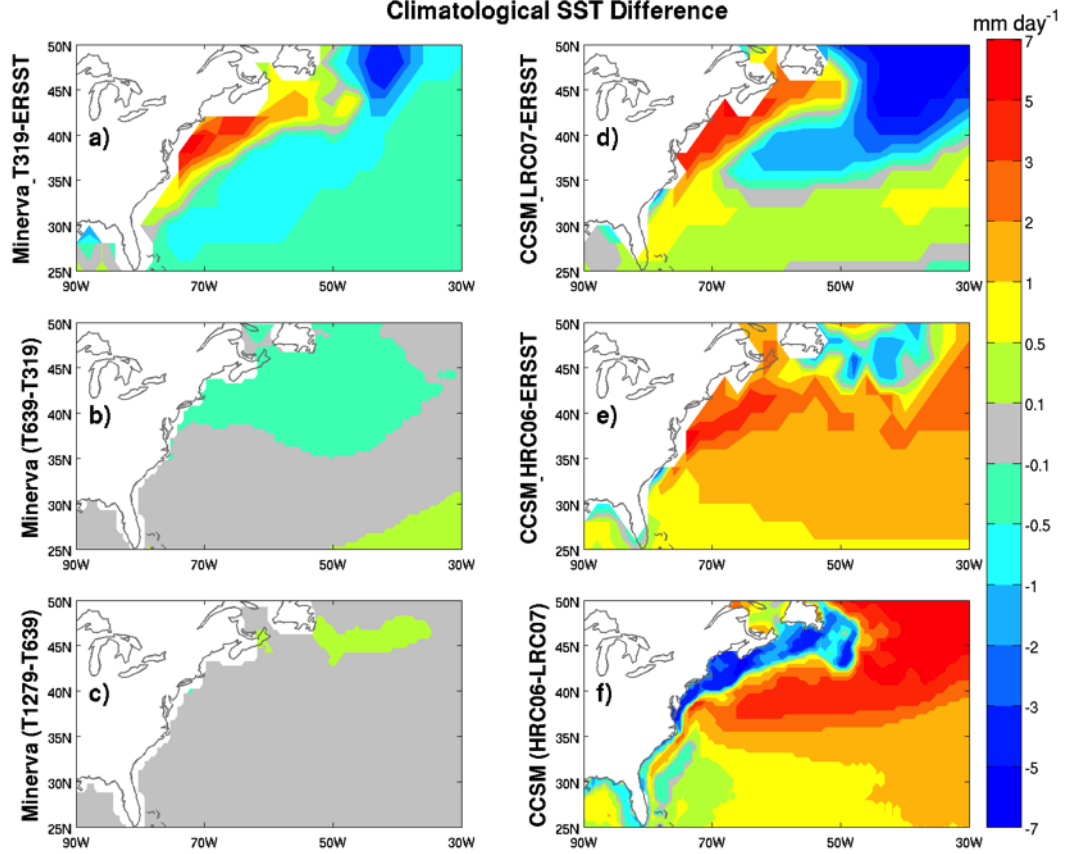


Figure 3.7: (a) Mean SST error of Minerva T319 runs. (b) Mean SST difference between Minerva T639 and T319 ( $T639-T319$ ), and (c) difference between Minerva T1279 and T639 ( $T1279-T639$ ). (d) Mean SST error of CCSM LRC07, and (e) CCSM HRC06. (f) Mean SST difference between CCSM HRC06 and LRC07 ( $HRC06-LRC07$ ).

We further examine the effects of air-sea coupling on the simulated GS precipitation. Figure 3.6 shows the climatological annual mean precipitation (shading) and SST (contour) from the Minerva hindcasts for 1980-2011 (left column) and CCSM3.5 (right column). For Minerva, the annual climatology is averaged from both the summer and winter hindcasts. Comparing the Athena simulations (Fig. 3.1) with their Minerva counterparts (left column, Fig. 3.6), it is clear that the air-sea coupling generally weakens the GS precipitation and also shifts its center southwestward, with enhanced precipitation over the Florida Current

and western GS but weakened precipitation over the GS extension. An increase of the IFS resolution from 62 (Fig. 3.6a) to 16 km (Fig. 3.6c) enhances the center of precipitation modestly. None of the simulations reproduces the secondary center on the NAC track. Similar features are also shown in the LRC run (Fig. 3.6d) of CCSM3.5, where the mean precipitation is weaker and its center ( $\geq 6 \text{ mm day}^{-1}$ ) is shifted further west and oriented along the coast.

The characteristics of these coupled simulations can largely be explained by the deficiencies of the simulated SST climatology near the oceanic front by the non-eddy-resolving OGCMs. In the Minerva runs, the oceanic front is located at  $40^\circ\text{N}$ - $45^\circ\text{N}$  (left panels, Fig. 3.6), further to the north of the observed one (Fig. 3.1a). This is because of an overshoot of the western boundary current separation latitude, which is common in non-eddy-resolving models (Kiehl and Gent, 2004). Moreover, the path of the GS extension and NAC is too zonal after the separation point near the Grand Banks.

Correspondingly, a large area of cold SST bias (Fig. 3.7a), up to  $4^\circ\text{C}$  at its center near  $45^\circ\text{N}$ - $50^\circ\text{N}$  and  $40^\circ\text{W}$ - $50^\circ\text{W}$ , extends from the northeastern North Atlantic toward the American coast near  $30^\circ\text{N}$ , which surrounds a substantial warm bias in the coastal region between  $35^\circ\text{N}$ - $45^\circ\text{N}$ . This error pattern is not sensitive to the increase of the IFS resolution because the mean SST differences between these runs (Figs. 3.7b and 3.7c) are much smaller than their SST errors (not shown), which are very similar to that shown in Fig. 3.7a. As a result, the oceanic frontal precipitation is substantially weakened.

The SST errors of the LRC run (Fig. 3.7d) have a similar pattern to that of the IFS simulations but with even larger magnitude because its SST front is more diffused (contour, Fig. 3.6b). However, as the OGCM resolution of the CCSM3.5 is increased to  $0.1^\circ$ , the SST gradient of the HRC06 run is tightened significantly near  $40^\circ\text{N}$  (contour, Fig. 3.6e). The high-resolution OGCM depicts the oceanic front and jet more accurately although it still seems too zonal. The separation point of the western boundary current is closer to the observed because the more realistic partitioning of the mean and eddy energy levels reduces its dependence on lateral friction (Chassignet and Marshall, 2008). Correspondingly, the

HRC06 precipitation is also improved significantly from the LRC run, as pointed out by (Kirtman et al., 2012). The center of precipitation is oriented more zonally and aligned with the oceanic front. Its magnitude is also enhanced substantially.

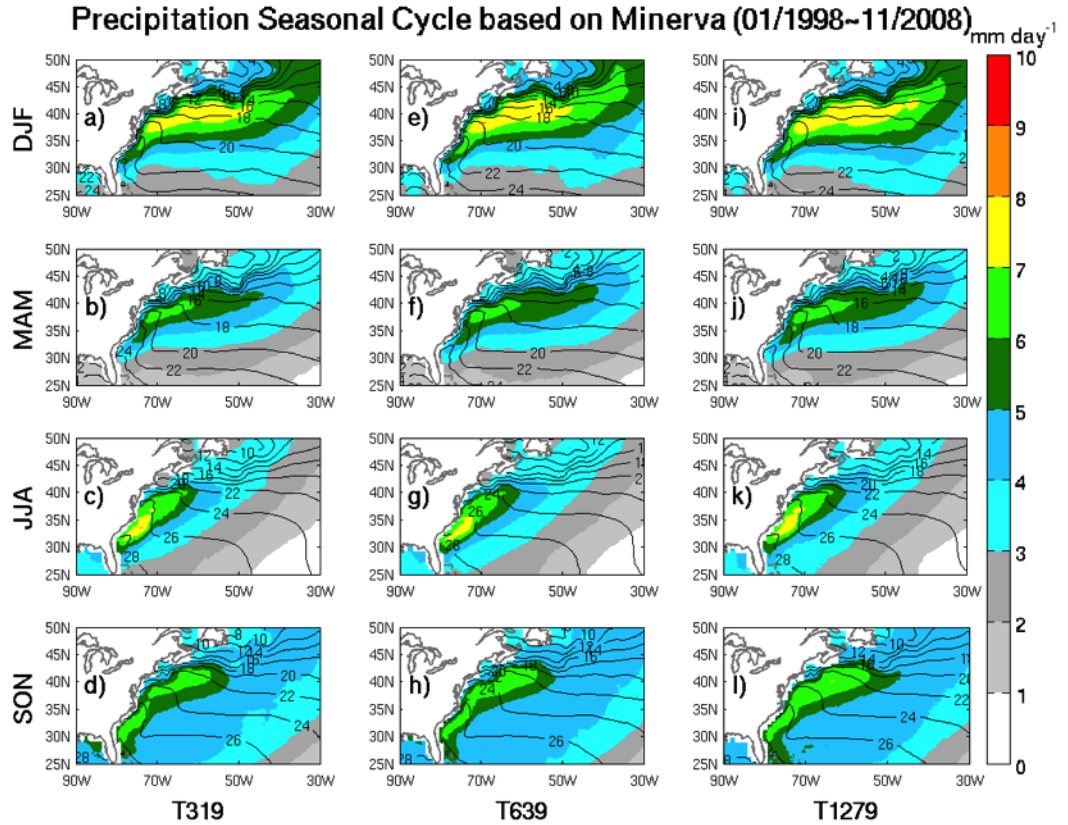


Figure 3.8: Seasonal precipitation climatology (shading) of Minerva simulations at the resolutions of T319 (left panels), T639 (middle panels) and T1279 (right panels). The color bar of precipitation (unit:  $\text{mm day}^{-1}$ ) is on the right. The seasonal SST climatology ( $^{\circ}\text{C}$ ; contours) from the corresponding runs is overlaid on each panel. The contour interval is  $2^{\circ}\text{C}$ . Within each column, the seasonal means of DJF, MAM, JJA and SON are organized from top to bottom.

### Precipitation Seasonal Cycle based on CCSM

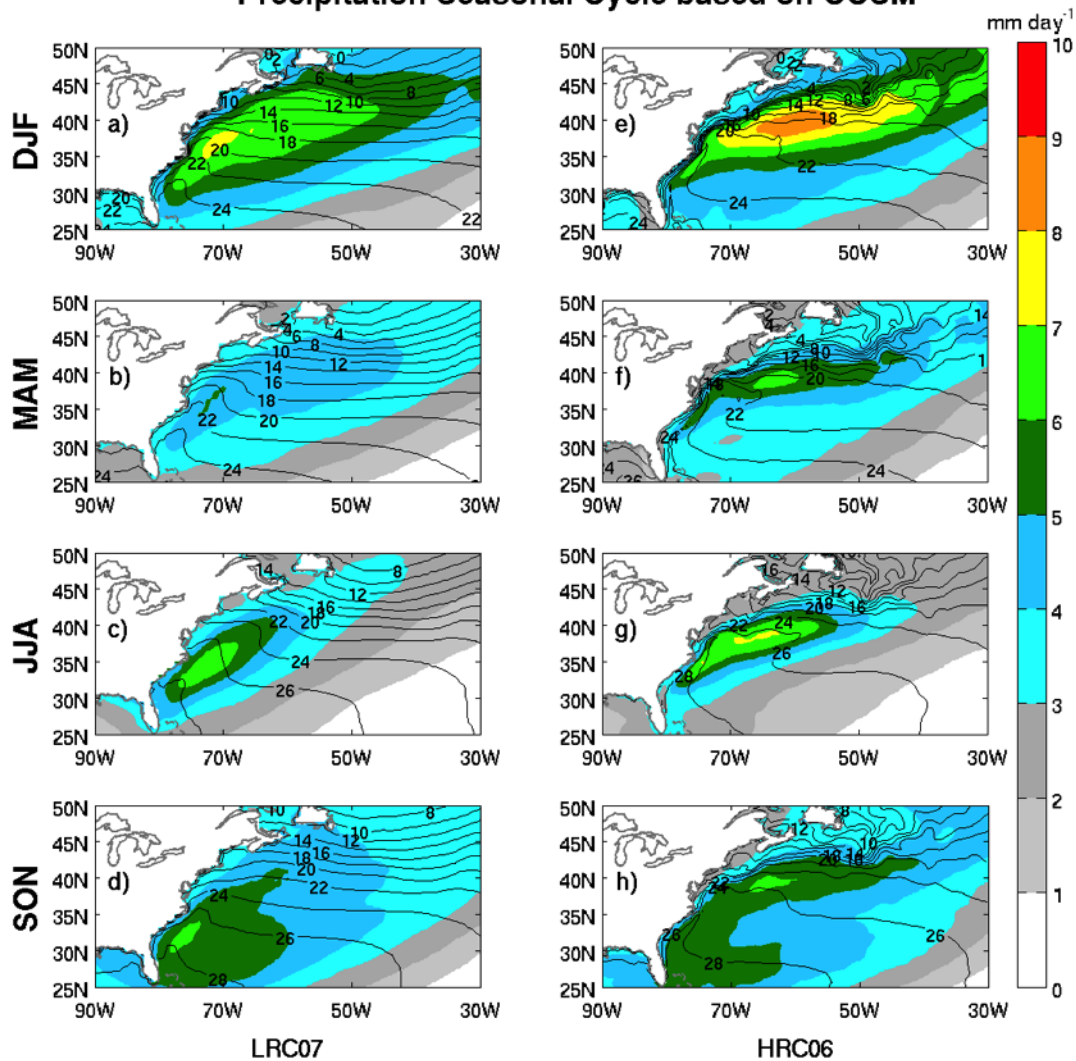


Figure 3.9: Seasonal precipitation climatology (unit:  $\text{mm day}^{-1}$ ; shading) from CCSM3.5 LRC07 and HRC06 coupled model simulations. The model corresponding seasonal SST climatologies are superimposed as contours on the corresponding panels. The contour interval is  $2^{\circ}\text{C}$ . The seasonal means for DJF, MAM, JJA and SON are organized from top to bottom panels and LRC07 and HRC06 runs are in the left and right panels, respectively.

Both the Minerva and CCSM simulations reproduce the annual cycle of the GS precipitation realistically (Fig. 3.8 and Fig. 3.9). In both sets of runs, there is a clear intensification of the mid-latitude rainfall over the GS extension and its westward expansion from SON to DJF. The enhancement of the rainfall over the Florida Current is also well simulated.

The seasonal transition from winter to summer seems better handled by the coupled models than uncoupled ones with a clearer weakening of precipitation and westward withdraw in the former. The fall broadening of the precipitation over the North Atlantic is also simulated realistically. In the Minerva runs, the effect of the increased IFS resolution is a quantitative intensification of precipitation in all seasons (Fig. 3.8). On the other hand, the improvement in the HRC06 simulation is qualitative, with a much more realistic annual cycle than the LRC run (Fig. 3.9). As in the annual mean, the annual cycle in the latter is dominated by the changes over the warm water in the western boundary, with an excessive weakening in MAM. The former, however, shows a clear seasonal transition between the dominant precipitation over the boundary and GS extension.

The above analysis of the three sets of experiments shows that, forced with observed SST, atmospheric models can produce the main characteristics of the rain band over the Gulf Stream region associated with the SST front even at moderate model resolutions. A resolution increase is able to improve the quality of the model simulations in several aspects, especially over the GS extension and the NAC track, simply because the underlying SST gradient can be better seen by the atmosphere. The coupled model simulations fail to reproduce the secondary precipitation center and generally weaken the overall precipitation in the GS region. However, the eddy-resolving ocean model produces qualitative improvements of the SST simulation and has the potential to greatly benefit the quality of the climate simulation in this region.

### 3.3 Potential mechanisms

One potential mechanism for stronger GS precipitation with increased atmospheric and/or oceanic model resolutions is that the storm track is enhanced in the higher-resolution models. However, our examination of the storm track intensity based on dynamical variables does not show clear evidence to support this scenario (Wettstein and Wallace, 2010). Following the framework provided by Minobe et al. (2008), we have also explored whether the mean atmospheric adjustment to the SST gradient plays a role. Using the Lindzen and

Nigam (1987) marine boundary layer model, (Minobe et al., 2008) showed that the Laplacian of the atmospheric sea level pressure ( $\nabla^2$  SLP) forces the near surface convergence  $-(u_x + v_y)$  :

$$-\rho_0(u_x + v_y) = \frac{\epsilon}{\epsilon^2 + f^2} \cdot \nabla^2 SLP \quad (3.1)$$

where  $\rho_0$  is the surface air density,  $\epsilon$  a constant damping coefficient and  $f$  the Coriolis parameter. Minobe et al. (2008) further pointed out the  $\nabla^2$  SLP itself is roughly proportional to the laplacian of the SST with the sign reversed ( $\nabla^2$  SST) where the Laplace operator acts as a high-pass filter to isolate the boundary layer SLP adjustment forced by the SST gradient from other larger-scale atmospheric variations. They also argue that this forced near-surface convergence generates vertical motion above the marine boundary layer and causes divergence in the mid-to-upper troposphere. In the following subsections, we first examine the pattern of the annual mean precipitation, which is representative of the fall and winter precipitation. The summer precipitation is then analyzed separately because it shows some unique features.

### 3.3.1 Annual mean pattern

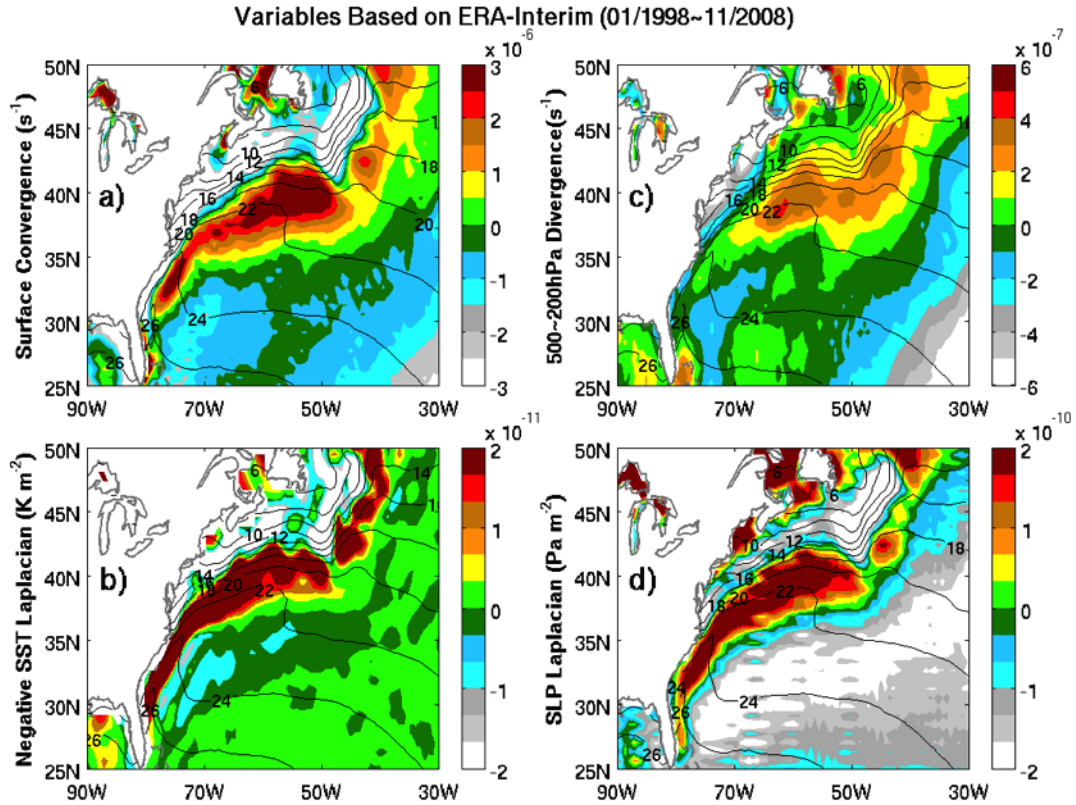


Figure 3.10: Shading: climatologies of (a) surface convergence (unit:  $s^{-1}$ ), (b) negative Laplacian of SST (unit:  $^{\circ}C m^{-2}$ ), (c) 500-200 hPa divergence (unit:  $s^{-1}$ ) and (d) SLP Laplacian (unit:  $Pa m^{-2}$ ) based on ERA-Interim. The corresponding color bar is on the right of each panel. The SST climatology ( $^{\circ}C$ ) from ERA-Interim is overlaid as contours in each panel. The contour interval is  $2^{\circ}C$

Figure 3.10 displays the climatological surface convergence in the Gulf Stream (Fig. 3.10a), negative SST Laplacian (Fig. 3.10b), upper level divergence (Fig. 3.10c) and SLP Laplacian (Fig. 3.10d) from the ERA-Interim reanalysis, all superimposed on the climatological SST (contour). The patterns of (Fig. 3.10d) and (Fig. 3.10b) are similar to each other with maxima over the southern edge of the SST gradient. Consistent with Eq.(1), the SLP Laplacian maxima also overlap with those of the surface wind convergence (Fig. 3.10a),

which also coincide with the location of the TMPA observed rain. Furthermore, the upper-level divergence shows a center in this area (Fig. 3.10b), suggesting that relatively deep circulation is invoked. This relationship confirms the (Minobe et al., 2008) results that the pressure adjustment to sharp SST gradients causes surface wind convergence, which causes ascending motion into the troposphere and divergence in the upper atmosphere.

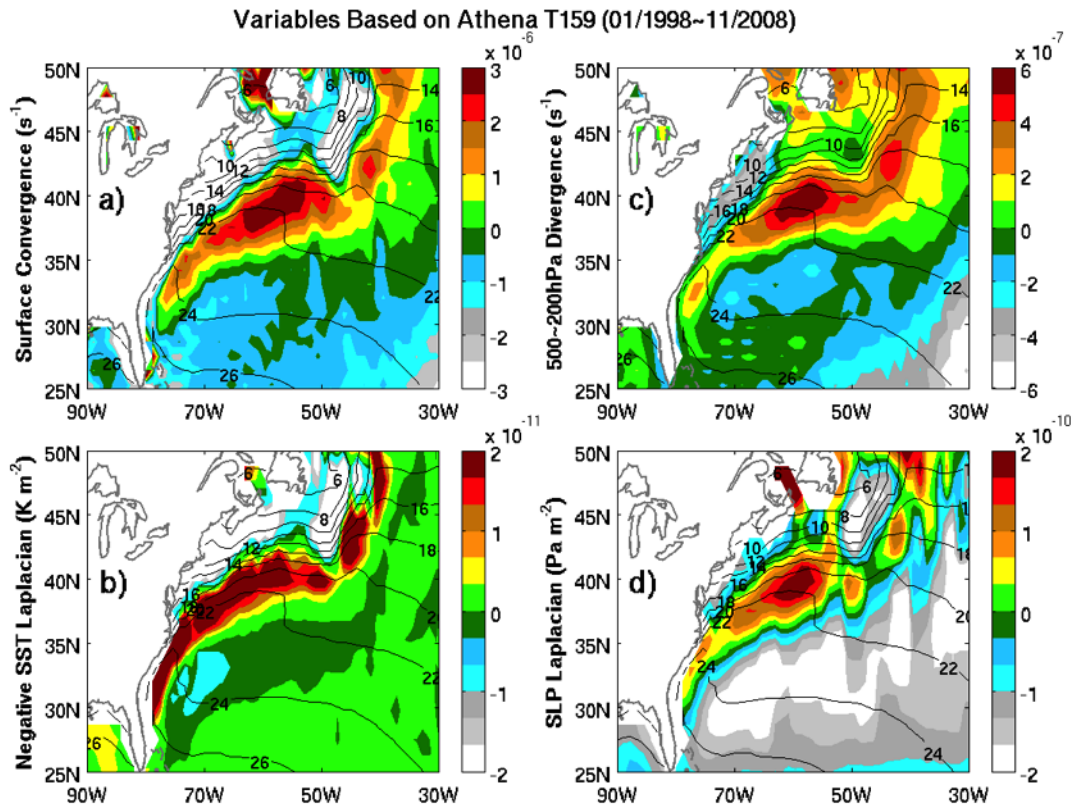


Figure 3.11: Shading: climatologies of (a) surface convergence (unit:  $s^{-1}$ ), (b) negative Laplacian of SST ( $^{\circ}C m^{-2}$ ), (c) 500-200 hPa divergence (unit:  $s^{-1}$ ) and (d) SLP Laplacian (Unit:  $Pa m^{-2}$ ) based on Athena T159. The corresponding color bar is on the right of each panel. The SST climatology ( $^{\circ}C$ ) from T159 is overlaid by contours in each panel. The contour interval is  $2^{\circ}C$ .

Figure 3.11 displays the same variables as in Fig. 3.10, except that they are from the Athena simulation at T159 resolution. In order to remove the noise influence, a 9-point

Variables Based on Athena T1279 (01/1998~11/2008)

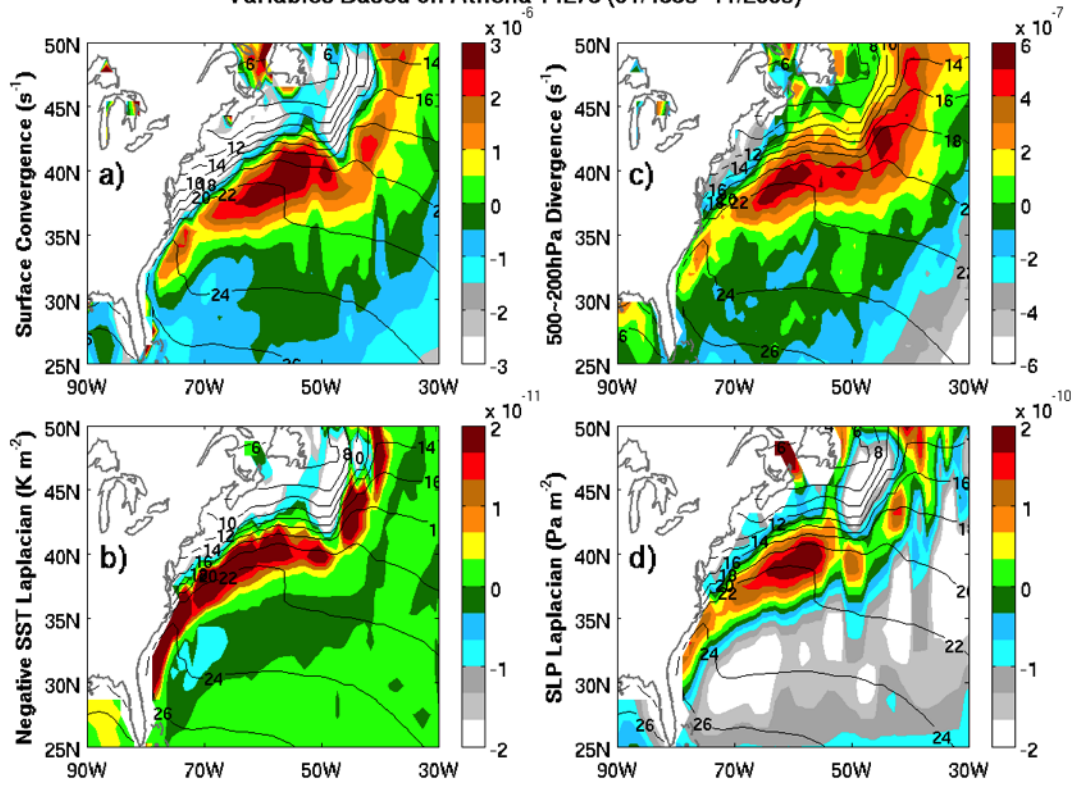


Figure 3.12: Shading: climatologies of (a) surface convergence (unit:  $s^{-1}$ ), (b) negative Laplacian of SST (unit:  $^{\circ}C m^{-2}$ ), (c) 500-200 hPa divergence (unit:  $s^{-1}$ ) and (d) the SLP Laplacian (unit:  $Pa m^{-2}$ ) based on Athena T1279. The corresponding color bar is on the right of each panel. The SST climatology ( $^{\circ}C$ ) from T1279 is overlaid as contours in each panel. The contour interval is  $2^{\circ}C$

smoothing is applied to the fields of the SST and SLP Laplacian of the model outputs. It is clear that the model reproduces the observational processes qualitatively, although the response of the SLP Laplacian near the SST front is weaker (Fig. 3.11d). We have also examined these quantities from other Athena runs with higher resolutions. Figure 3.12 shows the same quantities as those in Fig. 3.11, except that they are from the T1279 run.

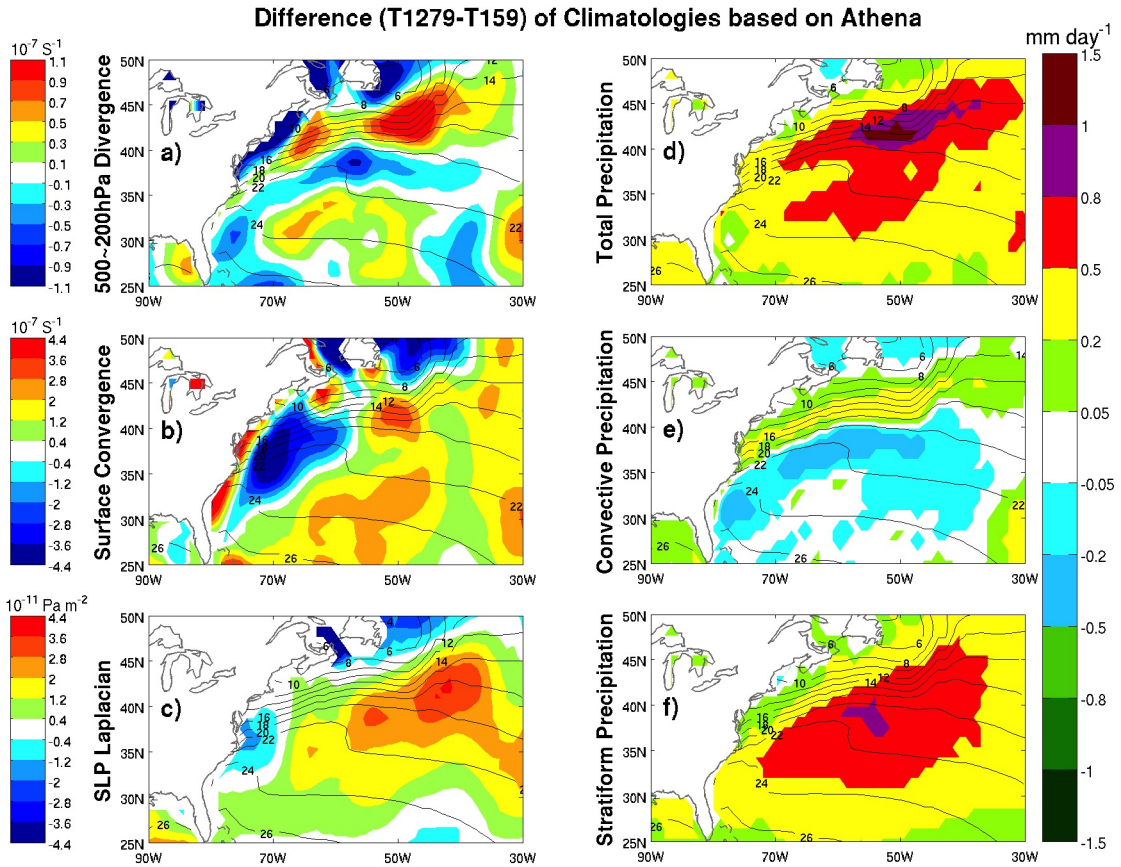


Figure 3.13: Shading: climatological differences (Athena T1279-T159) of (a) 500-200 hPa divergence (unit:  $\text{s}^{-1}$ ), (b) surface convergence (unit:  $\text{s}^{-1}$ ), (c) the SLP laplacian (unit:  $\text{Pa m}^{-2}$ ), (d) total precipitation, (e) convective precipitation and (f) stratiform precipitation. The unit of precipitation is (unit:  $\text{mm day}^{-1}$ ). The corresponding color bar is on the right of each panel. The SST climatology ( $^{\circ}\text{C}$ ) from T159 is overlaid as contours in each panel. The contour interval is  $2^{\circ}\text{C}$ .

The left panels of Fig. 3.13 further show the differences between the two runs in the

upper (Fig. 3.13a) and lower (Fig. 3.13b) atmosphere, as well as the SLP Laplacian (Fig. 3.13c). These figures suggest that the SST gradient induced convergence process is enhanced modestly as the model horizontal resolution increases. Furthermore, decomposing the difference of total precipitation between the two runs (Fig. 3.13d) into its convective (Fig. 3.13e) and stratiform (Fig. 3.13f) components, it can be seen that the spatial patterns of the SLP Laplacian (Fig. 3.13c) and stratiform precipitation (Fig. 3.13f) are similar to each other, which are generally broadened toward the warm side of the SST gradient. On the other hand, the upper atmospheric divergence (Fig. 3.13a) and the convective precipitation (Fig. 3.13e) are more similar to each other, with the convective rain belt narrowly confined in a zone of the high SST gradient. It suggests that only the portion of the enhanced surface convergence near the oceanic front contributes to the deep convection into the upper atmosphere. It should be noted that, since the wind and SLP outputs from the higher-resolution model runs have already been truncated to T159, the contribution of the smaller-scale atmospheric fluctuations could not be counted in these calculations. It is still possible that some precipitation change is likely generated by the smaller-scale processes directly.

The Minerva simulations demonstrated somewhat similar features to those of Athena (not shown). This is mainly because the responses of the non-eddy-resolving OGCM to the AGCMs with different resolutions are very similar. As discussed in the preceding section, The mean SST differences between the Minerva T319 run and the T639 (Fig. 3.7b) and T1279 (Fig. 3.7c) are less than  $0.5^{\circ}\text{C}$ . On the other hand, the OGCM resolution increase in the CCSM3.5 runs generates much more dramatic changes in the mean SST. As the OGCM resolution is increased to the eddy-resolving level, however, the mean SST front in HRC06 is sharper than those from the observations (Fig. 3.7e). As a result, the mean SST difference between HRC06 and LRC07 (Fig. 3.7f) shows a reversed pattern of Fig. 3.7d.

Variables Based on CCSM LRC07

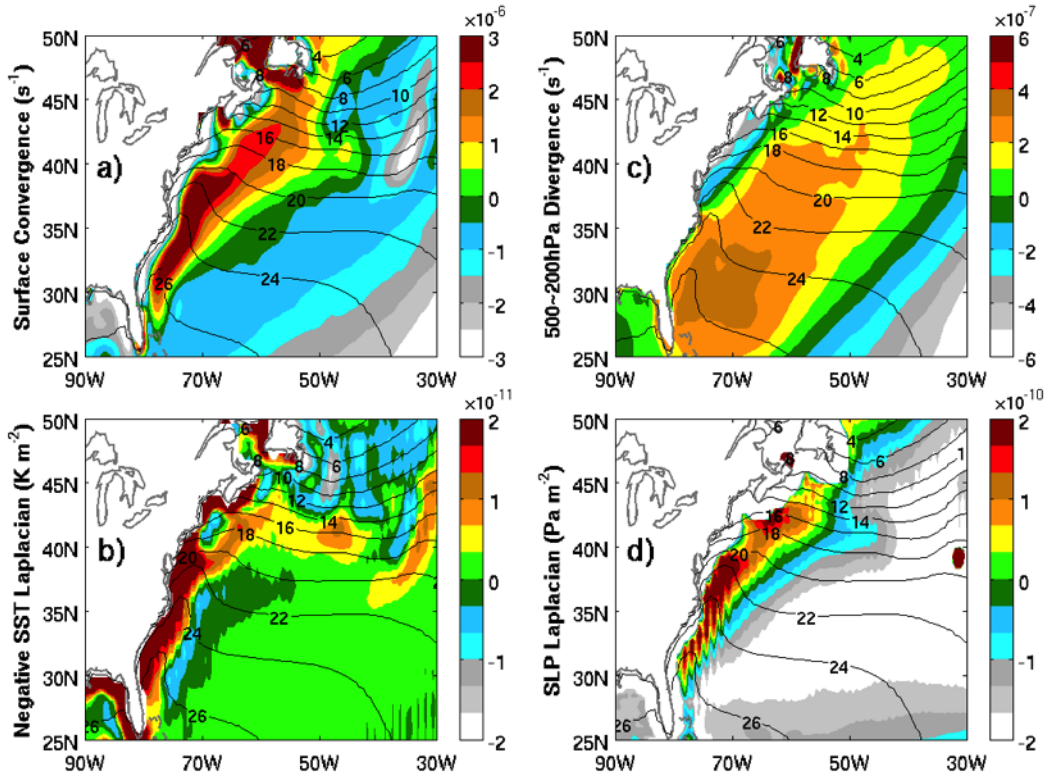


Figure 3.14: Shading: climatology of (a) surface convergence (unit:  $s^{-1}$ ), (b) negative laplacian of SST (unit:  $^{\circ}C m^{-2}$ ), (c) 500-200 hPa divergence (unit:  $s^{-1}$ ) and (d) the SLP Laplacian (unit:  $Pa m^{-2}$ ) based on CCSM3.5 LRC07. The corresponding color bar is on the right of each panel. The model SST climatology ( $^{\circ}C$ ) is overlaid as contours in each panel. The contour interval is  $2^{\circ}C$

Variables Based on CCSM HRC06

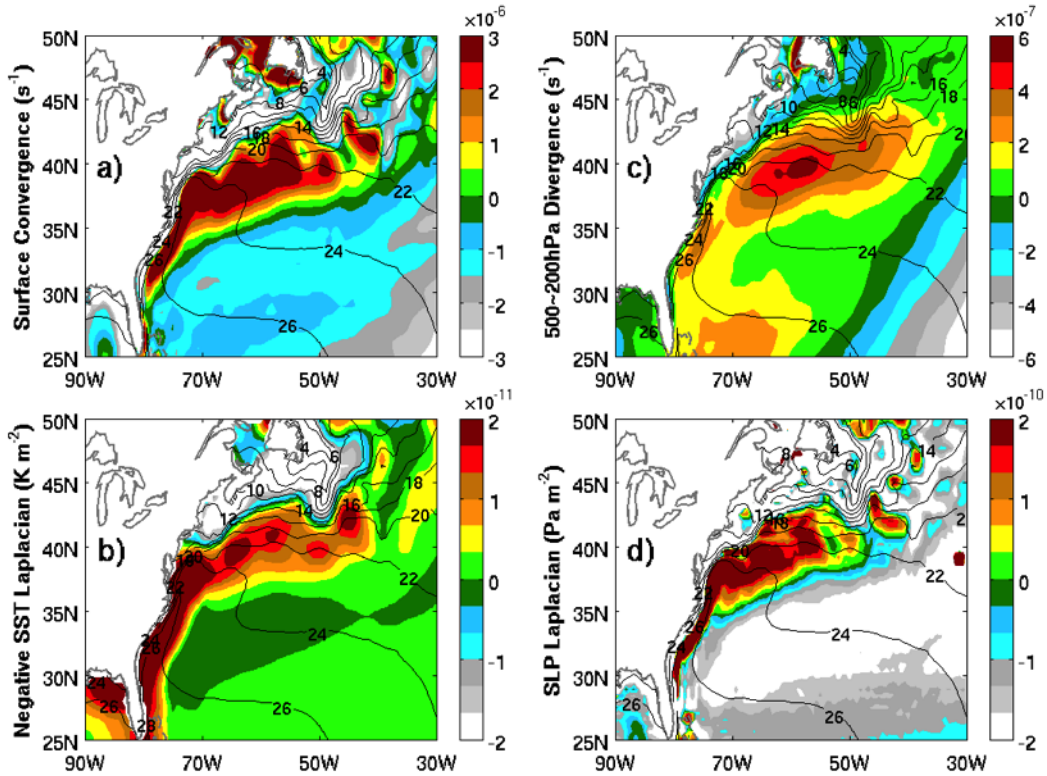


Figure 3.15: Shading: climatology of (a) surface convergence (unit:  $s^{-1}$ ), (b) negative Laplacian of SST (unit:  $^{\circ}C m^{-2}$ ), (c) 500-200 hPa divergence (unit:  $s^{-1}$ ) and (d) the SLP Laplacian (unit:  $Pa m^{-2}$ ) based on CCSM3.5 HRC06. The corresponding color bar is on the right of each panel. The model SST climatology ( $^{\circ}C$ ) is overlaid as contours in each panel. The contour interval is  $2^{\circ}C$

This mean SST difference may explain the substantially different atmospheric patterns between the LRC07 and HRC06 simulations. Figure 3.14 shows that, associated with the weak SST front in LRC07, strong surface convergence (Fig. 3.14a), as well as the Laplacians of both SST (Fig. 3.14b) and SLP (Fig. 3.14d), are limited to the coastal regions, away from the GS extension. Furthermore, in the upper level, there is a broad pattern of divergence (Fig. 3.14c) with its center over the warmest water in the southwest, which is quite different from the narrow convergence belt in the boundary layer (Fig. 3.14a). This implies that the upper level divergence, i.e., the deep convections, in this region is not mainly forced by the SST gradient induced surface convergence. This point will be further illustrated in the

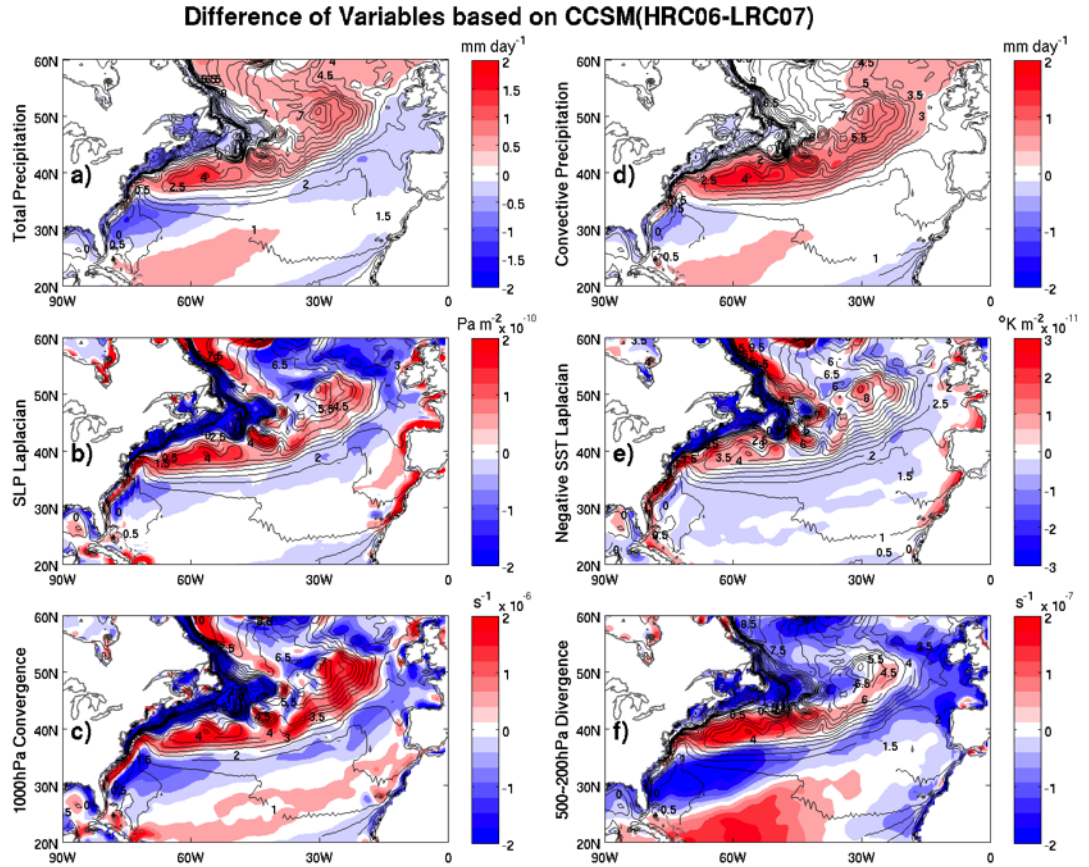


Figure 3.16: Climatological differences (shadings) between the CCSM3.5 HRC06 and LRC07 simulations. The SST climatology differences ( $^{\circ}\text{C m}^{-2}$ ) are overlaid as contours on all panels. Difference is defined as HRC06-LRC07. The order of this figure is (a) total precipitation climatology (unit:  $\text{mm day}^{-1}$ ), (b) SLP Laplacian (unit:  $\text{Pa m}^{-2}$ ), (c) 1000 hPa convergence (unit:  $\text{s}^{-1}$ ), (d) convective precipitation (unit:  $\text{mm day}^{-1}$ ), (e) negative SST Laplacian (unit:  $^{\circ}\text{C m}^{-2}$ ) and (f) 500-200 hPa divergence (unit:  $\text{s}^{-1}$ ). The shading scales are on the right side of their corresponding panels.

next subsection. In HRC06, however, the patterns in the atmospheric boundary layer and the upper levels are much more consistent with each other (Fig. 3.15). The centers of the actions are also moved to the GS extension where the SST gradient is strongest. Compared with LRC07, the increase of the total precipitation in the GS extension (shading, Fig. 3.16a) over the enhanced SST gradient there (contour, Fig. 3.16a) is predominantly due to the convective precipitation (shading, Fig. 3.16b). This increase is closely associated with the enhanced Laplacians of the SLP (Fig. 3.16c) and SST (Fig. 3.16d). Moreover, the enhancement of the surface convergence (shading, Fig. 3.16e) and divergence in the upper troposphere (Fig. 3.16f) also occurs in this region. This suggests that the mechanism outlined by (Minobe et al., 2008) functions much more efficiently in HRC06 than in LRC07.

### 3.3.2 Summer pattern

We have also examined the seasonal changes of these variables. In general, the fall and winter patterns are very similar to that in the annual means described above. The patterns in the spring and summer, however, suggest some qualitative differences in the scenario. In this subsection, we analyze the mechanisms of the summer precipitation pattern in the GS region. As we have pointed out in Section 3.1, a major seasonal change of the GS precipitation is a southwestward shift of the main rain belt from winter to summer. Figure 3.17 shows the upper level divergence from the summer (JJA) season and the boundary layer convergence generated by the SST gradient, as represented by the SLP Laplacian from the ERA-Interim analysis and the Athena T159 and T1279 simulations. Comparing with the corresponding panels in Fig. 3.4, it can be seen that the upper level divergences (Figs. 3.17a-c) match very well with the major precipitation centers over the Florida Current and the western GS where the SST is relatively higher. The SST gradient induced surface convergence from the observations (Fig. 3.17d), which forms a narrow band over the warm side of the SST front, contributes to the upper level divergence and accounts for the divergence center (Fig. 3.17a), where the strongest precipitation occurs. On the other hand, the patterns of the upper level divergence and the SST gradient induced boundary layer

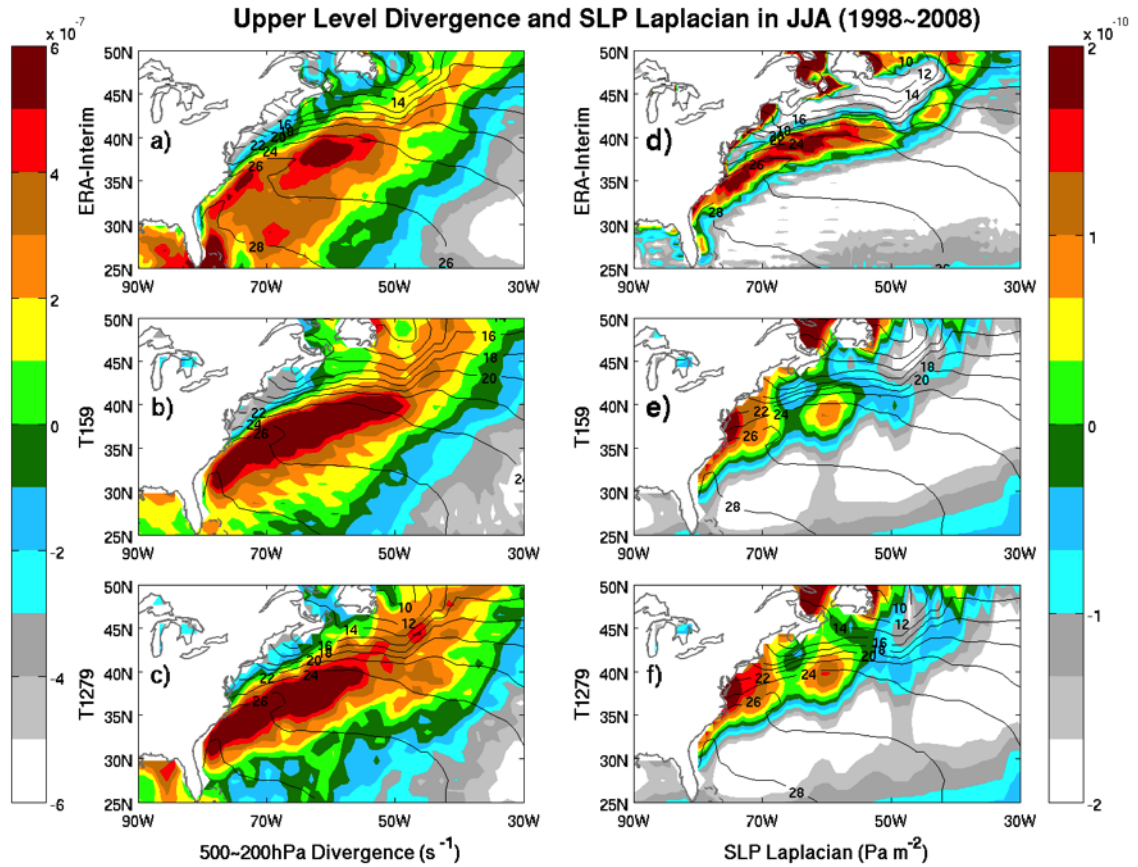


Figure 3.17: The shading in the left panels shows the JJA climatologies of the 500-200 hPa divergence (unit:  $\text{s}^{-1}$ ) for (a) ERA-Interim, (b) Athena T159 and (c) Athena T1279. The corresponding shading scale is on the left of these panels. The shading in the right panels shows the JJA climatologies of the SLP Laplacian (unit:  $\text{Pa m}^{-2}$ ) for (d) ERA-Interim, (e) Athena T159 and (f) Athena T1279. The corresponding shading scale is on the right of these panels. The JJA climatologies of SST the ERA-Interim data and the Athena simulations are superimposed as contours with  $2^\circ\text{C}$  interval on the corresponding panels.

convergence, as represented by the Laplacian of the SLP, shows larger differences, in comparison to the more consistent patterns between them in the annual means. In particular, the area of the 500-200 hPa level mean divergence is broader over the tropical-subtropical ocean and more organized than the boundary layer convergence. Moreover, the summer upper level divergence is stronger than the annual mean one (Fig. 3.10c), although the surface convergence in summer (not shown) is weaker than the corresponding annual mean. The weakening of the boundary layer divergence from winter to summer is consistent with the weaker SST gradient across the oceanic front in the GS extension during the summer. We speculate that, as the SST gradient weakens, the upper level divergence is shifted southwestward over the Florida Current and the western Gulf Stream, where deeper convections may be generated over the warmer water with a more elevated heat source in the mid-atmosphere. In fact, Minobe et al. (2008) have pointed out that deeper convection mainly occurs in summer over the Florida Current and the western Gulf Stream. It seems that these two regimes of precipitation compete with each other for dominance in the area. It is interesting to note that, even in the annual mean state, major precipitation and the upper level divergence is shifted southwestward toward the Florida Current and the western Gulf Stream in LRC07 because the SST gradient is weaker in the GS extension.

Similar structural differences between the upper and lower levels can also be seen from the Athena simulations. In the models, a deep-layer convergence over the warm water may play a more important role because the SST gradient induced boundary layer convergence is more disorganized (Figs. 3.17e and 3.17f). The JJA differences between the T1279 and T159 runs (Fig. 3.18) show that the AGCM resolution increase mainly enhances the surface convergence (Figs. 3.18b and 3.18c) and upper level divergence (Fig. 3.18a) near the SST front, which enhances the precipitation there (Fig. 3.18d), especially the stratiform precipitation (Fig. 3.18f). However, the effect of the AGCM resolution increase is quite moderate on the magnitude of precipitation.

We have also examined the pattern of the summer precipitation simulated by the NICAM model, which includes eight runs initialized on May 21 and finishing on August 31 for

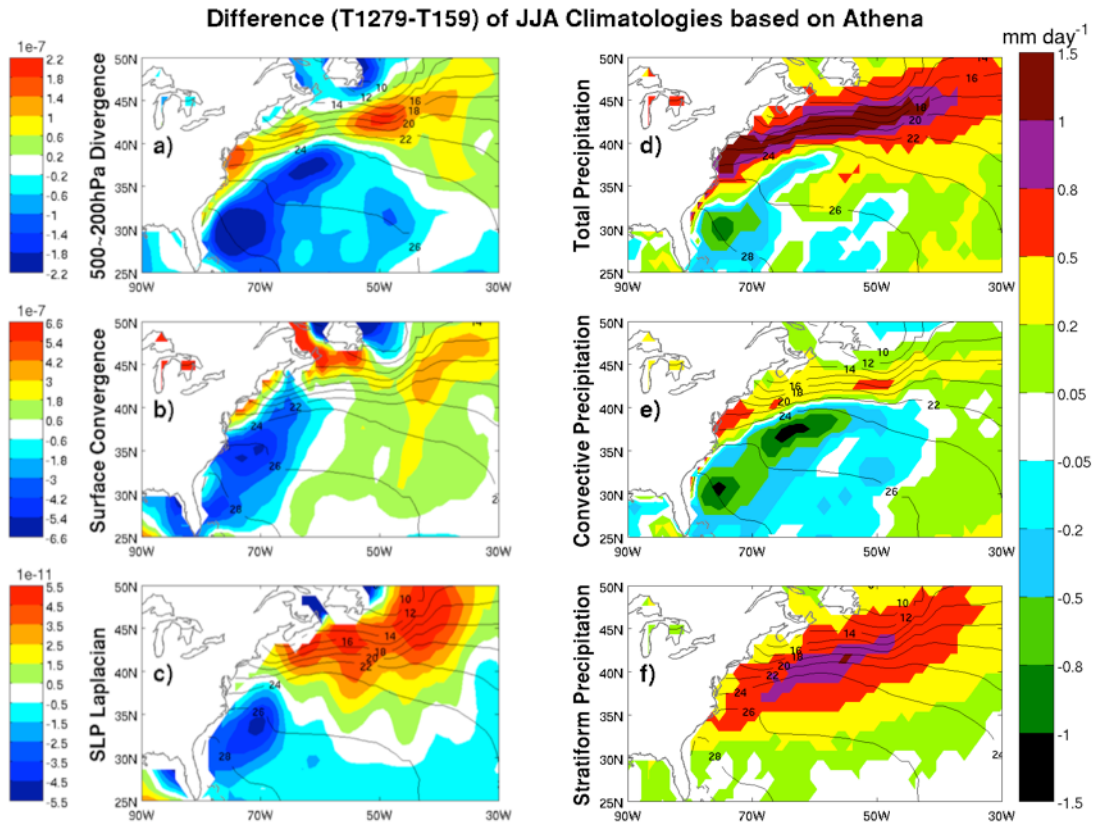


Figure 3.18: Shading: JJA climatological differences (Athena T1279-T159) of (a) 500-200 hPa divergence (unit:  $\text{s}^{-1}$ ), (b) surface convergence (unit:  $\text{s}^{-1}$ ), (c) the SLP Laplacian (unit:  $\text{Pa m}^{-2}$ ), (d) total precipitation, (e) convective precipitation and (f) stratiform precipitation. The unit of precipitation is (unit:  $\text{mm day}^{-1}$ ). The corresponding color bars are on the left side of left panels. The color bar for precipitation is on the right side of the right column. The SST ( $^{\circ}\text{C}$ ) climatology from T159 is overlaid as contours in each panel. The contour interval is  $2^{\circ}\text{C}$

Variables based on NICAM in JJA

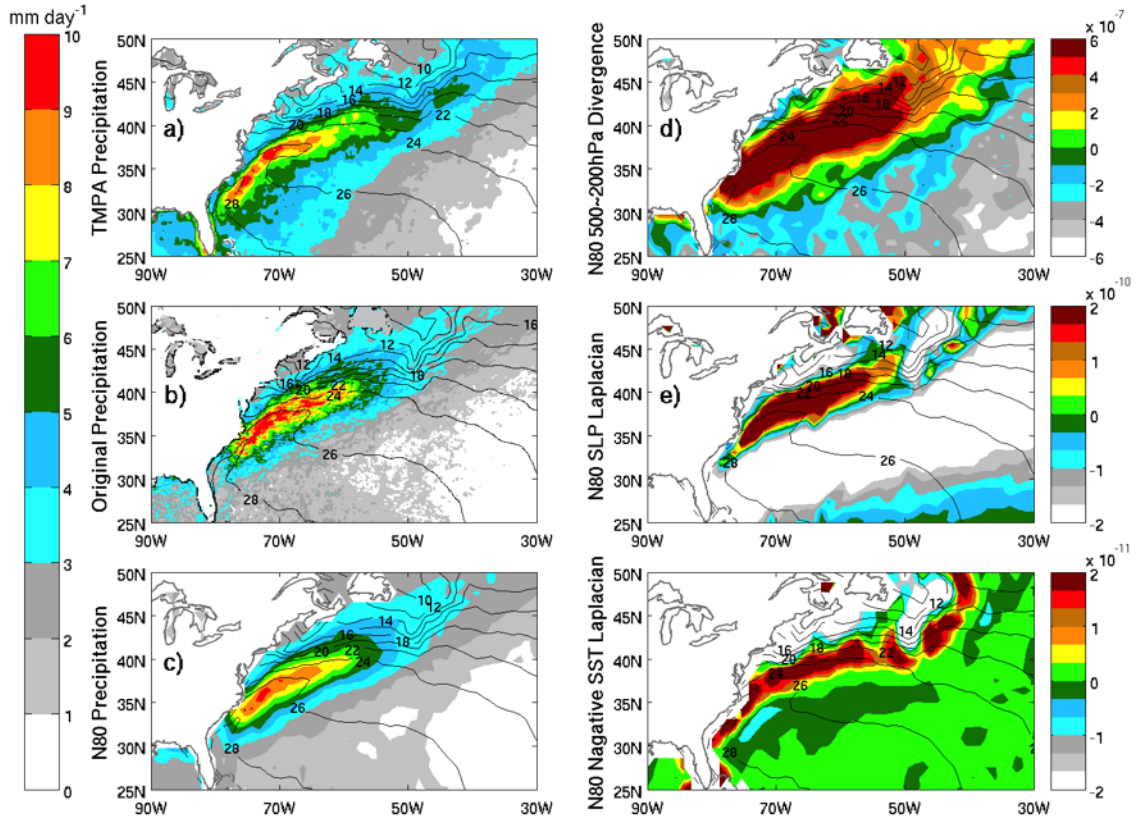


Figure 3.19: The shading in the left panels shows the JJA climatologies of the precipitation (unit:  $\text{mm day}^{-1}$ ) for (a) TMPA and the NICAM simulation on (b) native resolution and (c) reduced resolution (N80). The corresponding shading scale is on the left of these panels. The shading in the right panels shows the JJA climatologies of (d) 500-200 hPa divergence ((unit:  $\text{s}^{-1}$ ), (e) the SLP Laplacian (unit:  $\text{Pa m}^{-2}$ ) and (f) SST Laplacian (unit:  $\text{Pa m}^{-2}$ ) for the NICAM simulation. The corresponding shading scale is on the right of these panels. The JJA climatology of SST from the quarter-degree OISSTv2 data is superimposed as contours with  $2^\circ\text{C}$  interval on all panels. The climatology is based on the 9-year average from 2001 to 2009, except for 2003.

every year from 2001 to 2009, except for 2003 (Kinter et al., 2013). In comparison with the Athena models (e.g., T1279), NICAM has higher horizontal resolution of 7 km and is non-hydrostatic (Kinter et al., 2013). The simulations are also forced with daily SST observations at the horizontal resolution of a quarter degree, which, among other things, better represents the SST front and its variability in the Gulf Stream region (e.g., Small et al. 2014). Our results show that, compared with Athena T1279 (Fig. 3.4d), the NICAM runs show stronger mean summer precipitation in the GS region (Figs. 3.19b and 3.19c), which is closer to the observations (Fig. 3.19a). This seems to be partly attributable to an enhanced surface convergence, as represented by the SLP Laplacian (Fig. 3.19e), forced by the SST Laplacian near the oceanic front (Fig. 3.19f). On the other hand, the upper-level divergence (Fig. 3.19d) still shows a broader structure than the boundary layer properties, suggesting that the ascending motion in this region is also forced by deeper convections over the warmer water.

### 3.4 Summary and discussion

Using simulations from multiple climate models, we have investigated the influences of horizontal resolutions in both of their atmospheric and oceanic model components on the simulated mean precipitation over the Gulf Stream (GS) region. In particular, three sets of model simulations are analyzed. The first two examine the effects of increasing horizontal resolution of an AGCM gradually from around 100 to near 10 km under two fixed oceanic settings. Specifically, the AGCM is either forced with prescribed observational SST in the first case or coupled to an OGCM at a fixed horizontal resolution near 100 km that is not eddy resolving in the second case. The third set of experiments examines the effects of the oceanic resolution with a pair of long-term simulations by another CGCM, in which the OGCM is run respectively at non-eddy-resolving (100 km) and eddy-resolving (10 km) resolutions, while the AGCM resolution remains fixed at around 50 km for both runs.

Observationally, the Gulf Stream in the North Atlantic largely forces a narrow rain belt

that is attached to the tight SST gradient associated with the oceanic front. Seasonally, there is a clear annual cycle with its main precipitations concentrated near the GS extension and NAC track in boreal fall and winter and retreated southwestward to the Florida Current and the western GS. Our results show that all simulations reproduce qualitatively these gross features of the mean GS precipitation and its annual cycle. At similar AGCM resolutions, the uncoupled models produce more realistic GS rain band in both structure and strength than the coupled models with non-eddy-resolving oceans do. This is because the prescribed observational SST better represents the gradient near the oceanic front than the non-eddy-resolving OGCMs simulate although both are nominally generated on a  $1^\circ \times 1^\circ$  resolution. An increase from the baseline AGCM resolution yields enhanced GS precipitation climatology in both large-scale and convective precipitation in the North Atlantic, with the latter more tightly confined to the oceanic front. The enhancement, however, is moderate and further increase in resolution achieves diminishing results. On the other hand, an increase in oceanic resolutions from non-eddy-resolving to eddy-resolving regimes results in more consistent simulations with observations in both intensity and structure of the rain band. The major increase is in the convective precipitation near the much-tightened SST gradient associated with the oceanic front. Therefore, increasing from current base resolutions, the intensity improvement caused by oceanic resolution increases is more effective than that from atmospheric resolution increases.

Further analyses show that the improvement of the Gulf Stream precipitation climatology due to model horizontal resolution increases can be understood in terms of the atmospheric surface pressure adjustment to sharper SST gradients near the oceanic front, which leads to stronger atmospheric convergence in the atmospheric boundary layer. The ascending motion at the top of the boundary layer seems to affect the upper level divergence. This associated ascending motion contributes to the precipitation band located in the Gulf Stream. Our result also shows that this mechanism is most effective in the winter circulation. During the summer, the convection over the warm water of the Florida Current and the western Gulf Stream seems to play a stronger role in enhancing the upper level

divergence, in addition to the SST gradient induced boundary layer convergence.

Our results are based on a comprehensive examination of several model simulations in both coupled and uncoupled settings. This is because it is hard to use a single system to conduct such a wide range of simulations to test the sensitivity of both the atmospheric and oceanic resolutions in a variety of settings and combinations. One caveat of this approach is that factors other than the resolution may contribute to the model differences we have discussed here. For instance, the relatively weak GS precipitation in the CCSM3.5 LRC07, in comparison to the Minerva runs (e.g., T319), is possibly because the former also has fewer vertical levels to resolve the highly baroclinic vertical structures in this region. Moreover, it is also not clear whether the fact that NICAM better simulates the summer precipitation than Athena T1279 is due to its non-hydrostatic formulation or the better SST forcing. On the other hand, we do find from the analysis of these different models a coherent picture about the influence of the model resolution in the simulation of this region and the basic mechanisms by which such effects are achieved.

## **Chapter 4: Rainfall frequency and distribution changes associated with global warming in 16 km Athena simulations**

### **4.1 Introduction of changes in precipitation characteristics in a warm climate**

Under greenhouse gas warming, an increase in the downward flux of infrared radiation at the surface is compensated, in part, by an increase in surface evaporation, and a concomitant increase in precipitation. The increase in evaporation yields an increase in the absolute humidity of the atmosphere. Global climate models generally agree that relative humidity remains roughly constant with greenhouse gas warming, suggesting that absolute humidity of the troposphere may increase at a rate of  $6.5\% K^{-1}$  according to the Clausius-Clapeyron relation. Trenberth (1999) argues that the higher absolute humidity in the warming climate (due to higher temperature and constant RH) would result in storms that generate higher rain rate (i.e.,  $\sim 7\% K^{-1}$ ) because the amount of precipitation generated in a storm is controlled primarily by the amount of moisture converging at the base of storm. Trenberth (1999) further argues that such storms rain out faster than evaporation can restore the atmospheric humidity, and therefore an increase in the frequency of high rain-rate events may occur at the expense of low rain-rate events. Since the change in the overall intensity of precipitation is controlled by the availability of energy at the surface (Allen and Ingram, 2002), climate models predict that the intensity of the global hydrology cycle increases by about  $1\%-2\% K^{-1}$ . This also implies that there must be decreases in light or moderate precipitation and/or a decrease in the frequency of precipitation events (Trenberth et al., 2003). Climate change scenarios simulated by several global climate models yield predictions of increased frequency of intense precipitation (Gordon et al., 1992; Gregory and Mitchell,

1995; Semenov and Bengtsson, 2002; Wilby and Wigley, 2002).

Changes in the frequency of rain naturally imply that periods of flood and drought are likely to change as greenhouse gas forcing increases, with impacts on hydrology, agriculture, and water resources. Changes in precipitation extremes are of great importance to society and the entire ecosystem. Increases in heavy precipitation can increase surface runoff leading to more frequent and intense floods and mudslides. On the other hand, decreases of light and moderate precipitation can lengthen dry spells and increase the risk of drought, dust pollution, and forest fire because light and moderate precipitation is a critical source of soil moisture as well as ground water.

More recent analyses of CMIP5 model projections for the GHG warming simulations show an increase of heavy rainfall accompanied by a decrease in the moderate to light rainfall (Lau et al., 2014). These changes are also linked to shifts of the probability distribution of rainfall using a parametric model (Pandergrass and Hartmann, 2014). These model studies are based on monthly data over grid sizes from about  $1^\circ$  to  $2.5^\circ$  resolutions. It is recognized that statistics of rainfall distributions are strongly dependent on the spatial and temporal scales of the sampling (Kedem et al., 1990). When comparing high resolution (a few km) remote sensing data to model data, Stephens et al. (2010) used a model to convert spaceborne radar data to various model grid sizes to enable comparison.

The aim in this study is to investigate the changes in the different categories and regions of precipitation under global warming by analyzing the very high resolution, multi-decadal runs of ECMWF at resolution T1279 developed by the Project Athena. These data are derived from uncoupled ECMWF simulations, with a horizontal resolution of  $\sim 16$  km and a temporal resolution of 6 hourly. Two multi-decadal runs are made. The Atmospheric Model Intercomparison Project (AMIP) runs cover the period from 1961-2007, and a time-slice simulation covers 2071-2117. Time-slice simulations are performed under the Intergovernmental Panel on Climate change (IPCC) Special Report on Emission Scenarios (SRES). As a comparison, results from the coarse resolution T159 are also analyzed to examine the dependence on resolution.

## 4.2 Data and analysis method

A major objective of the Athena Project is to demonstrate the benefit of more realistic representation of mesoscale and subseasonal scale atmospheric phenomena on climate and weather analyses. Jung et al. (2012) found that increasing horizontal resolution improves the tropical precipitation, the tropical atmospheric circulation, the frequency of occurrence of Euro-Atlantic blocking, and the representation of extratropical cyclones in large part of the Northern Hemisphere extratropics. All of these improvements come from the increase in resolution from T159 to T511, with relatively small changes from further resolution increases to T1279 and T2047. In this chapter, we compare the data with the horizontal resolutions of T159 and T1279 for resolution dependence and focus on T1279 as it provides high spatial resolution not commonly analysed for climate change studies. Please refer to section 2 for the description of experimental setups including AMIP style and time-slice.

## 4.3 Results

### 4.3.1 Latitudinal distribution of precipitation change in amount, intensity and frequency

We compared the T159 simulation with the GPCP 2.5° monthly data set and the T1279 with TRMM 3B43 over the tropic and subtropics. Major rain features such as the ITCZ, SPCZ, and coastal storm tracks are well simulated for both AMIP and TS. The fine resolution T1279 shows finer details such as the rainfall minimum slightly south of the equator separating the ITCZ and the SPCZ. These refined features are not clearly evident at coarse resolutions, both for the model and observations.

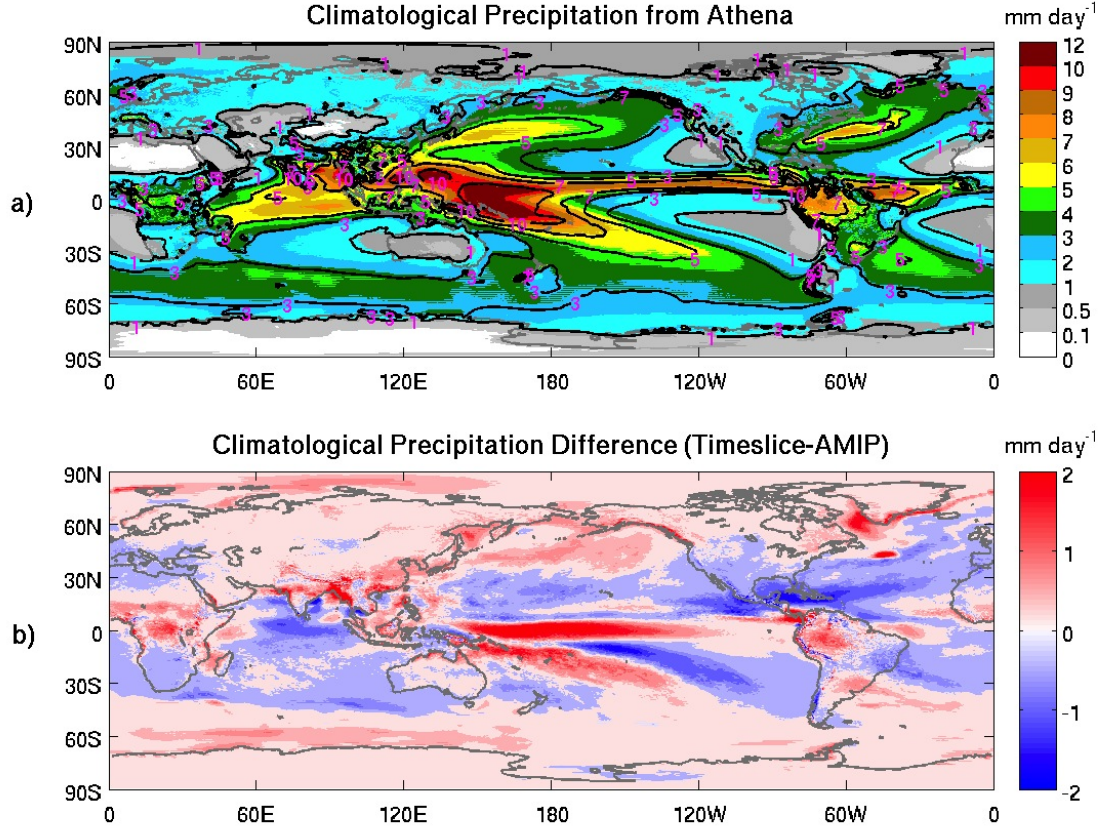


Figure 4.1: Climatological mean rainfall for AMIP (color coded) and TS (contours) (a). Their difference (TS-AMIP) is shown in (b). Units  $\text{mm day}^{-1}$

In the following discussion, we focus on T1279 results and make reference to the T159 where appropriate. The annual mean AMIP and Time-slice (TS) precipitation and their differences are shown in Fig. 4.1a. Changes under GHG warming are shown in their difference map. In the tropics, the change is characterized by a zonal tripole over the ITCZ and SPCZ region, with positive changes between a zone in the central tropical Pacific between  $140^{\circ}\text{E}$  and  $120^{\circ}\text{W}$ , negative changes in a zone from  $120^{\circ}\text{W}$  to  $30^{\circ}\text{W}$  and  $10^{\circ}$ - $30^{\circ}\text{N}$ , and another region of positive change orienting NW-SE in the South Pacific. Oceanic precipitation generally decreases, but increases poleward off the tropical belts. Over land, precipitation increases near the equator for both South America and Africa. Other areas of major land precipitation increases are seen over the coastal region of Burma and in the

southern tip of Central America. Outside the tropics, precipitation generally increases.

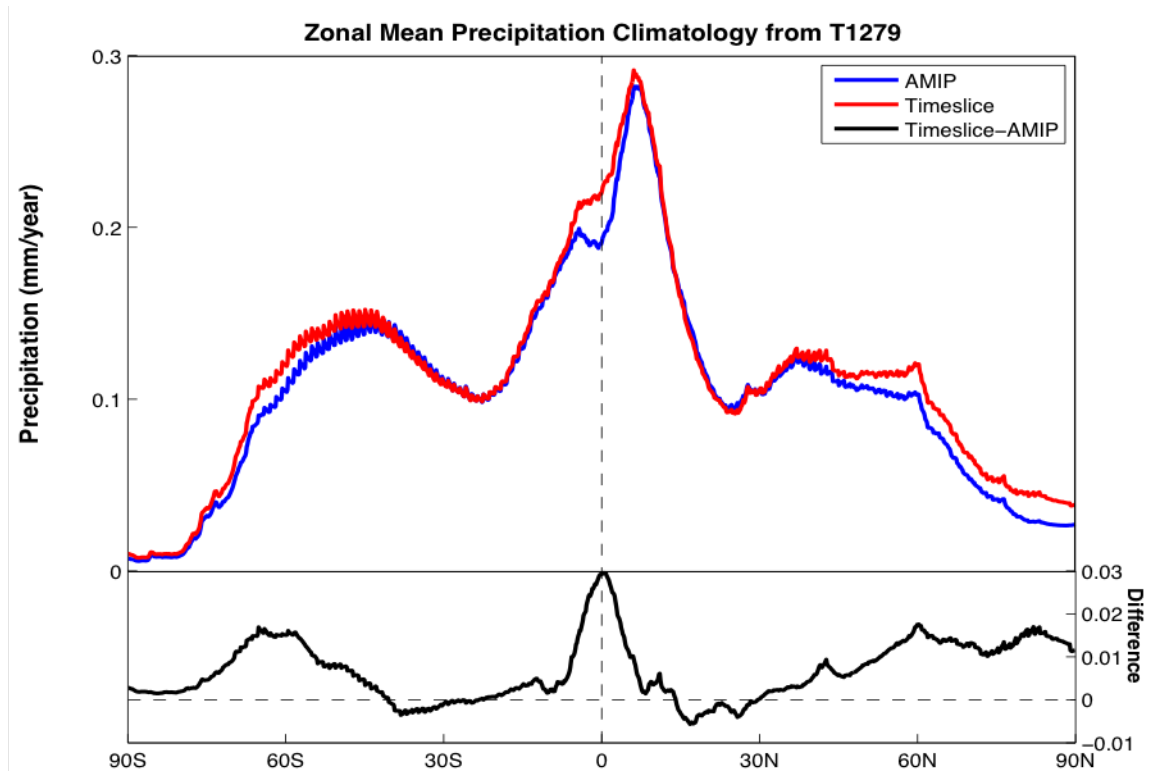


Figure 4.2: Latitudinal distribution of zonal mean rainfall ( $\text{mm hr}^{-1}$ ) for AMIP (blue) and TS (red) and their difference (in black)

Fig. 4.2 (top) shows the latitudinal distribution of zonal mean precipitation from AMIP, TS, and their difference (TS minus AMIP, lower panel). Maximum AMIP zonal rainfall occurs slightly off the equator in the Northern Hemisphere with a relative minimum right at the equator. It shows another relative minimum at the subtropics, increasing to a relative maximum in the mid-latitudes, before tapering to their absolute minimum at the poles for both hemispheres. In the TS simulation, the zonal profile is similar except the equatorial minimum disappears. The subtropical minimum also shifts slightly poleward, resulting in a maximum slightly off the equator in the Southern Hemisphere for the difference (TS-AMIP). The hemispheric asymmetry is also evident as the difference shows a peak slightly off the equator in the Southern Hemisphere.

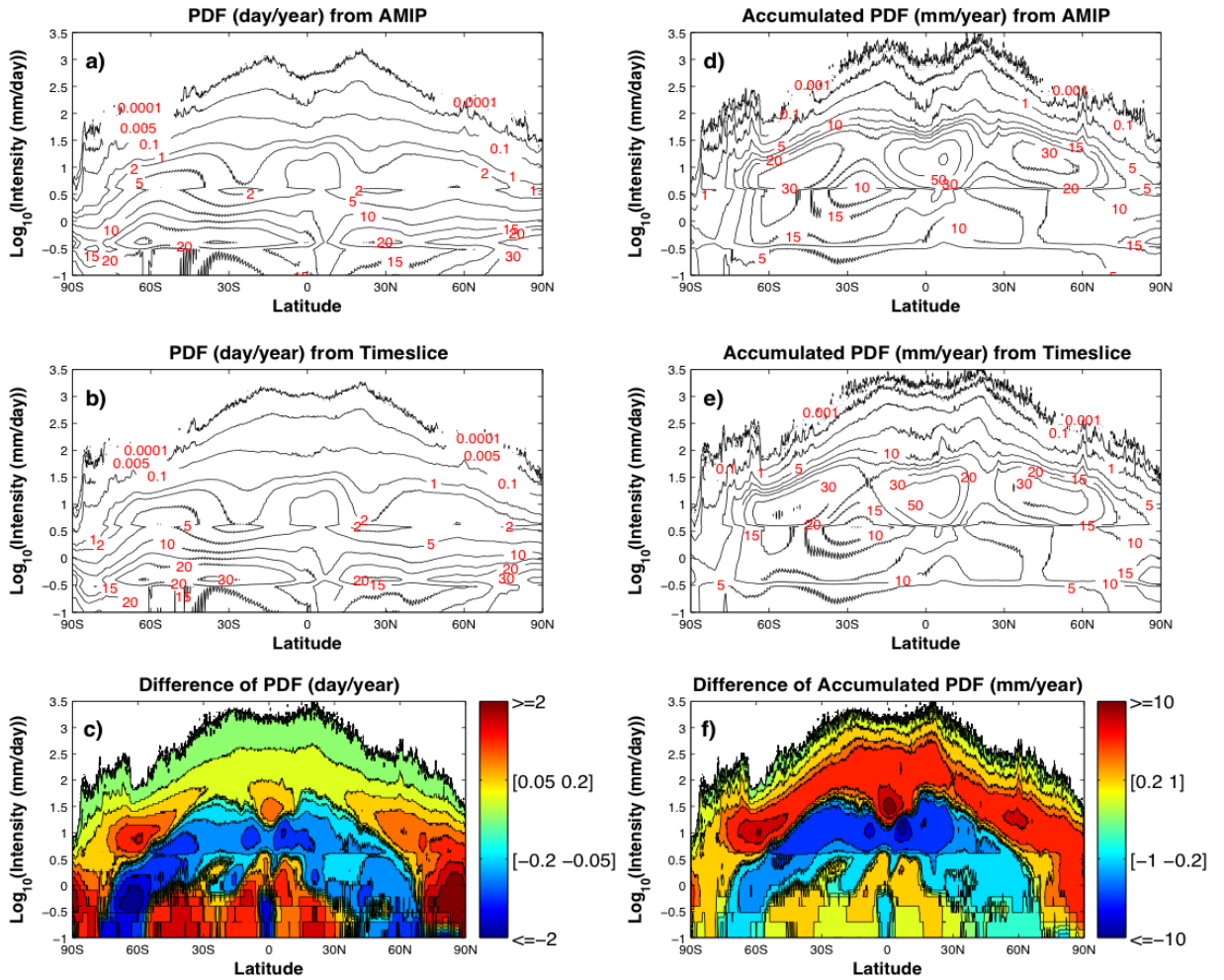


Figure 4.3: Precipitation frequency distribution with intensity in each latitude from AMIP displayed in panel (a), time-slice in panel (b), and time-slice minus AMIP in panel (c). The corresponding frequency accumulation from AMIP demonstrated in panel (d), time-slice in panel (e) and their difference in panel (f)

The above discusses the changes in precipitation amount. However, it does not tell us how precipitation frequency and intensity will change. Changes of frequency and intensity are also crucial to assessing the global warming impacts (Trenberth et al., 2003). To further understand the detailed changes of zonal mean precipitation under the warming scenario, the intensity spectrum of precipitation frequency and accumulation, and their change patterns in different latitudes are analyzed in Fig. 4.3, based on AMIP and time-slice simulations. The intensity bins are the same in all latitudes. For a given latitude, precipitation

frequency in each intensity bin is the number of days whose precipitation rate is within the corresponding intensity interval, normalized by the number of years simulated in the model. Similarly, precipitation amount in each intensity bin is the annual accumulation of precipitation within the corresponding intensity interval. The vertical summation in Fig. 4.3a, b is 365 days, and in Fig. 4.3d, e it adds up to the total annual mean precipitation amount in that latitude. Contour centers in Fig. 4.3a, b indicate that precipitation often occurs with light and very light rates below 1 mm/day when it is precipitating. However, the moderate precipitation rate between 1-30 mm day<sup>-1</sup> contributes most of total precipitation, especially in the tropics and mid-high latitudes shown by the contour center in Figs. 4.3d, e. The contribution of heavy precipitation rate above 30 mm day<sup>-1</sup> peaks around 15 and then decreases with latitude. Figs. 4.3c, f show that intensity spectra changes of frequency and accumulation precipitation look to be similar, and they vary with latitude. In general, between 40°N and 60°S except at the equator, the precipitation intensity distribution tends to become flat with very light (< 1mm day<sup>-1</sup>) and heavy precipitation (> 30 mm day<sup>-1</sup>) increasing but moderate rain decreasing, while in latitudinal bands of 40°N-70°N and 60°S-80°S, precipitation tends to be shifted to heavier with light precipitation (<3 mm day<sup>-1</sup>) decreasing but moderate and heavy increasing. At high latitudes poleward of 70°, precipitation of all intensities increases. We notice an asymmetric intensity spectrum change over mid-high latitude (40°-60°) in both hemispheres, i.e., very light precipitation increases in SH while it decreases in NH. In addition, the narrow equatorial belt stands out with a significant decrease of very light rainfall and greater increase of heavy rainfall than other low latitude belts.

Based on the discussion of zonal mean precipitation change in amount and intensity spectra, we may conclude that the large amount of precipitation increase over the tropics (Fig. 4.2) is mostly contributed by increases in heavier precipitation frequency and intensity. Though the days of light precipitation increase (Fig. 4.3c), their contribution to the increase of total precipitation is relatively small (Fig. 4.3f). This is consistent with the studies' suggestions that the enhanced circulation of the moisture convergence leads

to higher precipitation rates (Trenberth, 1999; Trenberth et al., 2003). The decreases of subtropical precipitation (Figs. 4.1b, 4.2) are mostly caused by the reduction of moderate rain ( $1-30 \text{ mm day}^{-1}$ , Figs. 4.3c, f). Heavy precipitation ( $>30 \text{ mm day}^{-1}$ ) frequency significantly increases over all latitudes. This has been revealed by several observational analyses and simulations (Emori and Brown, 2005; Held and Soden, 2006; Houghton et al., 2001; Zhang et al., 2007). It suggests that heavy precipitation will happen more in the future if the global warming trend continues. This overall change of the zonal mean precipitation is supported by 15 CMIP5 models and proves to be robust (not shown).

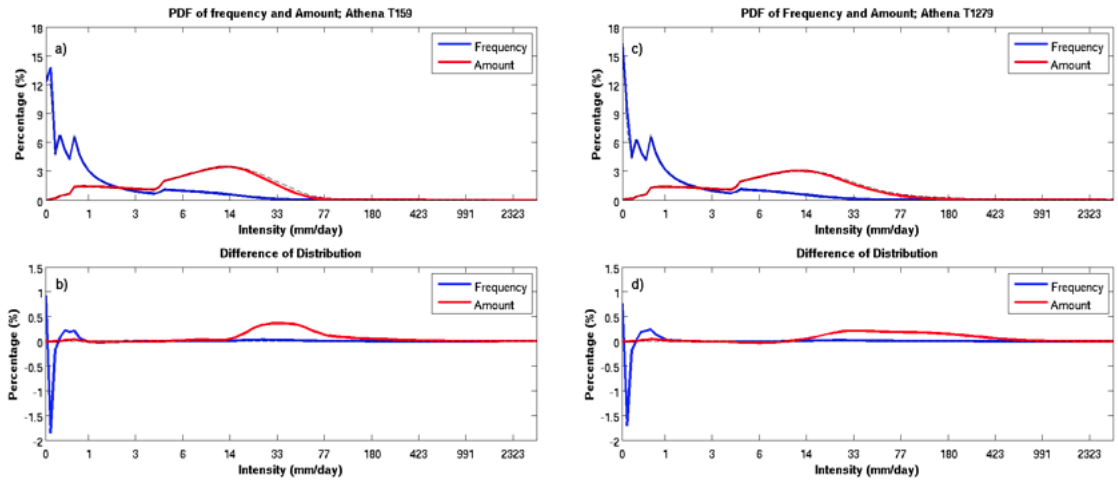


Figure 4.4: Probability distribution of rain frequency and rainfall distribution of AMIP and TS simulation from T159 and T1279 (upper). The lower panels show their difference.

Fig. 4.4 shows the rain frequency (PDF) and distribution (CPDF) for AMIP and TS (upper panel, (a) and their difference (lower panel, (b)). From their difference, we identify four rain categories and label them as drizzle ( $0-0.1 \text{ mm day}^{-1}$ ), light ( $0.1-1.2 \text{ mm day}^{-1}$ ), moderate moderate ( $1.2-15 \text{ mm day}^{-1}$ ) and heavy rain ( $>15 \text{ mm day}^{-1}$ ).

Table 4.1: Average rain rate (intensity) for each rain category at T159 and T1279 resolution for AMIP and TS simulations

Category	Drizzle ( $0-0.1 \text{ mm day}^{-1}$ )		Light ( $0.1-1.2 \text{ mm day}^{-1}$ )		Moderate ( $1.2-15 \text{ mm day}^{-1}$ )		Heavy ( $>15 \text{ mm day}^{-1}$ )		Total	
	T159	T1279	T159	T1279	T159	T1279	T159	T1279	T159	T1279
AMIP ( $\text{mm day}^{-1}$ )	$4.7 \times 10^{-3}$	$4.15 \times 10^{-3}$	$1.67 \times 10^{-1}$	$1.71 \times 10^{-1}$	1.71	1.75	1.03	1.22	2.91	3.14
Timeslice ( $\text{mm day}^{-1}$ )	$4.72 \times 10^{-3}$	$4.13 \times 10^{-3}$	$1.67 \times 10^{-1}$	$1.73 \times 10^{-1}$	1.66	1.68	1.22	1.42	3.05	3.28
Sensitivity ( $\% \text{ K}^{-1}$ )	0.2	-0.2	0	0.4	-1.2	-1.5	6.8	6.3	1.8	1.7

Table 4.2: Frequency of each rain category at T159 and T1279 for AMIP and TS simulations. Each row sums to 365.2 day

Category	Drizzle (0-0.1 mm day <sup>-1</sup> )		Light (0.1-1.2 mm day <sup>-1</sup> )		Moderate (1.2-15 mm day <sup>-1</sup> )		Heavy (>15 mm day <sup>-1</sup> )		Non-rain	
	T159	T1279	T159	T1279	T159	T1279	T159	T1279	T159	T1279
AMIP (mm day <sup>-1</sup> )	55.2	40.5	117.9	117.0	128.9	136.4	15.7	16.2	47.5	55.2
Timeslice (mm day <sup>-1</sup> )	52.4	37.7	119.7	118.9	125.0	132.0	17.3	17.2	50.9	59.4
Sensitivity (% K <sup>-1</sup> )	-2.0	-2.7	0.6	0.6	-1.2	-1.3	3.7	2.5	2.8	2.9

Tables 4.2 and 4.1 summarize the rain frequency and distribution for both the T159 and T1279 resolutions for the AMIP and TS simulation. For rain frequency, the sum of the rows of Table 4.2 is 365.2 days, which is the time period for one year. For rain contribution, the sum of the rows of Table 4.1, corresponding to drizzle, light rain, moderate and heavy rain sums to the global average. For the AMIP simulation, the frequency of dry, moderate, and heavy rain days increases, while the frequency of drizzle and light rain days decreases, and increases in moderate and heavy rain as the resolution is increased from T159 to T1279 (Table 4.2). This pattern is similar for the TS simulation, except for a minor decrease in the heavy rain for T1279.

We defined a sensitivity of rainfall parameter as follows:

$$S = \frac{r_2 - r_1}{r_1 \cdot \Delta T} \quad (4.1)$$

Where the  $r$  is the parameter, and subscript  $r_2$  and  $r_1$  indicate parameters for TS and AMIP simulations respectively, and  $\Delta T$  is the change in surface temperature, as prescribed in the experiment. The unit of  $s$  is %K<sup>-1</sup>.

We compute the sensitivity for the rain frequency for both T159 and T1279. All rain categories show comparable sensitivities of the same sign, except for the drizzle. The response of the heavy rain is much smaller for the high resolution T1279 than the coarse resolution T159. The number of non-rain (dry) days increases from 47.2 to 55.2 for T159 and T1279, respectively, indicating fewer rainy days (8 days) at the higher resolution. This decrease in rain days due to resolution is dominated by a decrease in the drizzle while the

other rain categories increase for AMIP. Under TS, the number of dry days increases by 3.4 and 4.2 days for T159 and T1279. The number of heavy rain days and light days increases as the number of moderate rain and drizzle days decreases.

The average rainfall amount for each rain category is shown in 4.1. Rainfall increases for all categories except for the drizzle as resolution increases from T159 to T1279. All rain categories show increases under a warming scenario, except for the drizzle. The sensitivity of the global rainfall of 1.8 and 1.7%  $K^{-1}$  is comparable to that estimated for the global hydrologic cycle of 1-2%  $K^{-1}$ . The most sensitive change is associated with heavy rain, with 6.8%  $K^{-1}$  for T159 and 6.3%  $K^{-1}$  for T1279. They approach the limit of the CC relation of the response of 7%  $K^{-1}$  for columnar water vapor under constant relative humidity (O’Gorman and Muller, 2010).

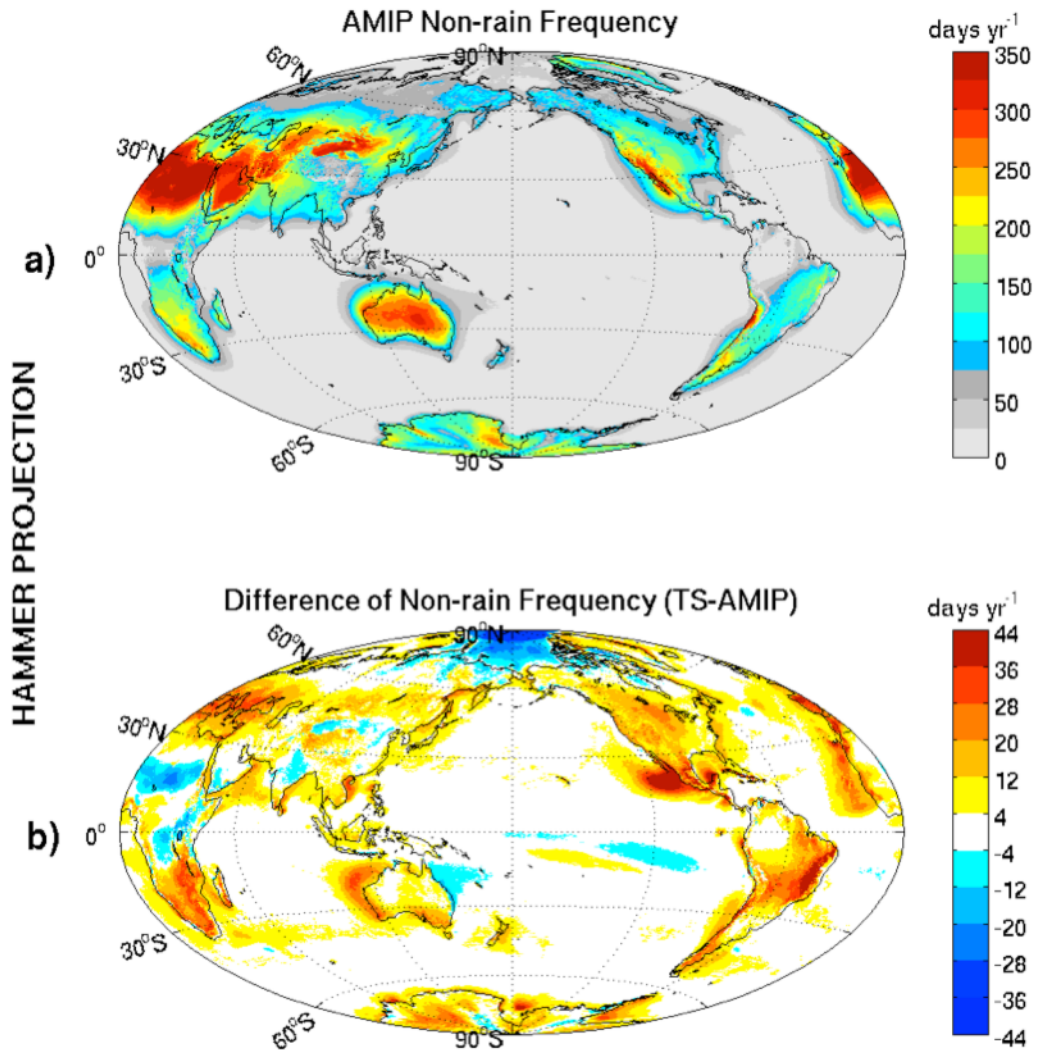


Figure 4.5: Frequency distribution for non-rain days for AMIP, TS and their difference (TS-AMIP) in day year<sup>-1</sup>

Figure 4.5 shows the number of non-rain days for AMIP (top) and the change under global warming (TS-AMIP). The number of dry-days shows maxima in desert zones such as the Africa Sahara Desert, Great Arabia Desert, Thar, Turkistan, and Takla-Makan-Gobi Desert over Africa and Eurasia and the North American Desert over north America. In the Southern Hemisphere, the maximum is located in the Australian and Kalahari and Nimbi Desert in the southern tip of Africa. The number of dry days increases over most of the

land areas in both North and South America. Over the African Sahara, the change suggests a shift of the dry zone, which migrates northwards, showing fewer dry days in the southern edge of the Sahara while the increase in number of dry days extends to the northern coastal region of Africa. There is also a significant increase of dry days the Kalahari Desert in the southwestern tip of Africa.

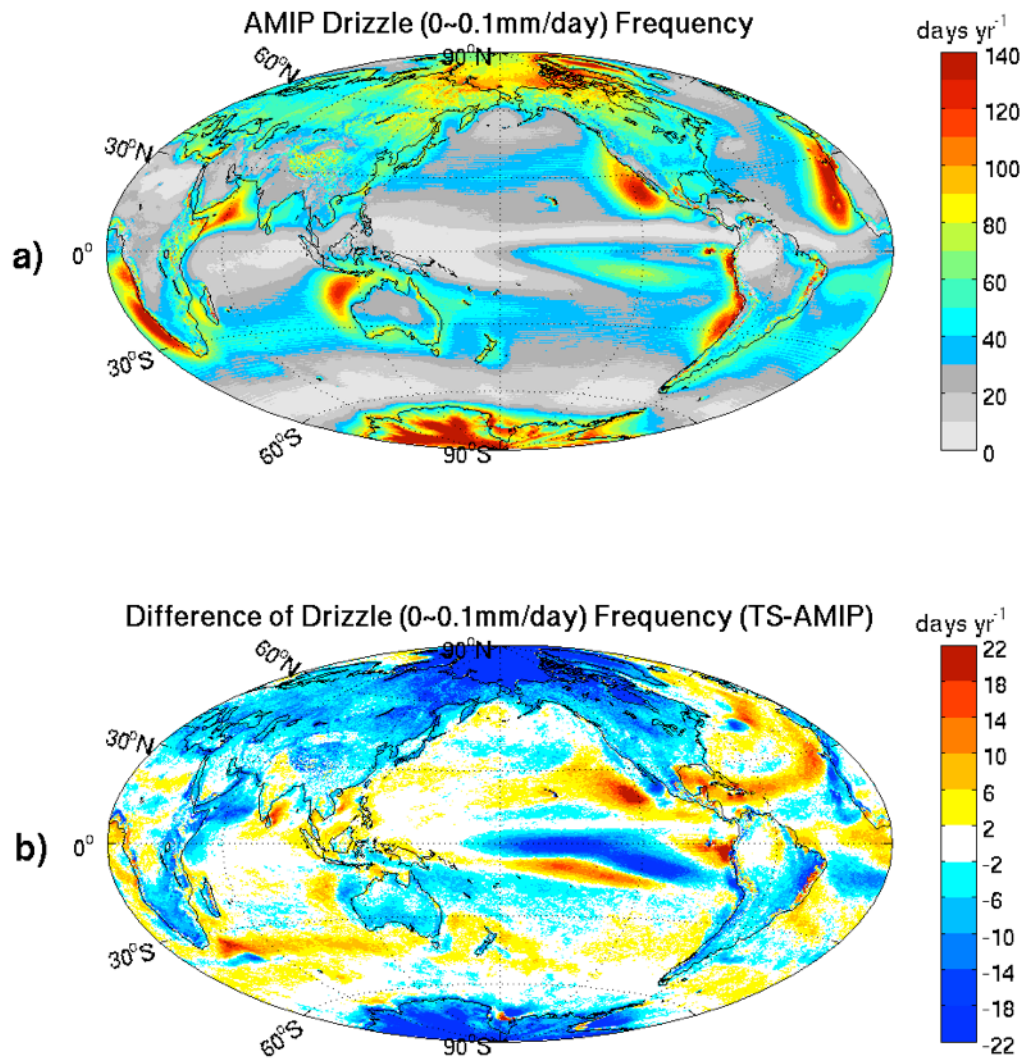


Figure 4.6: Same as 4.5, except for drizzle with rain rate ( $0-0.1 \text{ mm day}^{-1}$ )

Maxima of the drizzle frequency (Fig. 4.6) are concentrated in a few coastal regions,

such as the Arabian Sea, the west coast off the North American Desert, the northwest coast of northern Africa and Australia, the west coast of southern Africa and South America, and the coastal region of the Arctic Ocean. Under GHG warming (TS), there are large reductions of drizzle in the Arctic and over Antarctica, and on most of the land areas. The band of drizzle increase at around 30°S suggests an expansion or migration of the drizzle over the “roaring forties” or the circumpolar front. Other oceanic areas of decrease seem to be associated with the deserts, suggesting further inhibition of drizzle formation on the desert outflow area. There is significant decrease in the ITCZ region. In meteorological operations, drizzle impairs visibility but is difficult to quantify as its drop size falls outside the range of most conventional (tipping bucket gauge) and remote sensors. Drizzle is mostly associated with stratus clouds where the small drops do not have sufficient time to grow before falling back to the surface. However, this small but continuous evaporation/condensation process may contribute to the global water cycle. The decrease in drizzle has been documented in a number of observational studies (Lau and Chiu, 2010).

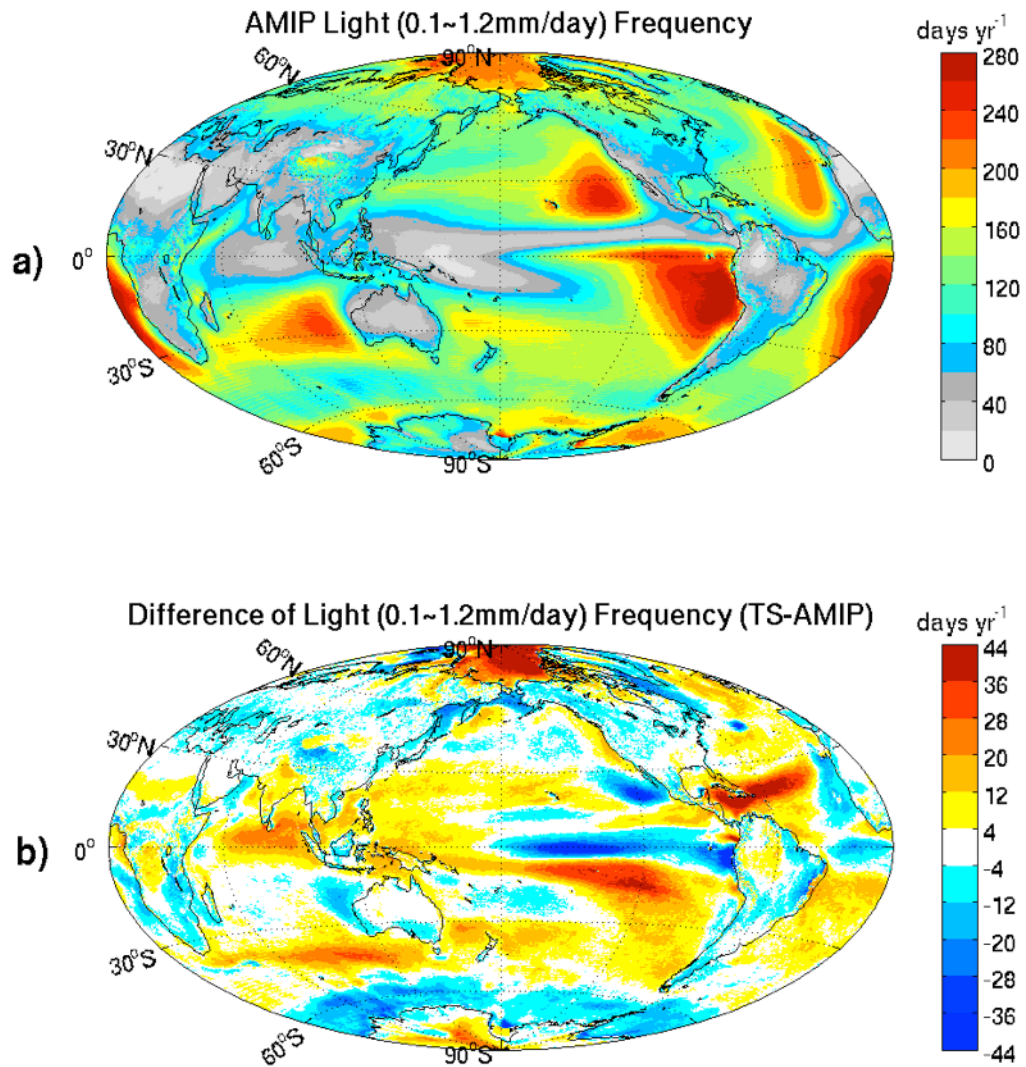


Figure 4.7: Same as 4.5, except for light rain with rain rate (0.1-1.2 mm day<sup>-1</sup>)

Regions of light rain are concentrated over the oceanic dry regions, over subtropical highs and over the Arctic (Fig. 4.7). Their change due to GHG warming is slightly different from that of drizzle, as there is an increase in light rain in the Arctic, and to a lesser extent in Antarctica. In the eastern equatorial Pacific, the north-south dipole may result from a shifting of the rain types associated with the ITCZ. The negative center of the dipole in fact corresponds to the light rain reduction over the equator in the spectrum change pattern (Figs. 4.3c, f). The decrease of light rain in the coastal zone of the Antarctic and

a southward movement of the northern boundary of the circumpolar front may suggest a weakening of precipitation in the circumpolar front.

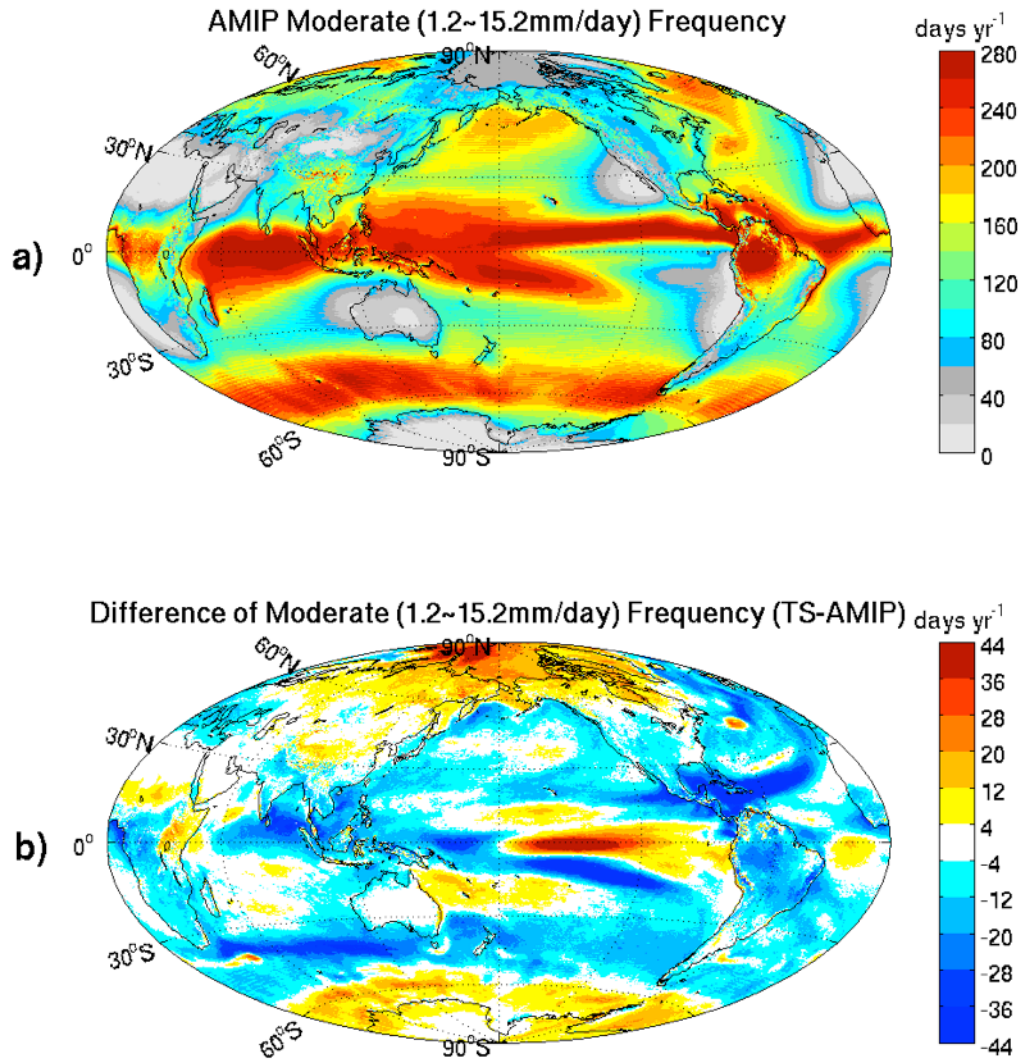


Figure 4.8: Same as 4.5, except for moderate rain with rain rate (1.2-15 mm day<sup>-1</sup>)

The moderate rain (Fig. 4.8) contains about 33% of the frequency count while contributing to 56% of the global rainfall. Strong zonal bands of moderate rain are concentrated in the equatorial Pacific and Indian Ocean, with extension to the SPCZ. There are also

high occurrences in the storm tracks off the continental coastal region and in the Antarctic circumpolar front region. The response to GHG warming is characterized by increases in moderate rain in the Arctic, decreases in the maritime continent, a dipole structure in the eastern equatorial Pacific, decrease at the extra tropics at  $30^\circ$  south and an increase near the coastal Antarctica. Generally speaking, the precipitation decreases from tropics to mid-latitudes, but increases in high latitudes. These features are also reflected on the spectrum change pattern (Figs. 4.3c, f). Some of the change patterns are opposite to those observed at the light rain.

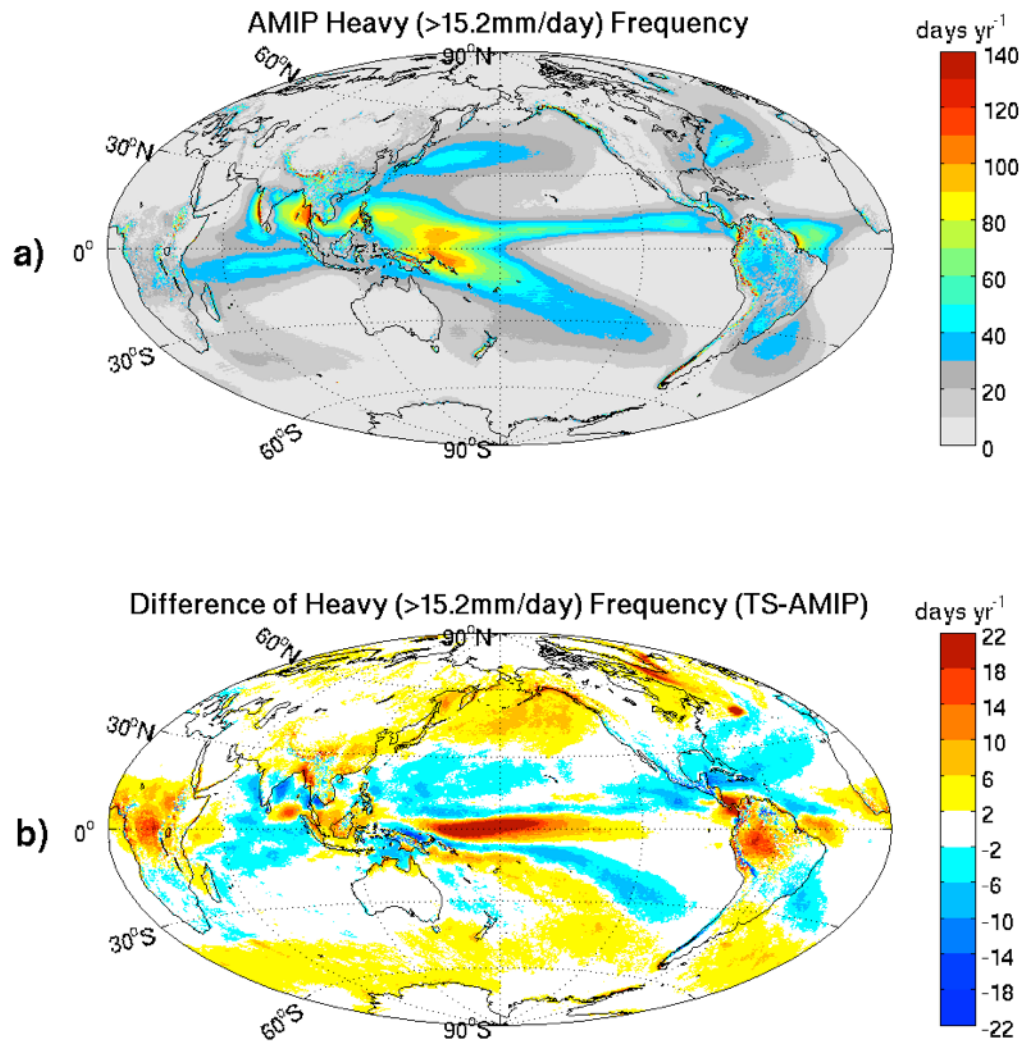


Figure 4.9: Same as 4.5, except for heavy rain with rain rate ( $>15 \text{ mm day}^{-1}$ )

The heavy rain (Fig. 4.9) accounts for only 4.5% of the frequency, but for almost 39% of the total rainfall. They are concentrated in the tropical rain belts such as the ITCZ, SPCZ, the South American Convergence Zone, the major storm track regions in the Pacific and Atlantic, in the Bay of Bengal, over SE Asia, equatorial Africa, and Amazonia. In a warming scenario, there is higher frequency of heavy rain over the heavy rain regions over land, including the equatorial regions of Africa and Amazonia, accompanied by slight increase over the eastern part of China. However, there is a narrow region of decrease in the

coastal region of western North America. Over the oceans, the change is characterized by a negative-positive-negative band, with the positive pattern centering over the equatorial western Pacific. There are slight increases in heavy precipitation over the circumpolar frontal zones.

### 4.3.2 Change of precipitation rates in different climatological regions

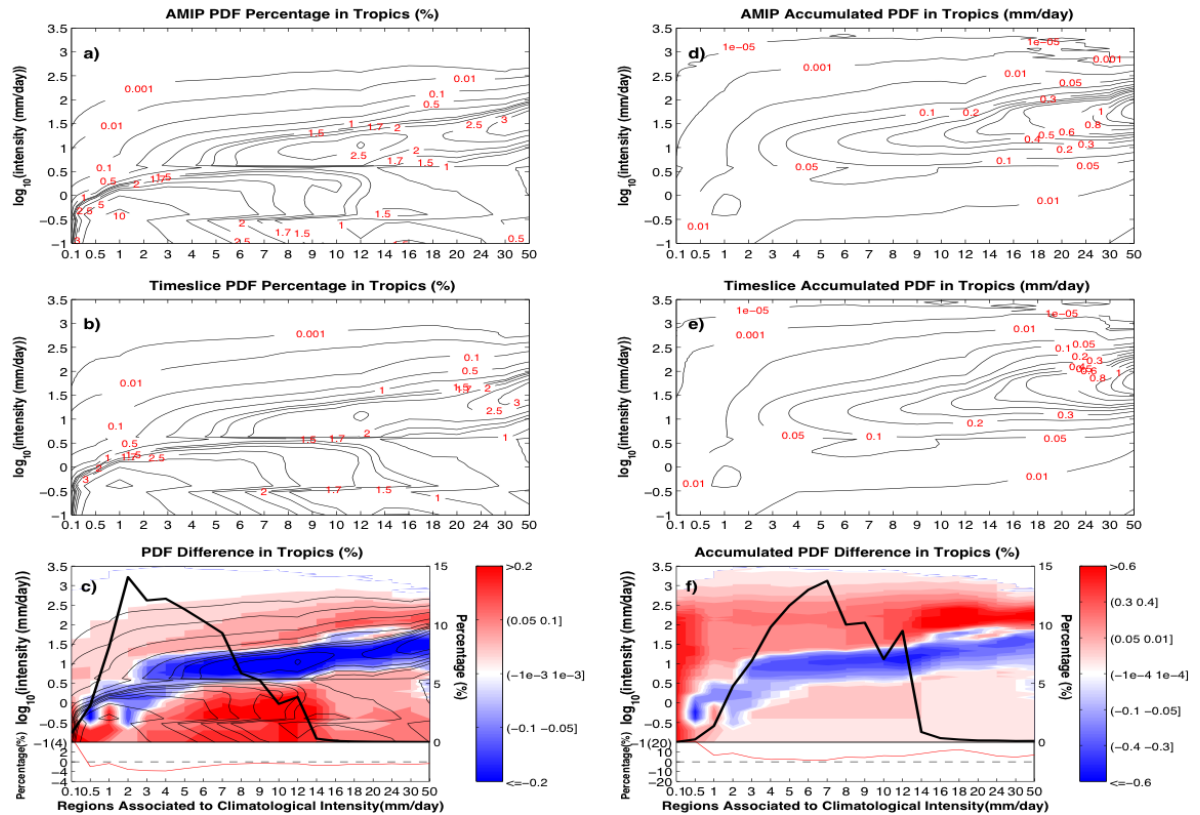


Figure 4.10: Frequency of precipitation distribution with intensity in different AMIP climatology regions for AMIP run (a), time-slice (b), and time-slice minus AMIP (c) (shading). The corresponding accumulated distribution of precipitation from different intensity over each AMIP climatological regimes are in (d)-(f). Population percentage is overlaid in panel (c). The fraction of rainfall panel f) denoted by black lines, as well as the PDF and accumulated PDF difference superimposed in corresponding panels by red lines, respectively).

Precipitation variation on latitudinal distribution shows some important changing characteristics under a warming scenario. However global warming effects on precipitation are evidently dependent on regions and seasons. The precipitation systems are significantly

different between convective storms in the tropics and baroclinic systems in the high latitudes. We explore these characteristics in different latitudinal belts, including the tropics ( $20^{\circ}\text{S}\sim 20^{\circ}\text{N}$ ), subtropics ( $20^{\circ}\sim 40^{\circ}$ ), and mid-high latitudes ( $40^{\circ}\sim 70^{\circ}$ ) as discussed above. In each belt, the areas with climatological precipitation falling into the corresponding bin are categorized into one climatological region. The number of climatology bins is 21. It is structured as 0, 0.1, 0.5, 1, 2, 3, 4, 5, 6, 7, 8, 9, 10, 12, 14, 16, 18, 20, 24, 30 and  $50\text{ mm day}^{-1}$ .

Firstly, we focus on the tropics. The intensity distribution of daily precipitation in different climatology regions is compared from the current (AMIP) to the future (time-slice) in 47-year simulations shown in Fig. 4.10. The left panels show the intensity spectra of frequency and the right panels display the intensity spectra of accumulated precipitation. Black lines in Figs. 4.10c and 4.10f respectively denote the contribution of frequency and amount to the total precipitation frequency and total precipitation amount from each climatological region. The red line represents its change with climate warming. The black line in Fig. 4.10f shows that in the tropics, the precipitation contribution is from regions with a broad range of precipitation climatology from 0 to  $14\text{ mm day}^{-1}$  with the peak in the regions with mean precipitation around  $7\text{ mm day}^{-1}$ . Negative values of the red line in Fig. 4.10c indicate that precipitation becomes less frequent, but precipitation amount increases in all climatological regions (Fig. 4.10f), and thus the average precipitation intensity becomes heavier overall under a warm climate. In the main precipitation regions with precipitation climatology from 0 to  $14\text{ mm day}^{-1}$ , the prevailing frequency events (large contour values in Fig. 4.10c) become less frequent but lighter intensity events and heavier events than the prevailing frequency tend to be more frequent. The frequency distribution with intensity tends to be flat in shape. Interestingly, the reduced frequency just overlaps the spectrum peak of precipitation frequency (Fig. 4.10c). Moreover, the precipitation intensities corresponding to the peak frequency (contour center) vary in different regions. The rainier the climatological region is, the heavier the prevailing precipitation systems are. In fact, the intensity corresponding to the frequency peak increases roughly linearly with

the precipitation climatology when we plot the figure with equal intervals for both axes (not shown). Thus, it is not reasonable to simply categorize the intensity of precipitation into light, moderate, and heavy by several constant precipitation intervals. The criterion should depend on the climatology regions.

In this part, we classify the precipitation events according to climatology-region-dependent criteria. The events within the scope of prevailing precipitation are considered to be moderate rain. Higher intensity events are grouped into heavy rain, and lower intensity events into light rain. On the other hand, the total precipitating day decrease in these wet climate regions is mainly caused by a reduction of the relatively moderate rain events (Fig. 4.10c), while the total precipitation amount tends to increase resulting from heavy rain increases (Fig. 4.10f). In very dry regions with climatological daily precipitation less than  $0.1 \text{ mm day}^{-1}$ , all intensities of precipitation events are more frequent and total precipitation increases. These regions are mostly in the Sahel region of Africa, stretches from the Atlantic coast of Mauritania and Senegal through to Sudan, and Eritrea and the Red Sea.

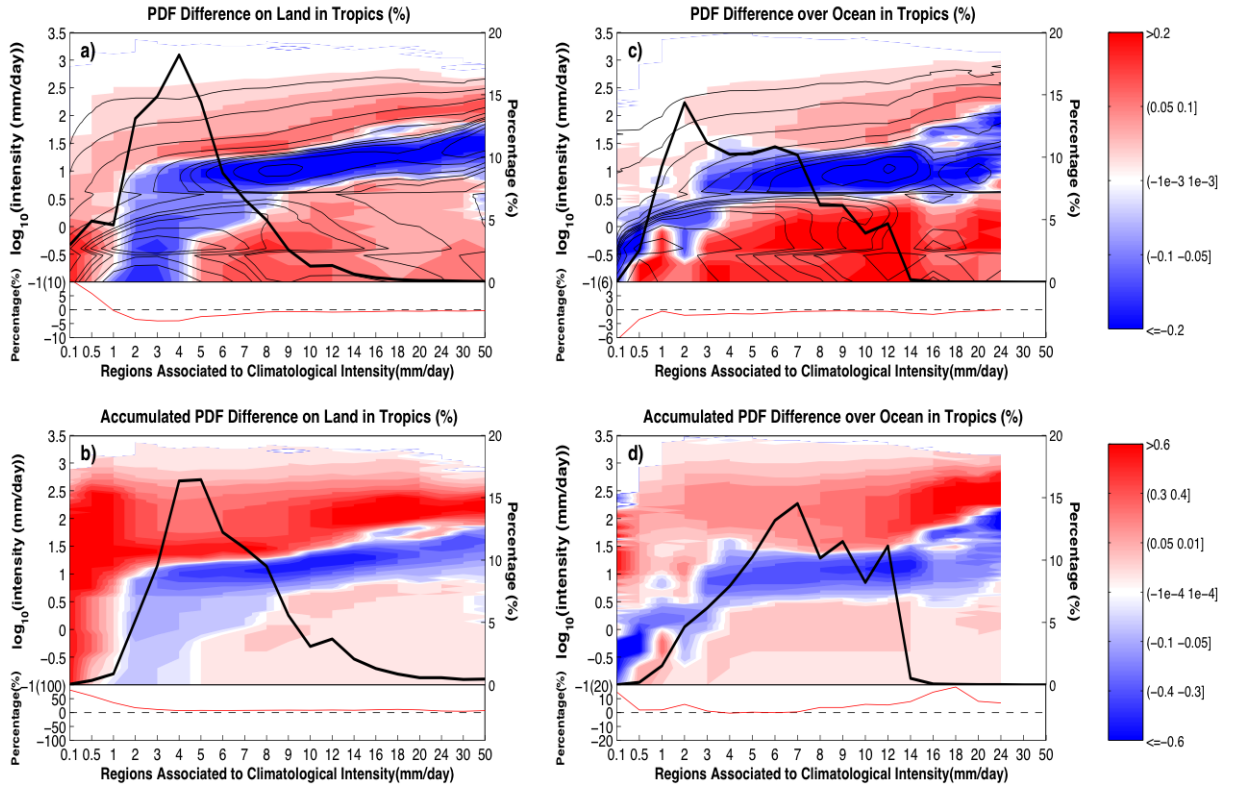


Figure 4.11: Tropical intensity dependent PDF difference on land in different climatology regions shown in panel (a), accumulated PDF difference on land in panel (b), while the PDF difference over ocean is displayed in panel (c). Accumulated PDF difference over ocean in panel (d). The format of panel (a) and panel (c) are the same as that of Fig. 10c, and the format of panel (b) and panel (d) the same as the one of Fig. 4.10f

Since the tropical ocean and land have different mechanisms to generate precipitation, a similar analysis is separately made for each (Fig. 4.11). The precipitation PDF, with climatology regions (black lines) indicating precipitation amount over the ocean (Fig. 4.11d), has broader spread than on land (Fig. 4.11b). Both frequency (Fig. 4.11a) and amount (Fig. 4.11b) over tropical land peaks at around  $4\text{-}5 \text{ mm day}^{-1}$  regions, while the tropical ocean shows the peak for frequency (Fig. 4.11c) is  $2 \text{ mm day}^{-1}$  regions, and  $7 \text{ mm day}^{-1}$  regions for amount (Fig. 4.11d). As for the spectra change patterns (shaded), all regions in the tropical ocean show a positive tendency for heavy and light precipitation, and negative tendency for moderate rain. Again, this moderate frequency reduction follows the peak of frequency (not shown) causing the precipitation frequency decrease. Over tropical land,

in regions with mean daily precipitation  $< 1 \text{ mm day}^{-1}$  such as arid regions in Africa, all intensities of precipitation events increase, and thus total precipitation amount increases. In wet tropical land, total precipitation amount slightly increases but frequency decreases, and distribution of events becomes flat with an increase in light and heavy rain but a reduction in moderate rain in both frequency and amount. Between the dry and rainy regions ( $1\text{-}5 \text{ mm day}^{-1}$ ), the spectra demonstrate a higher intensity switch tendency, i.e. heavy precipitation increases at the expense of moderate and light precipitation reduction. In addition, heavy precipitation increase is larger over tropical land than the tropical ocean.

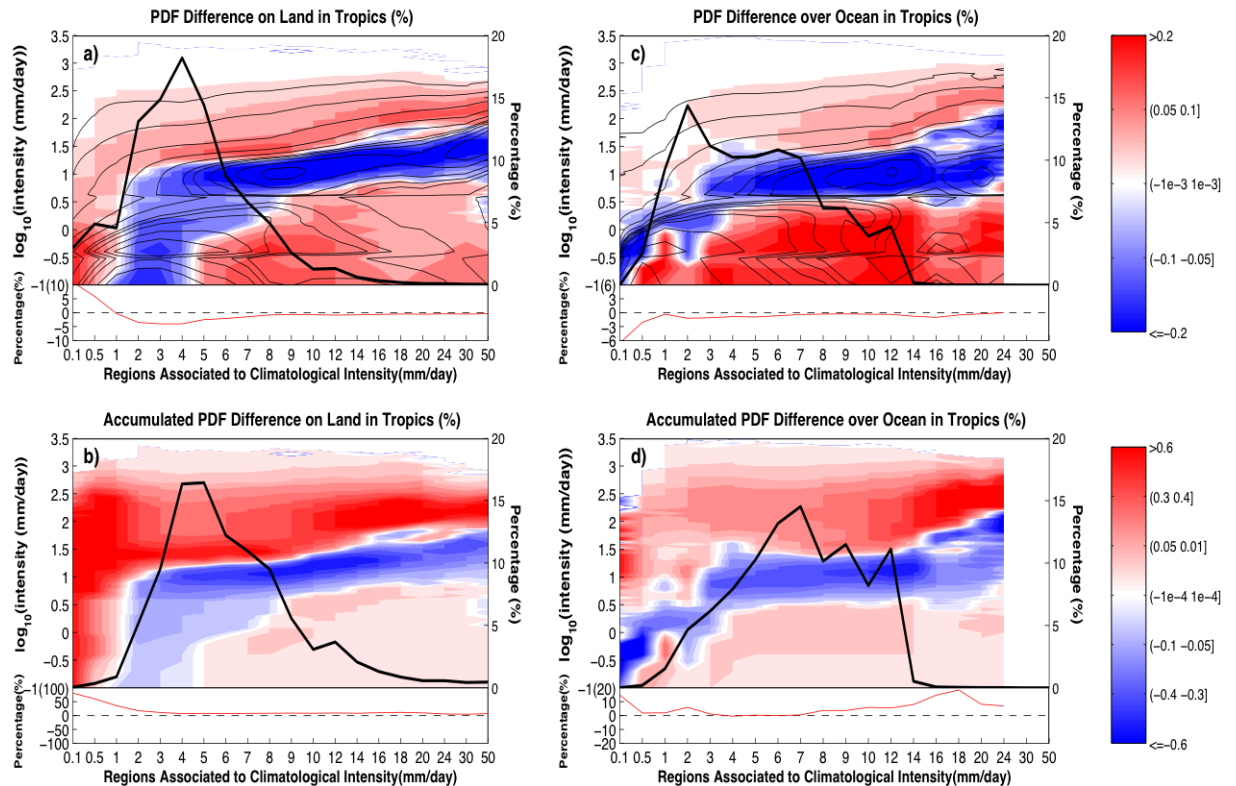


Figure 4.12: Subtropical intensity dependent accumulated PDF on land in summer shown in panel (a), on land in winter in panel (b), over ocean in summer in panel (c) and over ocean in winter in panel (d). The format of all these panels is the same as Fig. 4.10f.

In extratropical regions, precipitation has strong seasonal characteristics. Thus, the intensity spectra of subtropical precipitation changes in different climatological regions are analyzed in both summer and winter. In this section, only accumulated precipitation change

patterns are illustrated in Fig. 4.7, including four panels, which are for land summer (Fig. 4.12a), land winter (Fig. 4.12b), ocean summer (Fig. 4.12c) and ocean winter (Fig. 4.12d) in that order. The summer season is defined in the Northern Hemisphere as June-August (JJA) and in the Southern Hemisphere as December-February (DJF), while the winter season is the opposite. Except in the very dry climatology regions ( $< 0.1 \text{ mm day}^{-1}$ ), summer precipitation over subtropical land exhibits slightly positive/no tendency of light precipitation, positive tendency of heavy precipitation, but large negative tendency of moderate precipitation. It results in the decrease of total precipitation amount in all climatological precipitation regions. The difference between subtropical winter and summer spectra change patterns lies in the light precipitation. Winter land shows a light precipitation reduction, while summer land displays slight enhancement of light precipitation. On the other hand, both ocean panels illustrate a flatter redistribution of precipitation accumulation. We also notice a consistent increase of summer rainfall with all intensities in the very dry regions at precipitation climatology less than  $0.1 \text{ mm day}^{-1}$ , corresponding to the Sahelian region. Winter desert precipitation tends to decrease, while there is an increase in the narrow semi-arid region. Desert rainfall change patterns still need to be confirmed by more experiments.

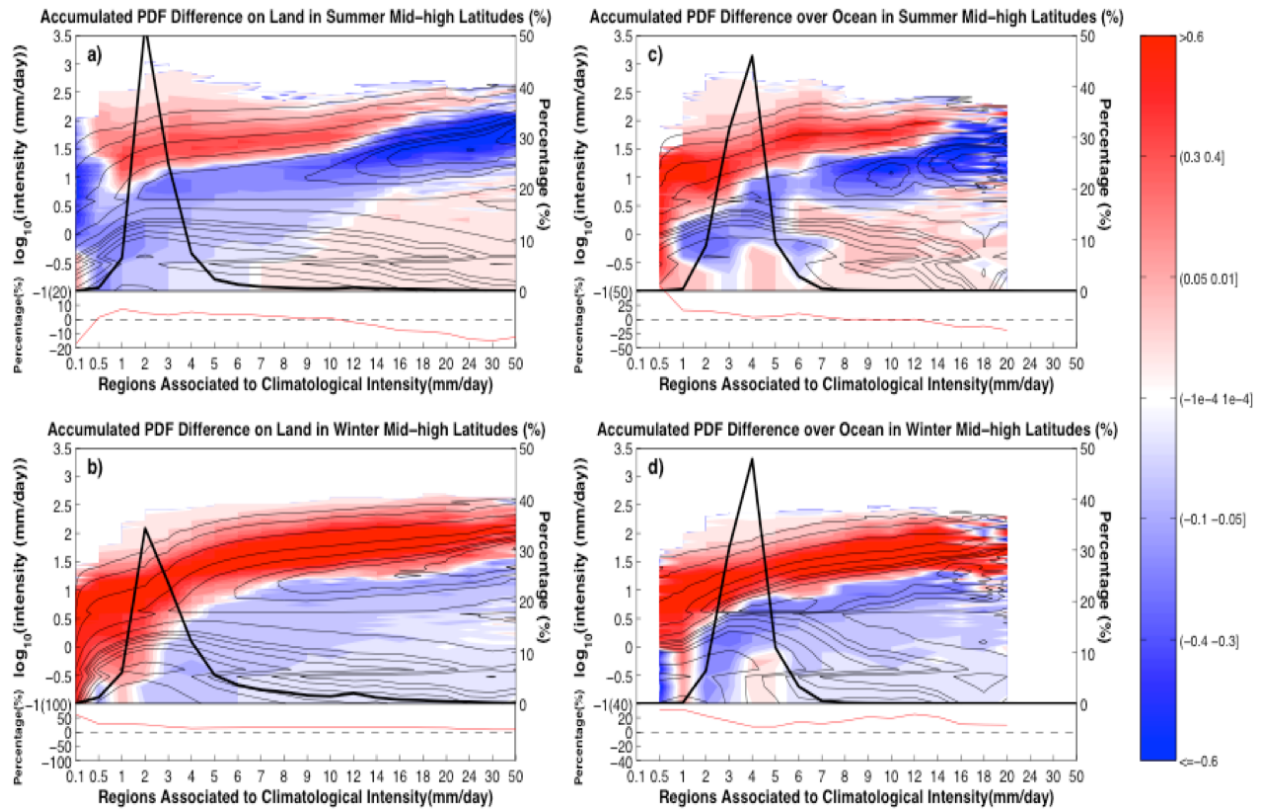


Figure 4.13: Same as Fig. 4.12. except for mid-high latitudes.

Similar to Fig. 4.12, Fig. 4.13 demonstrates the spectra of precipitation accumulation over mid-high latitudes for the land and ocean, for both summer and winter. In the mid-high latitudes, the dominant rain regions cluster around the climatology precipitation of  $2 \text{ mm day}^{-1}$  on land and  $4 \text{ mm day}^{-1}$  over the ocean (black lines). Within these primary rain regions, precipitation changes are different over the ocean and land. Precipitation tends to become heavier with a reduction of light and moderate rainfall and increase of heavy rainfall over land. The precipitation distribution with intensity of the mid-high latitude summer ocean tends to be flatter, and the winter ocean switches to higher intensity. The ocean panels are more disorganized than the land panels. The heavier intensity switch of mid-high latitude land precipitation is larger in winter than summer. Moreover, in rainless regions with precipitation climatology lower than  $0.5 \text{ mm day}^{-1}$ , precipitation increases in the winter but decreases in the summer.

## 4.4 Summary and discussion

We examine the changes in the precipitation associated with GHG warming based on the SRES scenario using two resolution runs of the Athena model, allowing examination of the dependence of rain frequency and distribution of model resolution. Results from two model resolutions of T159 and T1279, corresponding to resolutions of about 128 km to 16 km are examined. From the change in the rain rate PDF we identified four rain types: drizzle (0-0.1 mm day<sup>-1</sup>), light (0.1-1.2 mm day<sup>-1</sup>), moderate (1.2-15mm day<sup>-1</sup>) and heavy (>15mm day<sup>-1</sup>) rain.

Parameters of the rain PDF are dependent on the resolution of observation. The frequency of dry days increases from 13% to 15%, drizzle and light rain frequencies decrease, while moderate and heavy rain frequencies increase when the resolution is increased from T159 to T1279. The increase of non-rain frequency at the high resolution is consistent with a mixed rain rate distribution model consisting of a no rain and a rainy distribution (Kedem et al., 1990). The rain contributions from the drizzle and light rain to the global rainfall are relatively small, accounting for about 47% (43%) of the rain frequency and only about 5.5% (5.5%) of the total global rainfall for T159 (T1279). The moderate and heavy rain contributions increase for both rain categories as the resolution is increased, accounting for 54% and 33% for T159 and 55.7% 38.9% for T1279 for moderate and heavy rain respectively.

Under the SRES scenario of GHG warming, the sensitivity of the various rain categories are computed to be 1.8, 6.8, -1.2, 0, 0.2% K<sup>-1</sup> for T159 and 1.7, 6.3,-1.5, 0.4 and 0; -0.2% K<sup>-1</sup> for T1279 for global rainfall, heavy, moderate, light rain and drizzle. These sensitivities can be compared to those obtain from CMIP5 analysis of 14 models (Lau et al., 2014). While the magnitudes of the numbers are somewhat smaller, the sign of the changes are identical. The global sensitivity of 1.7 and 1.8% K<sup>-1</sup> and the heavy rain sensitivity of 6.8 to 6.3% K<sup>-1</sup> for heavy rain is comparable to the global hydrologic cycle and approaches the CC scaling relation of about 7% K<sup>-1</sup> for columnar water vapor with fixed relative humidity

(O’Gorman and Muller, 2010). In our calculation, the sensitivities for these rain categories are however, slightly less sensitive for the high resolution T1279 than for the low resolution T159. The sensitivity of the moderate rain is negative, being more negative at the high resolution.

Most of the heavy and moderate rain is concentrated in the deep tropics. The decrease in moderate rain accompanied by increases in heavy rain cannot be more evident over the Amazon and at the southern boundary of the Sahara over land and in major rain belts over the ocean (compare Fig. 4.8b and 4.9b). The changes in the deep tropics are characterized by bands of opposite changes in the central equatorial Pacific. These suggest shifts of the ITCZ and SPCZ. The increase in the rainfall contribution in the deep tropics (Fig. 4.1b) can be attributed to the expansion of the warm pool rainfall area. The general surface warming also supports enhancement of convective activities that dominates the heavy rain category.

The rainfall response is rather muted for latitudes  $20^{\circ}\text{S}\sim 40^{\circ}\text{S}$  and for  $20^{\circ}\text{N}\sim 40^{\circ}\text{N}$ , which is dominated by moderate rain. In the subtropics, there is little or negative change of rainfall, which can be attributed to dynamics. Poleward of the subtropics, rainfall increases and is linked to the thermodynamic response of these rain regimes.

Examination of the moderate rain frequency indicates a peak in the Antarctic Circumpolar Current (ACC) region, in addition to that in the deep tropics. The changes of moderate rain frequency in the Antarctic Circumpolar Current (ACC) system seem to be confined to decreases to the south of the Subtropical Front. Analysis of present day oceanic evaporation data suggests a decreasing trend and less frequent extreme oceanic-atmosphere evaporation events in the area (Gao et al., 2013; Herman, 2015)

As for the change of intensity spectra in different climatology regions under global warming, the tropical belt displays a heavy and light rain increase accompanied by a moderate rain decrease. Subtropical land shows a higher intensity switch in both summer and winter, but a flatter redistribution in the subtropical ocean. In the mid-high latitudes, over land, it reveals a higher intensity switch, while over the ocean they are somewhat disorganized.

Roughly speaking, over the ocean, the summer season becomes flatter and the winter season switches to higher intensity. All of the panels except the desert regions exhibit some common features, including heavy precipitation augment and prevailing moderate rain reduction.

## Chapter 5: Northern Hemisphere mid-latitude storm track inter-annual variability and seasonal prediction

### 5.1 Introduction of NH midlatitude storm track interannual variability

In both hemispheres, the mid-latitude atmospheric weather systems transport a substantial amount of heat and momentum poleward, and these transient eddy transports play the leading role in maintaining the climatology of the temperature distribution and other fundamental features of the atmospheric general circulation. Mid-latitude storms also serve as an energy source for much of the lower-frequency fluctuation of the extratropical circulation through mean-wave interactions. From the synoptic perspective, storm tracks are regions where synoptic-scale cyclones are prevalent. These storm tracks usually lie in the mid-latitudes and contribute much of the total and extreme precipitation climatology (Hawcroft et al., 2012; Pfahl and Wernli, 2012) and strong winds, and with potentially associated storm surges are thus among the major natural hazards of these regions (Leckebusch and Ulbrich, 2004; Pinto et al., 2007; Schwierz et al., 2010). Blackmon (1976) showed that, in the Northern Hemisphere (NH), there are two variability peaks of 500-hPa geopotential height fields over the mid-latitude oceanic regions, which correspond closely to the locations of maximum synoptic-scale cyclone activity. Interestingly, these two peak regions of cyclone activity are located over the two major oceanic frontal zones, the Kuroshio and Gulf Stream extensions over the mid-latitude oceans and form two distinct tracks: the North Pacific branch and North Atlantic branch (Graff and LaCasce, 2012).

There have been many previous studies of the interannual variability of these two storm tracks. The lower frequency variability of the storm track is generally analyzed using the

monthly variance field of the synoptic variations. For instance, Lau (1988) documented the dominant patterns of mid-latitude storm-track variability on time scales of a month or longer, and identified the boreal winter pattern using the empirical orthogonal function (EOF) decomposition on the hemispheric fields of the operational atmospheric analysis data produced by the National Meteorological Center. The first two leading modes of storm track variability in both the North Pacific and North Atlantic sectors represent monopole patterns overlaid on the major storm track background, and dipole patterns straddled over the climatological mean storm tracks. The mono-sign structure is dominated by the center in the North Pacific sector, while the dipole structure is dominated by the one in the North Atlantic sector. Also examining the EOF-based hemispheric storm track modes, Chang and Fu (2002) suggest that the strengths of the two storm tracks can fluctuate coherently on interannual time scales. They also suggest the existence of a hemisphere-scale pattern of NH storm track variability due to the fact that the inter-annual and month-to-month variations of the North Pacific and North Atlantic storm tracks are found to be significantly correlated in the winter season based on the National Centers for Environmental Prediction-National Center for Atmospheric Research (NCEP-NCAR) reanalysis datasets. By revealing the high correlations of high-passed 250-hPa meridional wind variances between the North Pacific and Atlantic from reanalysis and observations, results in (Chang, 2004) support the idea of a hemispheric pattern of storm track variability. More recently, Wettstein and Wallace (2010) have performed the hemispheric EOF analyses on both hemispheric and sectorial domains using the ERA-40 monthly variance fields of the high-pass filtered winds. They also reveal the mono-sign and dipole structures in their leading EOF modes of the hemispheric fields. Their further analyses within the North Pacific and Atlantic basins, however, suggest that the storm-track variabilities of the two Northern Hemisphere sectors appear to be largely independent from each other.

Lau (1988) further examines the connections between the leading modes of the two NH sectorial storm track variabilities and the atmospheric lower-frequency teleconnection patterns by correlating the corresponding leading principal components (PCs) of the storm

track modes to the major teleconnection pattern indices defined in Wallace and Gutzler (1981). Detailed connections among storm track variability modes, atmospheric teleconnection patterns and the upper-tropospheric jet streams are also discussed in (Wettstein and Wallace, 2010). The low-frequency variations of the storm track show similar patterns in two sectors. In general, the storm track variability exhibits not only a strengthening or weakening at the locations of climatological center (pulsing) but also latitudinal shifts associated with atmospheric lower frequency variability (Lau, 1988; Yang and Chang, 2006, 2007). In particular, a major variation in the North Pacific is in response to the atmospheric teleconnection pattern of the El Niño-Southern Oscillation (ENSO) cycle associated with atmosphere-ocean interaction. During El Niño years, the Pacific storm track shifts equatorward and downstream (Eichler and Higgins, 2006; Straus and Shukla, 1997; Zhang and Held, 1999), while in La Niña years it shifts in the opposite way. In general, the atmospheric anomalies induced by the persistent underlying surface forcing, such as ENSO, can persist and are thus more predictable on seasonal time scales. On the other hand, the predictability of the atmospheric internal variability is significantly shorter, generally within a month (Palmer et al., 2008; Shukla et al., 2009). Therefore, we speculate a certain part of the storm track variability over North Pacific has higher predictability on seasonal time scales due to its connections with the tropical heating sources associated with ENSO.

In terms of this speculation that the storm tracks over the North Pacific have predictability on seasonal time scales, we will examine the seasonal predictability of the NH storm tracks based on the simulations by state-of-the-art climate models. We will also examine the characteristics of the model simulated storm track variability, and evaluate the relationships between the leading modes of the storm track variability in these two sectors and the major low-frequency atmospheric teleconnection patterns using model simulations, meanwhile examining the sensitivity of these relationships to model resolutions. In particular, we analyze how well our climate models reproduce the observed major features of the storm track variations and their relationships to atmospheric teleconnection patterns,

as well as whether their results are sensitive to the model horizontal resolutions. Moreover, the relationships of the storm track variations between the North Pacific sector and North Atlantic sector are still under debate. In this section, we will analyze the connections of these two NH basins at different horizontal resolutions, and test the model fidelity in simulating the storm track variability of each individual sector.

Outputs from Athena ECMWFS IFS simulations at the resolutions of T159, T511, and T1279 are used for the study of low-frequency variations of the Northern Hemisphere storm track in this section. A caveat of this analysis is that, since the Athena simulations are single member runs, the SST-forced signals cannot be easily detected due to the strong influences of the atmospheric internal variability. As a result, the correlations between the mode of the Pacific storm track shift, and the tropical atmospheric low-frequency variations are generally small. To further study this potential connection, we examine the storm track seasonal predictability using ensemble seasonal hindcasts from the Minerva project. The large number of the ensemble members allows us to reduce the signal-to-noise ratio and separate the SST-forced variability from the atmospheric internal variability. Following (Wettstein and Wallace, 2010), we use the variance of the high frequency meridional wind component as a storm-track indicator. For this purpose, the daily 250 hPa meridional winds from the model output and the ERA40 atmospheric reanalysis for the period of 1958-2001 are first high-pass filtered. The filter used in this study is a 13<sup>th</sup> order Butterworth filter with a 50% cutoff signal at a period of 6 days. The monthly averages of the high-pass filtered wind squared (denoted as  $vv_{250}$  hereafter) are used to measure the monthly intensity of the storm track strength. The high-pass filtered 300 hPa meridional winds ( $vv_{300}$ ) are used in (Wettstein and Wallace, 2010). In our case, the  $vv_{250}$  is used because the 300 hPa winds are not part of the model outputs.

The rest of this chapter is structured as follows. Subsection 2 analyzes the hemispheric patterns of Northern Hemisphere storm track activity of ECMWF atmospheric model simulations. The sectorial patterns from atmospheric model simulations, as well as their connections with atmospheric low-frequency variability are described in subsection 3. The

examination of DJF season storm track predictability is discussed in subsection 4, and the summary is provided in subsection 5.

## 5.2 Hemispheric patterns of storm track activity: the relationship between the North Pacific and Atlantic basins

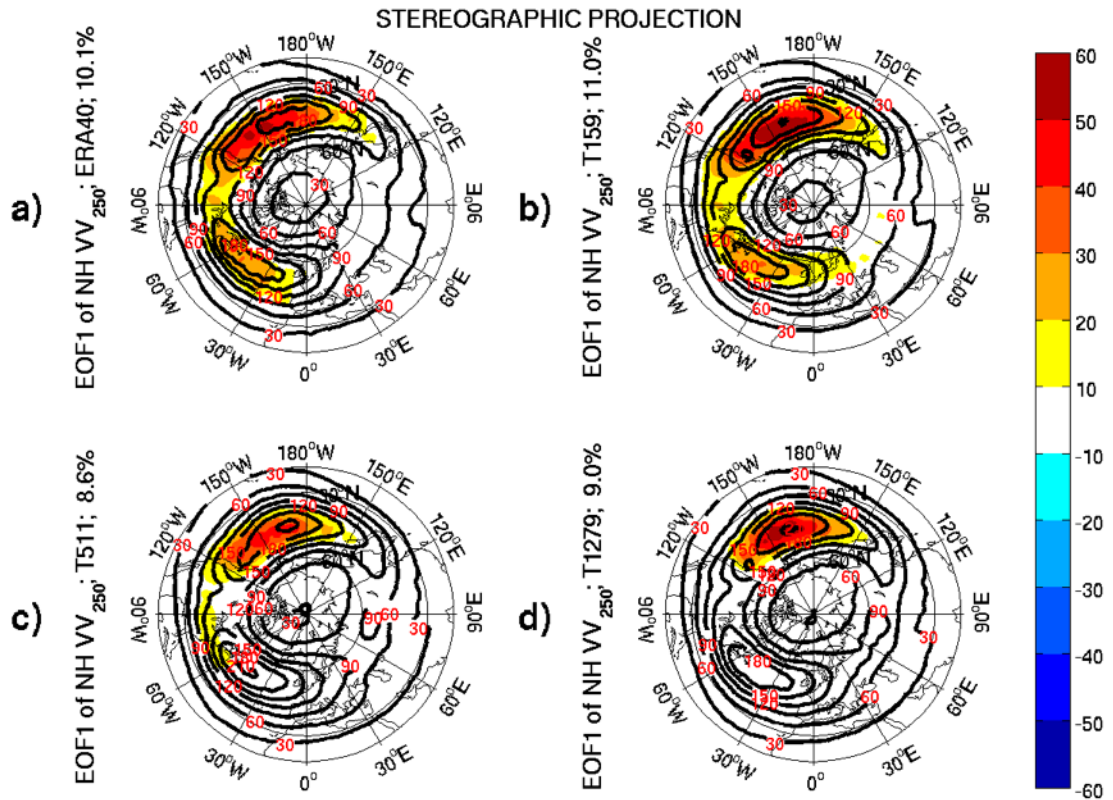


Figure 5.1: EOF1 (color shading) and the climatological mean (contours) of Northern Hemisphere monthly averaged  $vv_{250}$  from the ERA-40 reanalysis for 1958-2001 in panel (a), as well as Athena IFS simulations at T159 in panel (b), T511 in panel (c), and T1279 in panel (d).

In this section, we explore whether the climate model can simulate the observed connection of the North Pacific and Atlantic storm track variability. Before examining the variability,

the IFS model simulated storm track climatologies are compared with the observations (contours, Fig. 5.1). The observations (Fig. 5.1a) show a band of storms stands out in the mid-latitudes with two pronounced centers over North Pacific and North Atlantic basins. The simulations at all three resolutions are able to reproduce the broad structures, including the two peaks over the North Pacific and North Atlantic basins, the weak intensity zone between these two peaks, as well as their realistic positions. In addition, the simulated climatological intensities are also comparable to the observed, even though there are slight overestimations of the two peaks over the oceans. Both the intensity and pattern of the NH storm track climatologies are not notably sensitive to the model horizontal resolutions.

To examine the storm track variability, an EOF analysis of  $vv_{250}$  is applied in the whole NH domain. The storm track variability patterns are expressed by the two leading EOF modes of  $vv_{250}$  and demonstrated by the shading in Figs. 5.1 and 5.12, superimposed with the mean climatology fields. The first variability mode from the EOF analysis (EOF1) based on ERA40 reanalysis data is demonstrated in Fig. 5.11a with 10.9% of the total variance explained. The counterparts based on the outputs from the Athena hindcast runs are generated as well and exhibited in the rest of the panels in Fig. 5.1. The panel for EOF1 from reanalysis data shows the strengthening and weakening of the two storm track centers (shading) exerted on the two climatological-mean storm track branches (contours) over the oceans. This is very similar to EOF1 of the variance of high-pass filtered ERA40 daily 300 hPa meridional wind  $vv_{300}$  shown in Fig. 5.1(upper left panel) of (Wettstein and Wallace, 2010) . As we have mentioned above, the strengthening and weakening of the storm track at its climatological center is usually characterized as the pulsing signal. The spatial pattern of this mode suggests that, as the leading mode of variability, the storm tracks in these two basins pulse (strengthen and weaken) in phase in time.

The leading EOF modes from different simulations show quite different patterns. The pattern from the lowest resolution (T159) simulations (Fig. 5.1b) is consistent with the ERA40 reanalysis and able to capture the gross features of these in-phase relationships between the two basins. In addition, the variance explained in T159 (11.0%) is comparable

to that of the reanalysis (10.9%). However, the pulsing signal in the Atlantic sector vanishes gradually (Fig. 5.1c and d) with resolution increase, indicating that the dominant variability is oriented in the Pacific sector and that this in-phase relationship is not steady. As a result, the leading EOF pattern in the T511 and T1279 simulations are characterized by the pulsing of the Pacific storm track only, with little corresponding variations in the Atlantic sector.

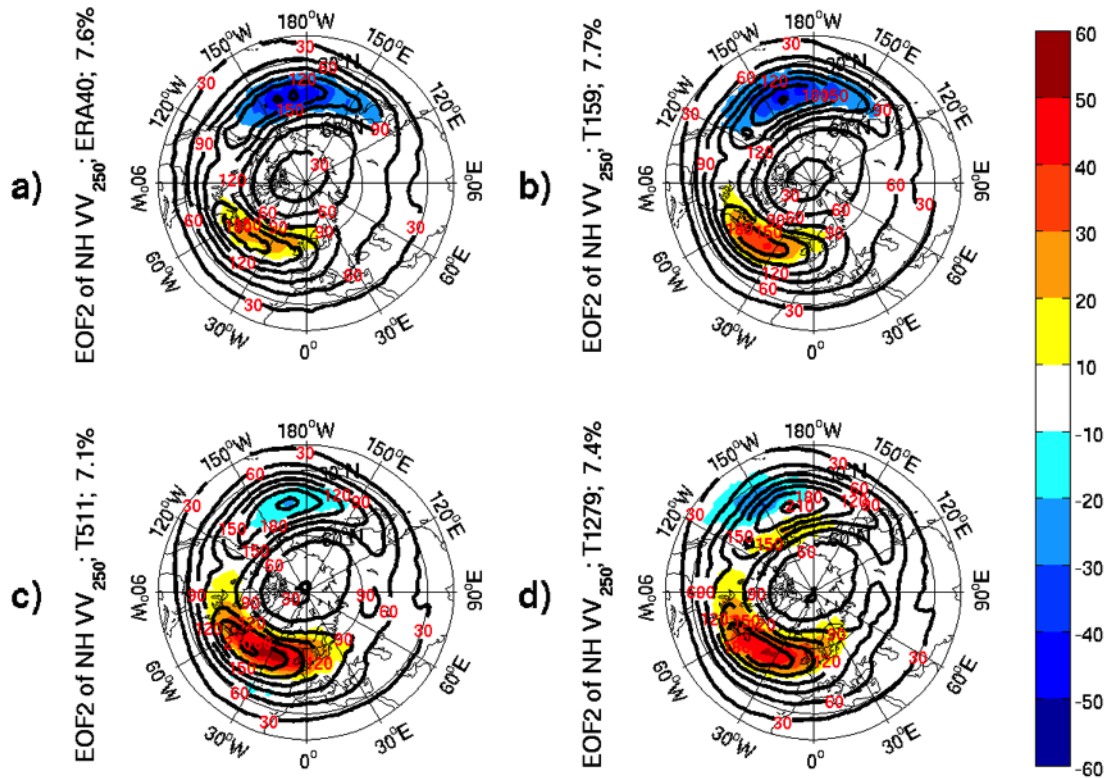


Figure 5.2: Same as Fig. 5.1

The second EOFs from the NH analysis are shown in Fig. 5.2. The panel order of this figure and the rest figures in this section associated with the Athena database is the same as that in Fig. 5.1. The observed EOF2 in Fig. 5.2a represents a seesaw between the strength of the Pacific and Atlantic storm tracks, i.e., their strength is out of phase (one strong, the other weak). This is reminiscent of the EOF2 of ERA40  $vv_{300}$  in (Wettstein and Wallace,

2010) (the left bottom panel of their Fig.1). This mode from observations explains 7.6% of the total variance. The T159 simulation (Fig. 5.2b) again yields the most consistent pattern with the seesaw relations from ERA40 and explains the percentage of total variance (7.7%) very closely to the observed one (7.6%). The T511 and T1279 simulations have an explained variance of 7.1% for the former and 7.4% for the latter. Although the anomalies centered over the North Atlantic storm track are quite robust, the opposing center over the North Pacific weakens as the model resolution increases (Fig. 5.2c and d). Moreover, the signal in the Pacific turns to latitudinal shifting from pulsing in T1279 (Fig. 5.2d). Therefore, the 2nd EOF mode mainly characterizes the pulsing in the North Atlantic sector in T511 and T1279, with little connections to the North Pacific. Combining the two leading EOF modes, we can conclude that the coherent pulsing signals only appear in the relatively low-resolution model simulations. As the model resolution increases, the pulsing occurs more or less independently in the North Pacific and the North Atlantic basins, with the former accounting for more variance.

### **5.3 Sectorial patterns of the storm track activity: connection to the atmospheric low-frequency variability**

Since the variability of the storm track is independent in the NH two sectors, we discuss the individual sectors separately. In this study, we follow the same approach as Chang and Fu (2002) to assign the domains of these two Northern Hemisphere sectors.

### 5.3.1 Leading modes in individual sectors

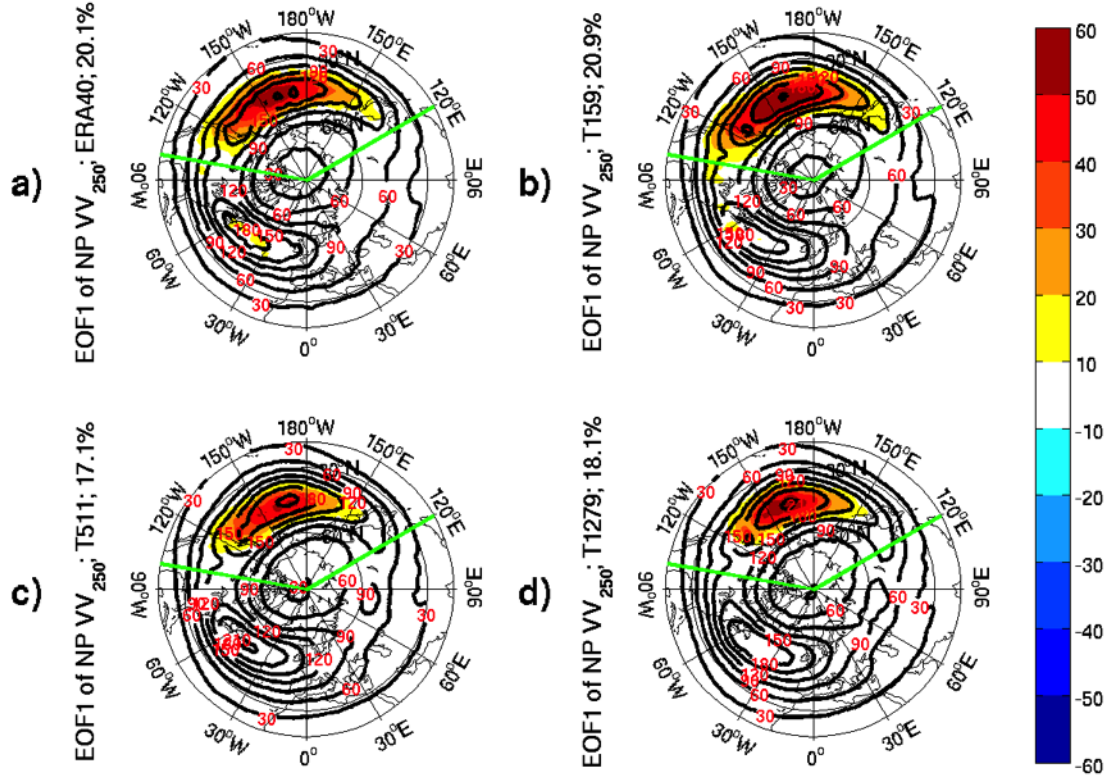


Figure 5.3: EOF1 (color shading) of North Pacific sector, indicated by green lines, monthly averaged  $vv_{250}$  from the ERA-40 reanalysis for 1958-2001 in panel (a), as well as Athena IFS simulations at T159 in panel (b), T511 in panel (c), and T1279 in panel (d). The climatological mean of Northern Hemisphere monthly averaged  $vv_{250}$  from the corresponding dataset is overlaid by contours.

Fig. 5.3 demonstrates the regression pattern over the whole NH domain of  $vv_{250}$  to the principal component (PC1) of  $vv_{250}$  calculated in the North Pacific sector bordered by the two green lines at  $120^{\circ}\text{E}$  and  $110^{\circ}\text{W}$  respectively. Note that, within the bordered domain, the regression pattern is the same as the EOF pattern. The percentage of the total variance explained by this mode for the observations is 20.1%, and 20.9% for T159, 17.1% for T511 and 18.1% for T1279. The observed dominant pattern (Fig. 5.3a) of month-to-month

storm-track variability is characterized by a pulsing on the mean state background. The large amplitudes are restricted in the regions where EOF analysis is performed, except for a small response near the center of the Atlantic storm track. All simulations (Figs. 5.3b-d) are able to successfully reproduce this monopole center over the mean state  $vv_{250}$ . Therefore, this variability mode is not sensitive to model resolution.

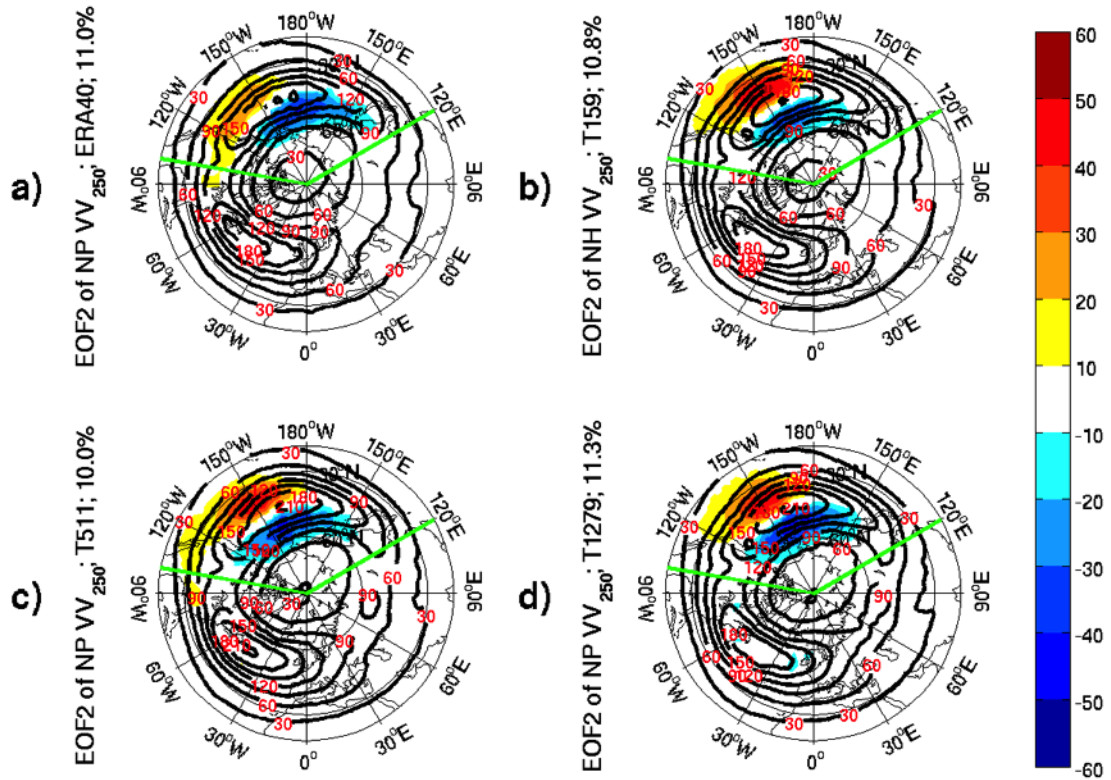


Figure 5.4: Same as Fig 5.3.

The second modes of the North Pacific sector storm track variability (Fig. 5.4 from both observations (Fig. 5.4a) and model simulations are characterized by a dipole structure with its two poles straddling the axis of storm track climatology. This pattern depicts a latitudinal migration of the storm track from its mean state position. These meridional shifts of the storm track tend to be localized within the North Pacific sector, and there

is little downstream effect over the North American continent. This second mode in the observations explains 11.0% of the total variance. All simulations from these three different model resolutions (Fig. 5.4b-d) are able to successfully reproduce this dipole structure. There is no apparent change with model resolution. The percentage of the total variances explained by this mode in simulations for T159 is 10.8%, for T511 10.0%, and for T1279 11.3%.

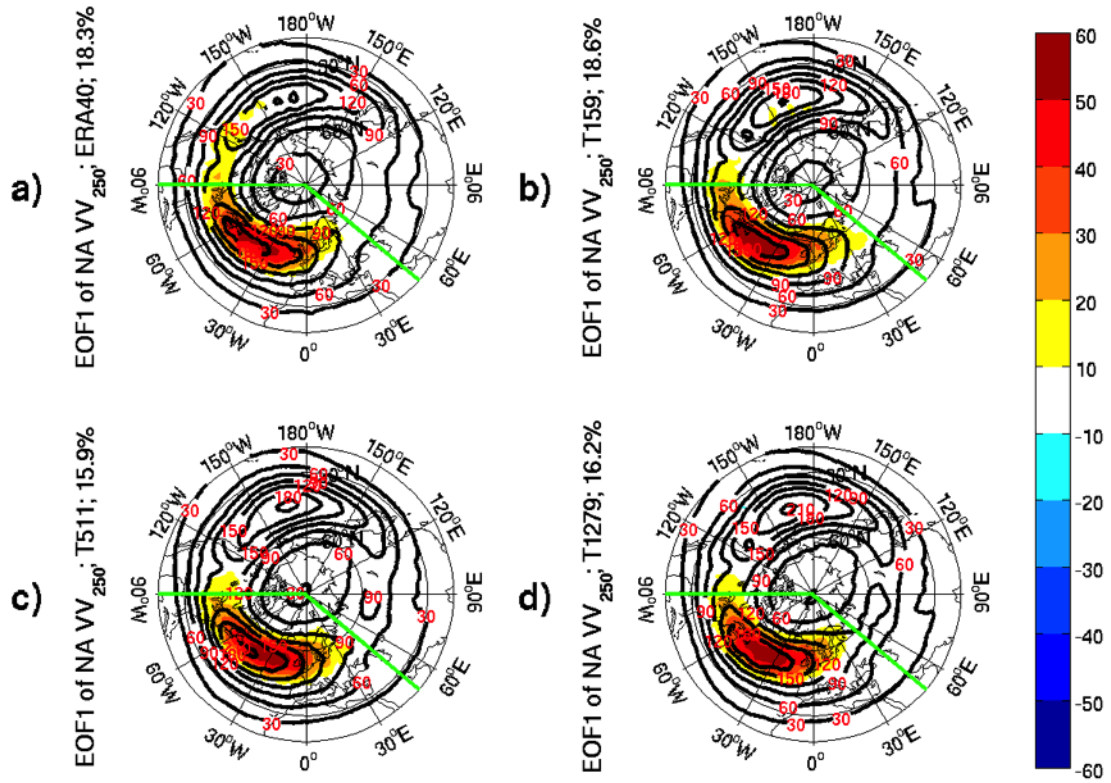


Figure 5.5: EOF1 (color shading) of the North Atlantic sector, indicated by green lines, monthly averaged  $vv_{250}$  from the ERA-40 reanalysis for 1958-2001 in panel (a), as well as Athena IFS simulations at T159 in panel (b), T511 in panel (c), and T1279 in panel (d). The climatological mean of Northern Hemisphere monthly averaged  $vv_{250}$  from the corresponding dataset is overlaid by contours.

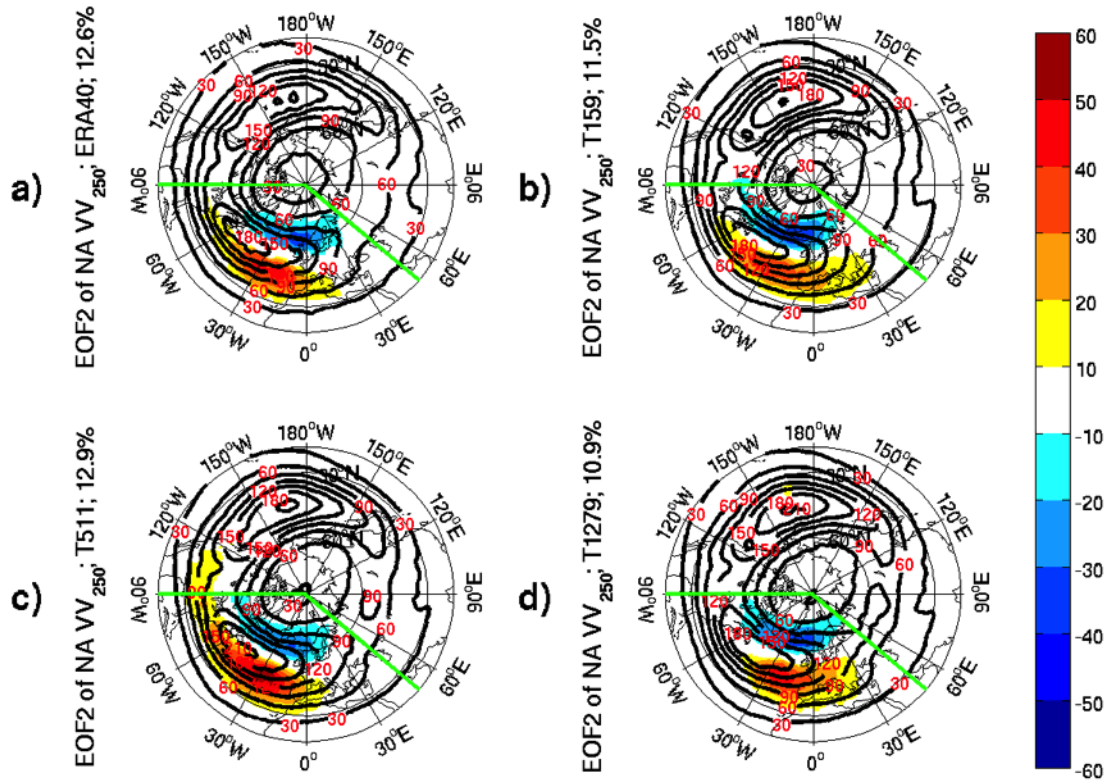


Figure 5.6: Same as Fig. 5.5 but for EOF2 (color shading) of North Pacific sector.

Similar to the North Pacific, the North Atlantic EOF1 of  $vv_{250}$  from both observations (Fig. 5.5a) and model simulations (Figs. 5.5b-d) is characterized by a monopole center over the mean storm track background, while observed (Fig. 5.6a) and simulated (Figs. 5.6b-d) North Atlantic EOF2 consists of a dipole structure, indicating a meridional shift over the climatological-mean storm tracks. The structures of large magnitudes in observed and all simulated panels are restricted within the regions where the EOF analysis is calculated, suggesting that the shift of the storm track activity is largely a regional process. The simulated patterns have comparable percentages of the explained variance with those from observations, and there is no clear sensitivity of patterns to the model resolutions. The modes explain about 17% of the total variance for EOF1, and around 11% for EOF2.

### 5.3.2 Connections to atmospheric low-frequency variability

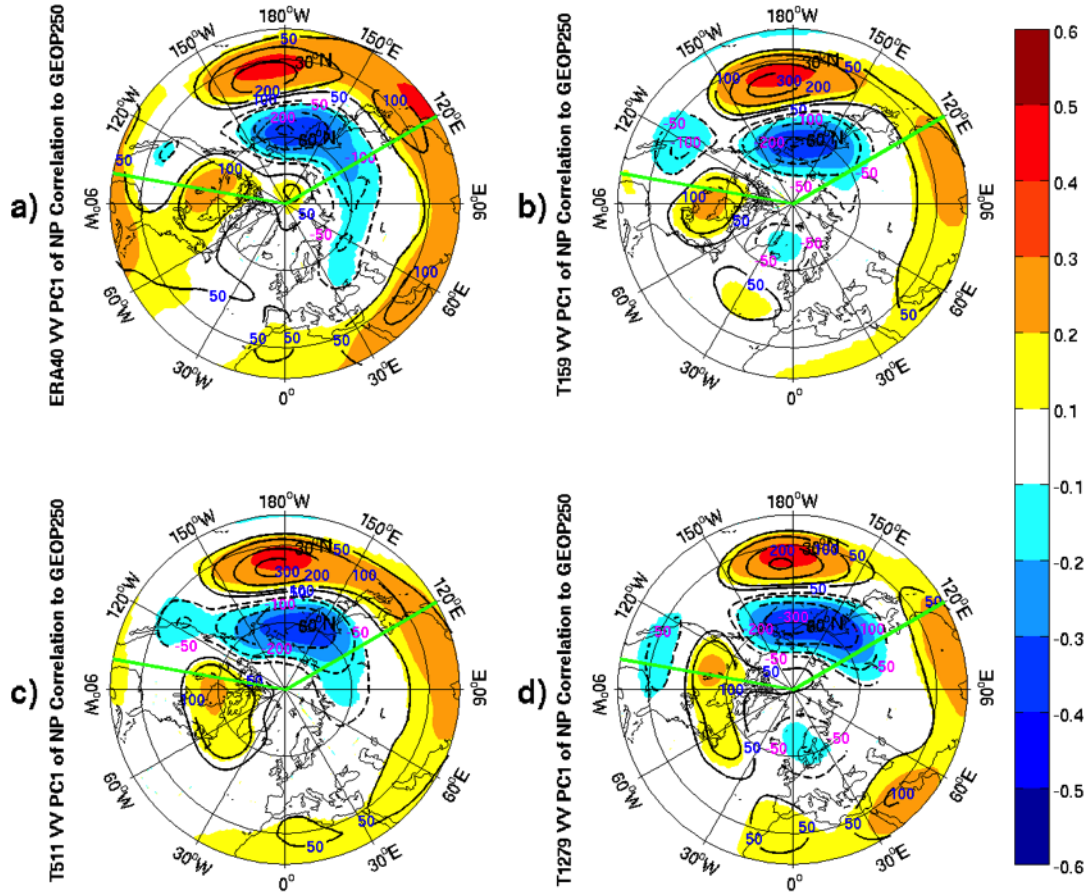


Figure 5.7: The correlation coefficients (color shading) and regression coefficients (contours) between PC1 of the North Pacific sector, indicated by green lines, monthly averaged  $vv_{250}$  and the corresponding layer geopotential height fields from the ERA-40 reanalysis for 1958-2001 in panel (a), as well as Athena IFS simulations at T159 in panel (b), T511 in panel (c), and T1279 in panel (d). Only values of correlation coefficients that pass the significance test are displayed.

To examine the relationship between the modes of storm track fluctuations and the atmospheric lower-frequency variability, we present the correlation patterns of the NH geopotential height with the corresponding PCs of  $vv_{250}$  in each sector. The monthly geopotential

height fields adopted here are also on the 250 hPa level. Only areas with correlation passing the 95% statistical significance level are shaded. We also present the regression pattern of the geopotential height anomalies with the PCs in contours. We firstly focus on the PC1 in the North Pacific sector. The observed correlation panel (Fig. 5.7a) of geopotential height exhibits a spatial distribution similar to the Western Pacific (WP) pattern as described by (Wallace and Gutzler, 1981). With a north-south dipole of anomalies, its one center is located over the Kamchatka Peninsula and the other covers a portion of Southeast Asia and the western subtropical North Pacific. This connection of the North Pacific EOF1 of storm track variability with West Pacific pattern is consistent with that derived by (Wettstein and Wallace, 2010) based on a regression of the WP index with the  $vv_{300}$  fields. The positive phase of the WP meridional dipole with positive anomalies in the southern lobe and negative anomalies in the northern lobe corresponds to anomalously strong westerly winds in the core of the mid-latitude jet stream. Physically, the strengthened westerly wind jet leads to increased storm-track activity (higher  $vv_{250}$ ) downstream.

All simulations (Fig. 5.7b-d) are able to reproduce this WP-storm track relationship qualitatively, especially on the downstream effect of the strengthened or weakened westerly jet. Qualitatively, the model correlation patterns are not sensitive to the model resolution. However, the T159 simulation seems to be closer to the observations by reproducing the secondary geopotential height dipole-like anomalous centers to east of the WP pattern with a reversed sign (Fig. 5.7b). One of the centers is located near the California coast and the other over the North American continent. With increased resolutions, however, these centers shift further eastward and are not as well-paired meridionally (Figs. 5.7c and d).

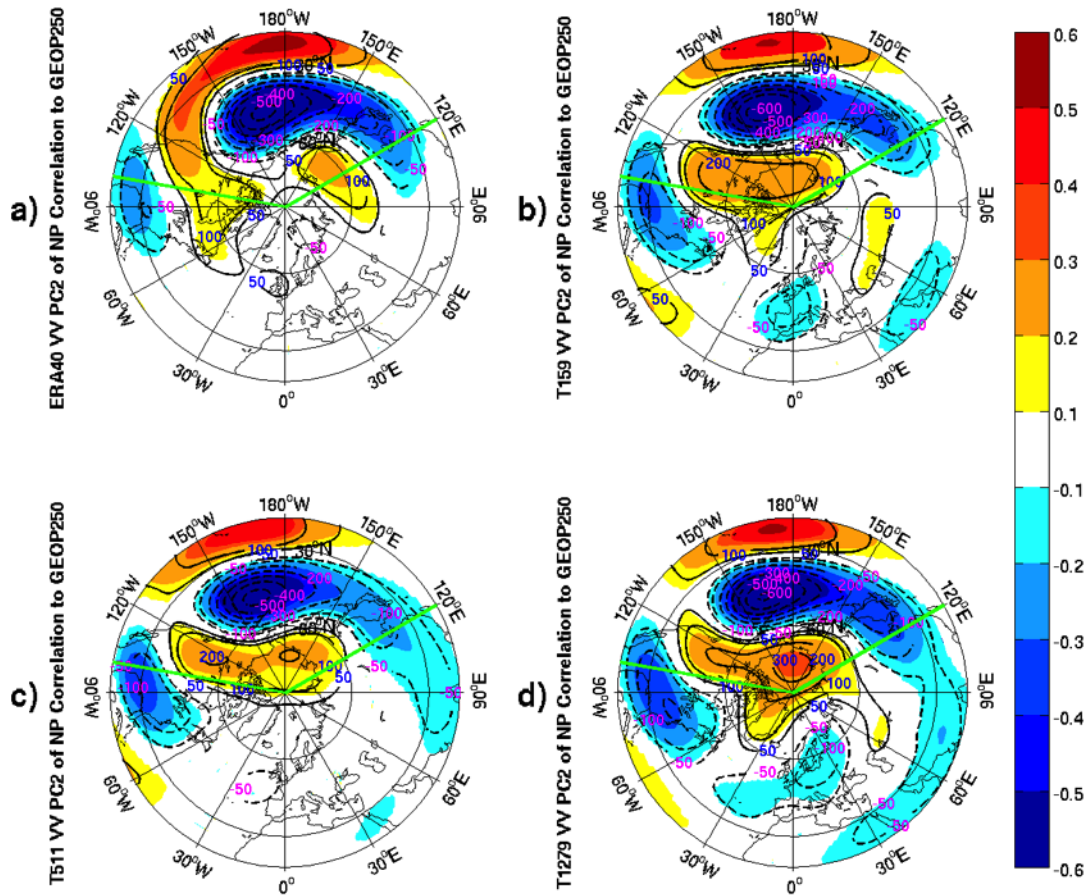


Figure 5.8: The correlation coefficients (shading) and regression coefficients (contours) between PC2 of the North Pacific sector, indicated by green lines, monthly averaged  $vv_{250}$  and the corresponding layer geopotential height fields from the ERA-40 reanalysis for 1958-2001 in panel (a), as well as Athena IFS simulations at T159 in panel (b), T511 in panel (c), and T1279 in panel (d). Only values of correlation coefficients that pass the significance test are displayed.

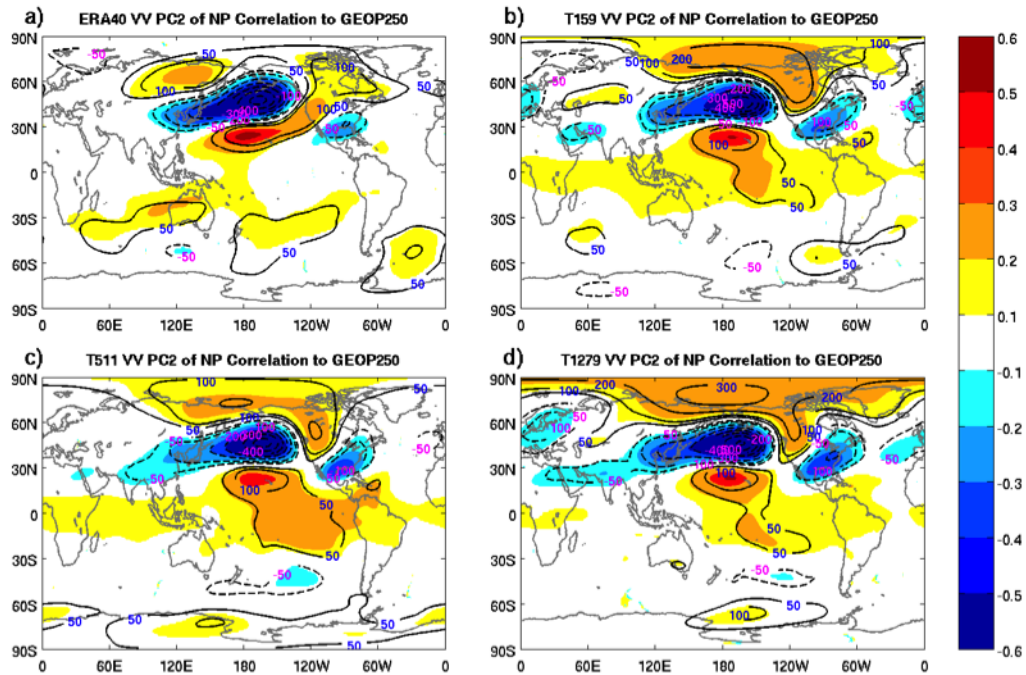


Figure 5.9: Same as 5.8, but in Cartesian coordinate, rather than in spherical coordinate frame.

The correlation structure of the observed NH geopotential height to PC2 of  $vv_{250}$  (Fig. 5.8a) in the North Pacific sector seems to be localized, with negative correlations over the North Pacific and southeastern United States, and with positive correlations in the vicinity of Hawaii. The simulated correlations at all three resolutions (Fig. 5.8b-d) are similar to this observed pattern, but with one more relatively weak positive center over the Intermountain Region of North America. These structures are similar to the Pacific/North American (PNA) pattern described by (Wallace and Gutzler, 1981). When we examine the observed geopotential height structure (Fig. 5.9a) in Cartesian coordinates, it exhibits a dipole oscillation structure over the North Pacific and propagates toward two sides along the Northwest-Southeast direction. But the simulated 250 hPa geopotential height (Figs. 5.9b-d) patterns, when the weaker center is included, display a well-known wave train which

is described in Horel and Wallace (1981). The wave train emanates from the tropical central Pacific region, first propagating poleward to the North Pacific, then curving eastward to North American Intermountain Regions, and finally equatorward to the southeastern United States along a great circle route. This well-known wave train starting from the tropical Pacific is in fact induced by ENSO, suggesting that the storm track variability over the North Pacific is connected with tropical ENSO forcing. In general, all simulations are able to capture these observed pronounced features. There are no substantial differences in the simulation of this structure across all three resolutions.

We also examine the links between the leading modes of storm track variations over the North Atlantic sector and the atmospheric low-frequency variability, and find the pulsing signal associated with EOF1 of  $vv_{250}$  is connected with the North Atlantic Oscillation (NAO), while the meridional shift related to EOF2 of  $vv_{250}$  is linked to the East Atlantic (EA) pattern of the atmospheric low-frequency variability. The simulations from all three resolutions are able to reproduce these relationships, and no clear sensitivity can be detected among resolutions. For brevity, the detailed relationships over North Atlantic sector will not be discussed in this chapter.

## 5.4 Northern Hemisphere storm track DJF mean predictability

Previous studies and our analyses based on the Athena AGCM simulations both suggest the storm track fluctuations are connected with ENSO. The atmospheric anomalies induced by the persistent underlying surface forcing, such as ENSO, can persist and are thus more predictable on seasonal time scales. Finally, we examine the seasonal predictability of the Northern Hemisphere storm track variability. Because of the dominance of the DJF variability in the full month analysis of the Northern Hemisphere, we analyze the predictability based on the DJF mean values in this chapter, using the ECMWF coupled model ensemble hindcast runs with two different atmospheric resolutions (T319 and T639) initialized at

November 1 for 1979-2012.

### 5.4.1 Prediction skill and skillful regions

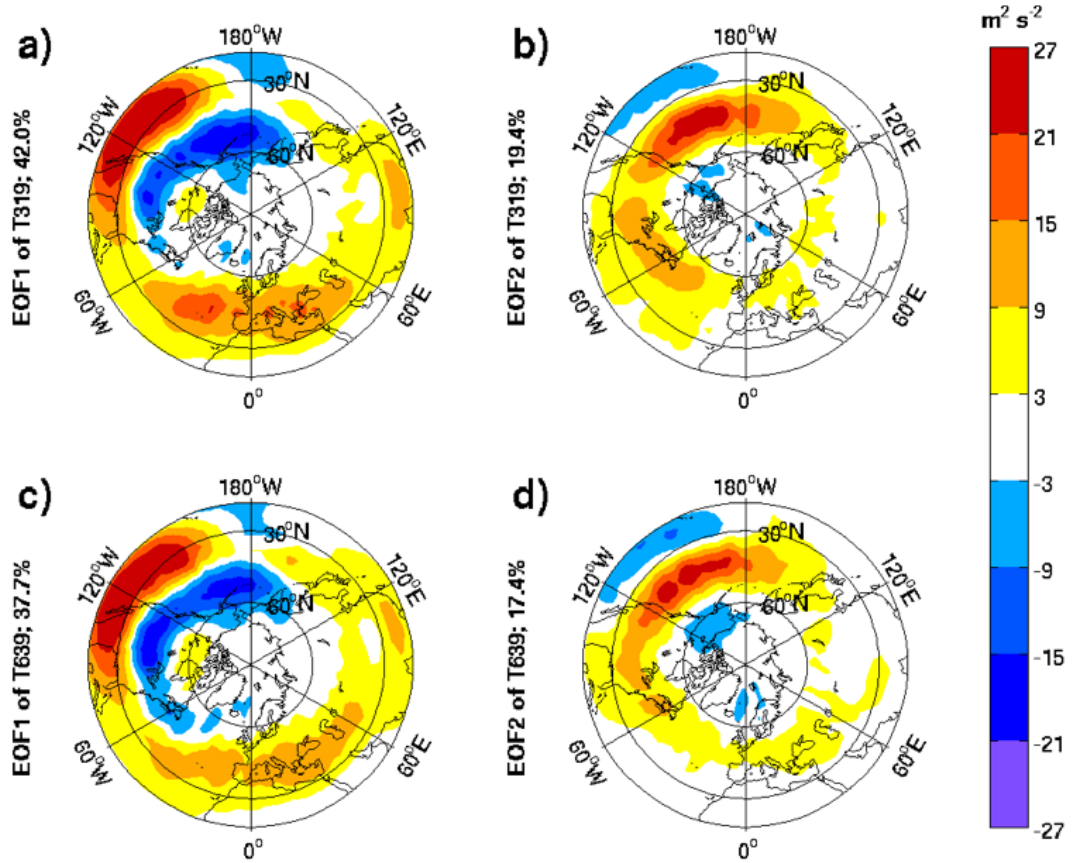


Figure 5.10: The leading modes of the ensemble mean from Minerva simulated NH DJF mean  $vv_{250}$ . EOF1 from T319 in (a), EOF2 from T319 in (b), EOF1 from T639 in (c), and EOF2 from T639 in (d).

To study the storm track predictability, EOF analysis is applied to the DJF  $vv_{250}$  from the ECMWF coupled model ensemble hindcast runs. The first two leading modes of Northern Hemisphere  $vv_{250}$  from the ensemble means of the T319 and T639 hindcasts are exhibited in Fig. 5.10. Both leading modes from T319 are very similar with the corresponding ones

from T639. In particular, EOF1s from T319 (Fig. 5.10a) and T639 (Fig. 5.10c) both show a dipole structure over the North Pacific basin with positive values in the southern lobes and negative values in the northern lobes, as well as some weak downwind effects over the North American continent and over the North Atlantic. The primary features of this pattern are the north-south oriented dipole over the North Pacific, which implies a meridional displacement of storm track position somewhat downstream of the climatological storm track center. In fact, the first leading mode explains around 40% of the variance in both resolution runs, which accounts for a significant amount of the total variance of the ensemble mean anomalies. EOF2s in both T319 (Fig. 5.10b) and T639 (Fig. 5.10d) are also similar to each other, and they both demonstrate a monopole pattern over the mid-latitude North Pacific with weak downwind effects, as well as with weak lower latitude feedback in an opposite sign. The monopole pattern over the North Pacific basin is the key feature, and is an indication of strengthening and weakening signals acting on the climatological-mean storm track. The second mode also explains a large amount of total variance with 19.4% in T319 and 17.4% in T639. Overall, the dominant variability of the Northern Hemisphere EOF1 and EOF2 of the ensemble-averaged  $vv_{250}$  is located in the North Pacific sector. In addition, these two leading modes are different from the counterparts discussed in the last section based on ECMWF atmospheric simulations. That is because the data adopted in this section are the 15-ensemble DJF means from the coupled ECMWF model, rather than those from the monthly means of atmospheric model simulations used in the previous section.

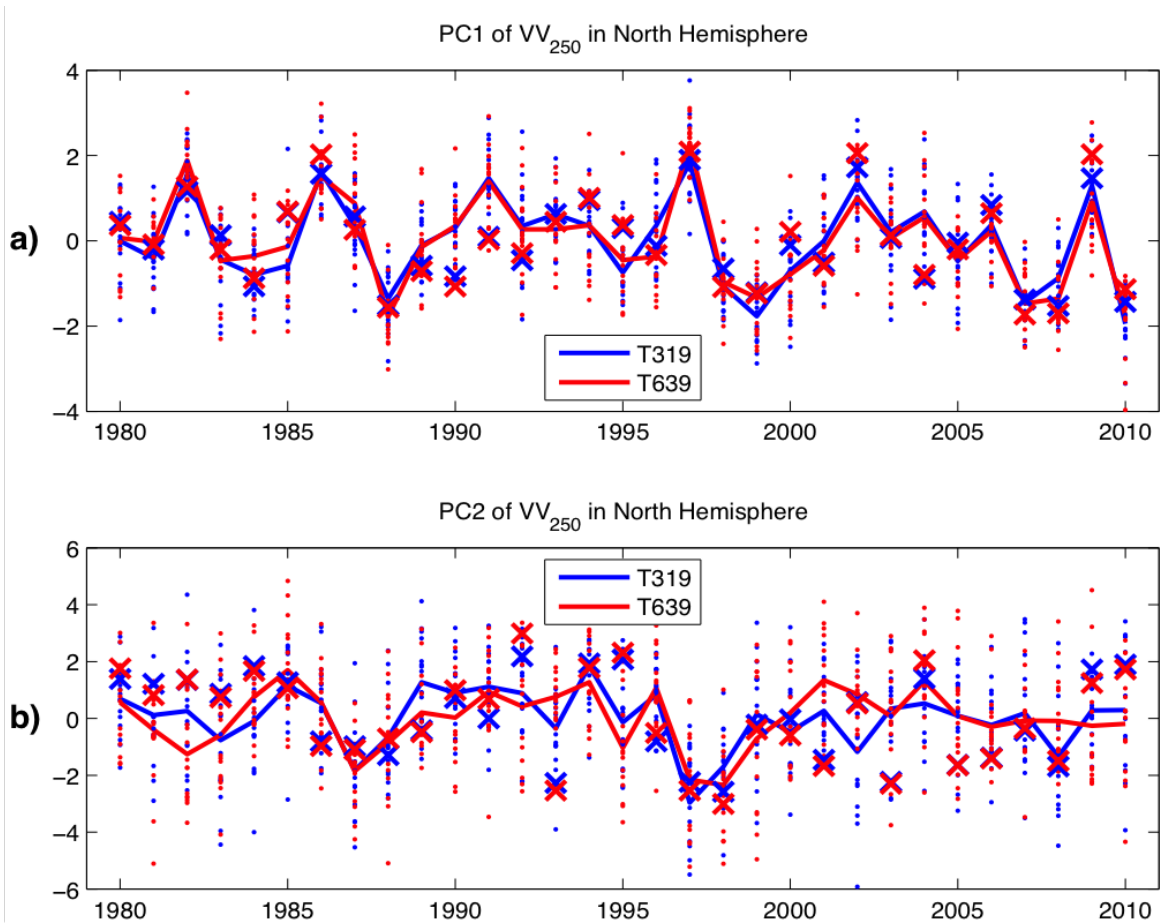


Figure 5.11: Minerva T319 PC1 (blue solid) and T639 PC1 (red solid) of  $vv_{250}$ , the time series of ERA-Interim  $vv_{250}$  projected onto T319 PC1 (blue cross) and onto T639 PC1 (red cross), as well as the time series of T319  $vv_{250}$  from individual simulations projected onto T319 PC1 (blue dots) and the time series of T639  $vv_{250}$  from individual simulations projected onto T639 PC1 (blue dots) shown in (a). T319 PC2 (blue solid) and T639 PC2 (red solid) of  $vv_{250}$ , the time series of ERA-Interim  $vv_{250}$  projected onto T319 PC2 (blue cross) and onto T639 PC2 (red cross), as well as the time series of T319  $vv_{250}$  from individual simulations projected onto T319 PC2 (blue dots) and the time series of T639  $vv_{250}$  from individual simulations projected onto T639 PC2 (blue dots) shown in (b). All  $vv_{250}$  in this figure are based on NH DJF mean.

The other part of the leading EOFs is the leading principal components (PCs). The first two leading PCs of North Hemisphere DJF  $vv_{250}$  are shown in Fig. 5.11. Our analyses show that these two leading PCs of the 15-ensemble mean from between T319 and T639 are highly correlated, with the correlation coefficient for PC1 (Fig. 5.11a) being 0.94 and for

PC2 (Fig. 5.11b) 0.70. Since these two EOF modes are not sensitive to these two hindcasts, we define them as the high predictability components of the storm track variations. The higher correlation coefficient of PC1 between the two sets of hindcasts suggests EOF1 has higher predictability than EOF2.

We further examine their predictive skill by projecting the observed Northern Hemisphere  $vv_{250}$  to these two leading PCs, and obtain two projected PCs (cross marks) from observations. The correlation coefficient between PC1 from T319 and the projections from observations is 0.79, and the correlation coefficient between PC2 and the observed projection is 0.50. Similarly, the correlation coefficient for PC1 between T639 and the observations is 0.80, and the coefficient for PC2 is 0.32. All of the values pass the 95% confidence test, indicating the model has prediction skill associated with these two modes, with higher skills for EOF1 than EOF2. Further projection of Northern Hemisphere  $vv_{250}$  from each individual run onto these two leading PCs (dots) indicates ensembles from T319 and T639 have comparable spreads. The resolution altering has no significant influence on the spreads of variability.

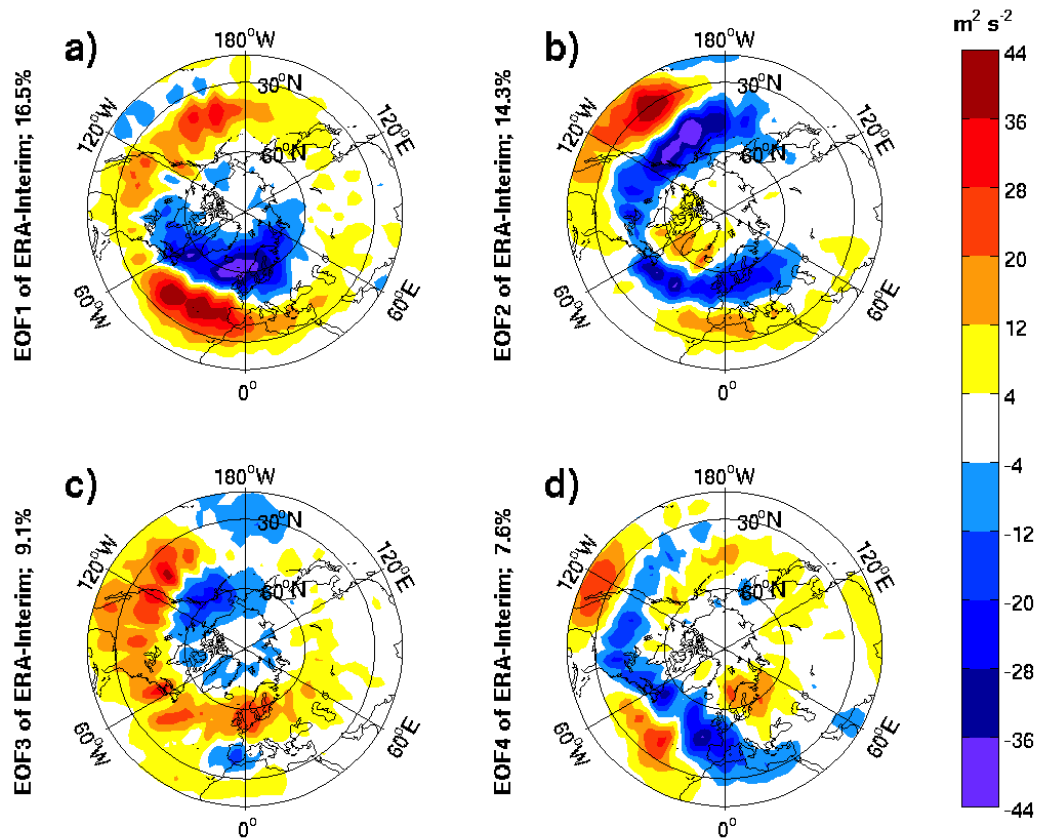


Figure 5.12: The leading fourth modes of observed NH DJF mean  $vv_{250}$  EOF1 in (a), EOF2 (b), EOF3 (c), and EOF4 in T639 (d)

Since the model has prediction skill for Northern Hemisphere storm track variability, are there similar modes in observations? To answer this question, EOF analysis is performed on the  $vv_{250}$  of ERA40 reanalysis data. The leading EOFs are demonstrated in Fig. 5.12. EOF1 (Fig. 5.12a) shows a main dipole pattern over the North Atlantic basin, as well as some weak effects over the North Pacific sector. EOF2 (Fig. 5.12b) displays another dipole structure over the North Pacific sector, and some features over the North Atlantic basin. EOF3 (Fig. 5.12c) and EOF4 (Fig. 5.12d) each present a pattern over both the North Pacific and North Atlantic, with more complicated spatial structures. None of these four modes are particularly similar in structure to the leading EOFs of the ensemble mean  $vv_{250}$

in the simulations, but some similarities do exist. For example, the dipole part of EOF2 (Fig. 5.12b) over the North Pacific well resembles the main features of the simulated EOF1. As discussed above, the dipole structure over the North Pacific sector is related to external variability of underlying surface forcing, while the distinctions over the North Atlantic are associated with the atmospheric internal variability. This suggests that observed leading modes are mixed patterns between atmospheric internal variability and external variability. However, the modes from the simulated ensemble mean all primarily show the patterns associated with external forcing over the North Pacific. The disparities between observations and the ensemble mean from simulations can be explained by the observations being based on only one case so that the noise level might be higher, while the ensemble average reduces the internally generated atmospheric weather noise present in the individual simulation, increasing the effects from external forcing (Schneider and Fan, 2007).

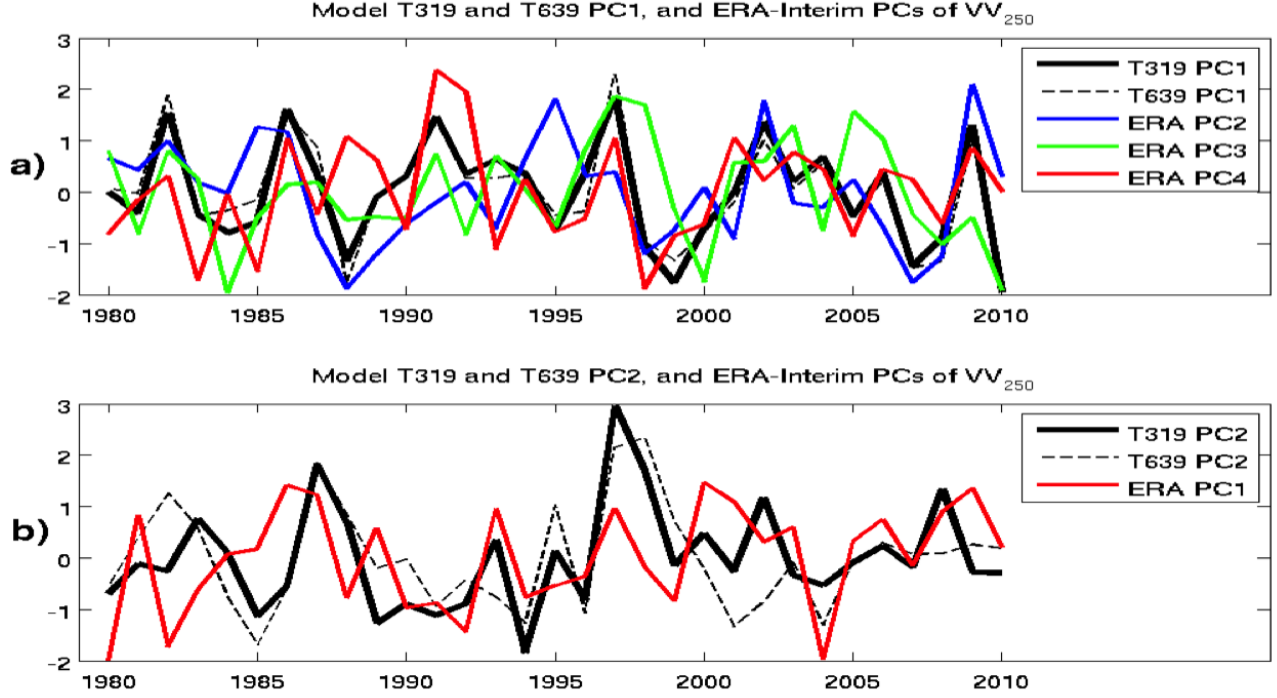


Figure 5.13: Minerva T319 PC1 and T639 PC1 of NH DJF mean  $vv_{250}$ , and observed PCs significantly correlated with T319 PC1 in (a). T319 PC2 and T639 PC2, and observed PCs significantly correlated with T319 PC1 in (b).

Table 5.1: Correlation coefficients between first two leading PCs of Minerva T319 and observed four leading PCs of NH DJF mean  $vv_{250}$

	ERA PC1	ERA PC2	ERA PC3	ERA PC4
T319 PC1	0.06	<b>0.44</b>	<b>0.47</b>	<b>0.47</b>
T319 PC2	<b>0.37</b>	0.16	0.26	0.21

As we have discussed, the observed modes are mixed patterns. Thus we speculate their components from the external forcing are related to the simulated high predictability modes. To examine these relationships, correlation analyses between the observed leading PCs and the simulated PCs corresponding to the high predictability modes are performed. As discussed above, simulated PC1 and PC2 in T319 are highly correlated to the corresponding ones in T639. The correlation coefficients between T319 and observations must be very close

to the ones between observations and T639. For brevity, therefore, the correlation analysis is only performed between observations and T319, and the results are listed in 5.1 with values passing the significance test of 95% confidence level in red bold. The analysis shows the first high predictability mode (EOF1) from the simulated ensemble mean is associated with the observed EOF2, EOF3 and EOF4, while the observed EOF1 is associated with the second highest predictability mode (EOF2) from simulations. The simulated PC1 and its significantly correlated PCs from observations are shown in Fig.5.13a, as well as the simulated PC2 and the PCs from observations significantly correlated with it in Fig. 5.13b.

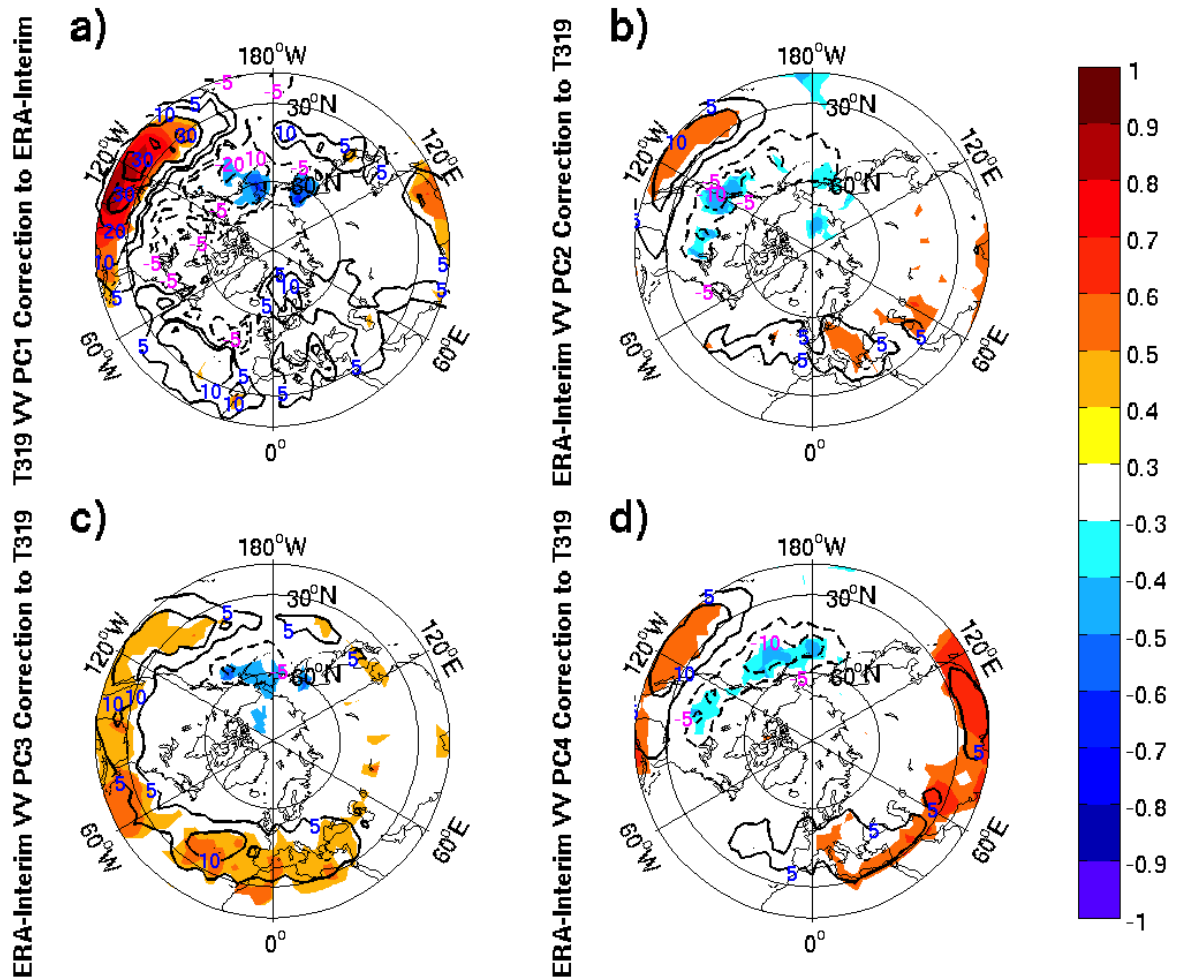


Figure 5.14: Correlation coefficients between Minerva T319 PC1 of NH DJF mean  $vv_{250}$  and observed NH DJF mean  $vv_{250}$  in (a), between observed PC2 and simulated T319 in (b), between observed PC3 and simulated T319 in (c), and between observed PC4 and simulated T319 in (d).

Now we investigate the skillful regions using correlation and regression analysis. The grid-to-grid correlation coefficients between observed  $vv_{250}$  and the simulated PC1 are shown in Fig. 5.14a, with the regression coefficients overlaid by contours. Only the values of correlation coefficients passing 95% significance level are shaded. The correlation structure showing the skillful region for EOF1 is located in the Pacific west of California. Combination of the correlation coefficients with the regression coefficients suggests this skillful

region represents the south lobe of the dipole pattern over the North Pacific. Moreover, the simulated EOF2 has lower prediction skill than EOF1, and it is significantly associated with observed EOF1. Correlation analysis reveals the predictability is reflected on the coastline of Canada (not shown). The main feature of EOF1 from ERA40 is the dipole pattern over the North Atlantic. However, this part is connected with the atmospheric internal variability of the East Atlantic pattern, and thus has a shorter timescale than the external forcing and lower predictability, so that it does not emerge in the correlation pattern, leaving a very small region of the western coastline of Canada alone.

On the other hand, the observed leading modes must be reflected in the simulations because the simulated PCs of  $vv_{250}$  are significantly correlated with the PCs from observations. In addition, the observed leading EOFs are mixed patterns from both internal and external variability. To explore which parts of the observed EOFs are associated with these two high predictability modes, correlation and regression analyses between PCs from ERA40 and the ensemble mean of simulated  $vv_{250}$  are likewise studied. The highest predictability component is EOF1, which is significantly correlated with the observed EOF2, EOF3 and EOF4. We first explore the observed modes related to this highest predictability component (simulated EOF1). The correlation structure between observed PC2 and the simulations (Fig. 5.14b) shows the model predictability is associated with the dipole structure of observed EOF2 over the North Pacific. This is understandable because the dipole of storm track variability over the North Pacific is linked to the external forcing, and thus has high predictability. The correlation analysis based on the observed PC3 (Fig. 5.14c) exhibits a weak band, extending from East Pacific eastward to the European Continent. This band is also presented in the simulated EOF1 (Figs. 5.10a and 5.10c). However the correlation coefficients are too small and thus contain little meaning, even though they pass the significance test. The correlation pattern related to PC4 also shows a dipole structure over the North Pacific, and some features over the South Asian Continents. The dipole structure over the North Pacific has been discussed, but those over South Asia are hard to explain. One possible reason is that this mode has too high order, so that the mechanism is

difficult to understand. Although this model has prediction skill for Northern Hemisphere DJF mean storm track variability, the observed fluctuations mostly result from the atmospheric internal variability so that only a small portion of the observed fluctuations over the North Pacific, which is associated with ENSO, is predictable.

#### **5.4.2 Potential mechanism of the predictability**

We have speculated that these two high predictability modes are associated with the coupled low-frequency variations originating from the tropical Pacific. To verify this speculation and explore the potential mechanism, correlation analyses between the simulated PCs corresponding to the high predictability components and potentially related monthly mean variables (SST, SLP, geopotential height and precipitation) are discussed in this subsection. Because each of the two leading modes is highly correlated both temporally and spatially between the T319 and T639 runs, correlations are investigated only based on T319 run. For the correlations, a statistical significance test is conducted. Values failing to pass the 95% significance level are masked out.

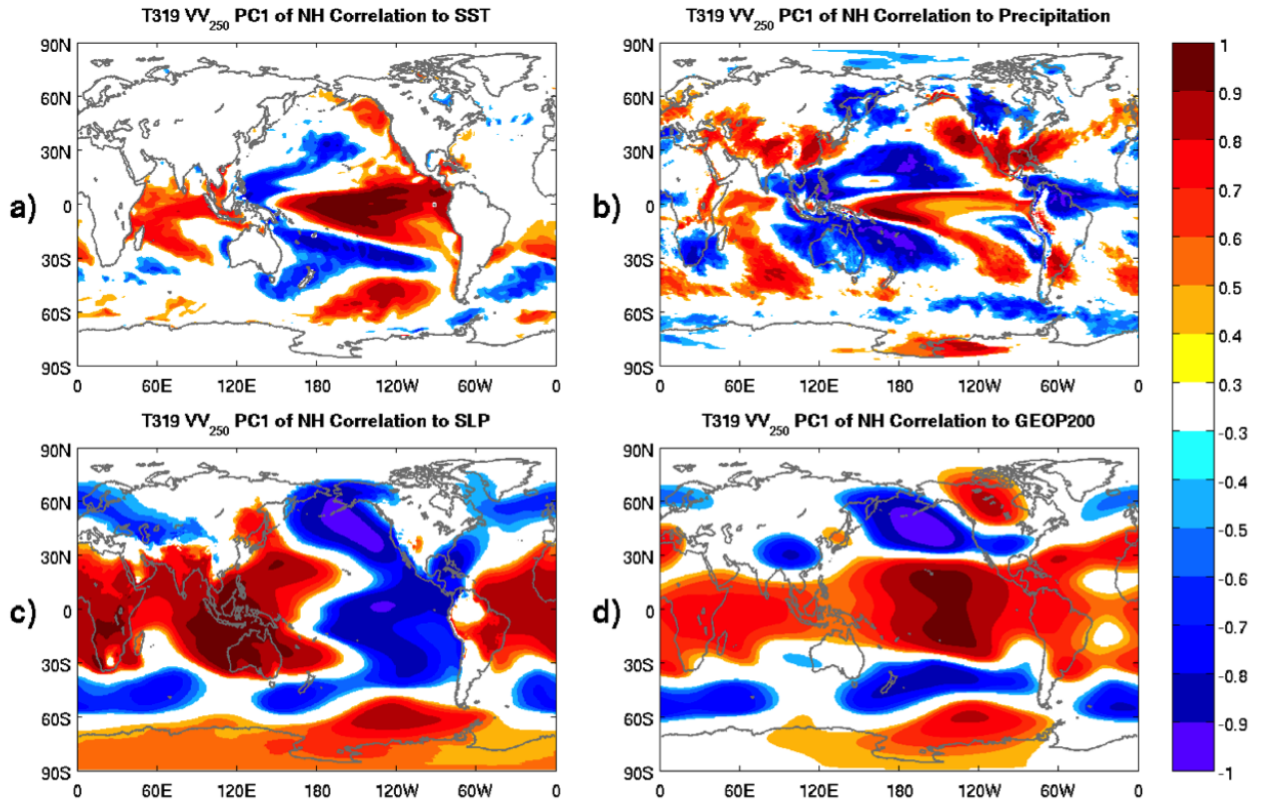


Figure 5.15: Correlation coefficients between Minerva T319 PC1 of NH DJF mean  $vv_{250}$  and SST in (a), between T319 PC1 and precipitation in (b), between T319 PC1 and SLP in (c), as well as between T319 PC1 and 250 hPa geopotential height in (d).

We first correlate PC1 to those variables from the ensemble means of the T319 hindcasts (Fig. 5.15). It is evident that the SST related correlation (Fig. 5.15a) demonstrates the warm phase of ENSO (El Niño) with the typical east-west seesaw structure of SST warmer than normal in tropical central and eastern Pacific, but colder than normal in the western Pacific. The atmospheric component of ENSO is represented in the SLP related correlation panel (Fig. 5.15c). There arises a tendency for SLP in the eastern tropical Pacific to oscillate out of phase with the SLP in the western tropical Pacific and the Indian Ocean. Above analyses with respect to the monthly mean SST and SLP indicate that

these predictable components are induced by the tropical ENSO signal. As we know, the ENSO signal is able to generate deep convection and divergence in the upper troposphere. The correlation analyses are, therefore, applied to the upper level (250 hPa geopotential height) to explore the process of the connections between the tropical ENSO signal and mid-latitude storm track variability, and are shown in Fig. 5.15d. This panel, with respect to 250 hPa geopotential height, shows a well-known ENSO induced wave train emanating from the tropical central Pacific, passing the North Pacific, and propagating to North America. Over the North Pacific, this is known as the PNA pattern. This wave train has been demonstrated observationally by (Horel and Wallace, 1981; Wallace and Gutzler, 1981), analytically by (Hoskins and Karoly, 1981), as well as numerically by (Blackmon, 1976). As obtained in theoretical study (Egger, 1977)), this process is specifically forced by the tropical latent heat released from precipitation. The monthly mean precipitation anomalies can be detected in the precipitation associated correlation pattern (Fig. 5.15b), which well resembles and is induced by the tropical ENSO related SST. In addition, there is a large area of positive precipitation anomalies in the tropical central Pacific, which serves as the source of this well-known wave train.

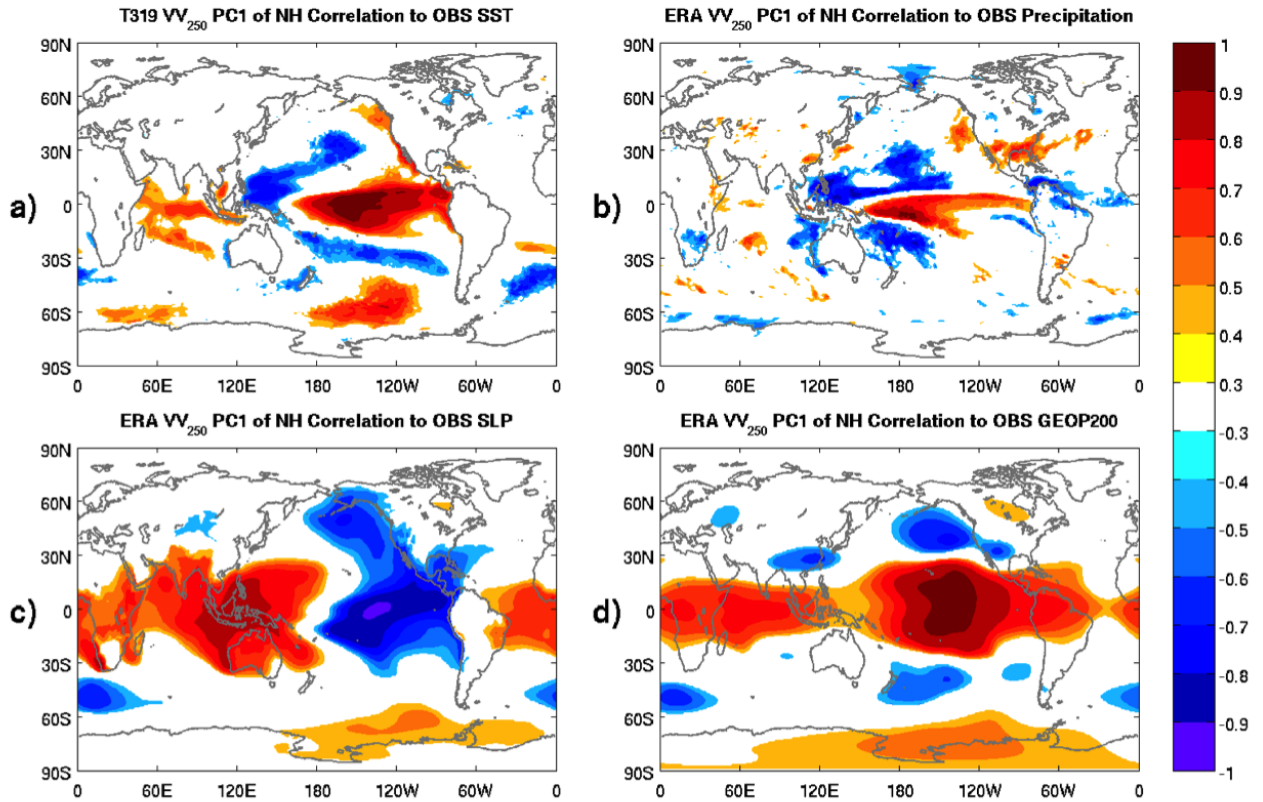


Figure 5.16: Correlation coefficients between Minerva T319 PC1 of NH DJF mean  $vv_{250}$  and observed SST in (a), between T319 PC1 and observed precipitation in (b), between T319 PC1 and observed SLP in (c), as well as between T319 PC1 and observed 250 hPa geopotential height in (d).

Similarly, the correlation between T319 PC1 and those potentially related variables mentioned above from observations are also calculated. The correlation patterns are shown in Fig. 5.16. All correlation structures are similar to the corresponding ones from simulations in Fig. 5.15, but with weaker correlation coefficients. The correlation pattern similarity between simulated T319 and the observations suggests the model well reproduces the process by which ENSO influences the meridional shift of mid-latitude storm tracks. But the lower magnitude of correlation coefficients is in agreement with the results found in other coupled model forecast systems, and can be explained as the ensemble average reducing the noise

present in the individual runs, increasing the correlations and reducing the total noise level (Krishnamurti et al., 2000; Palmer et al., 2000)

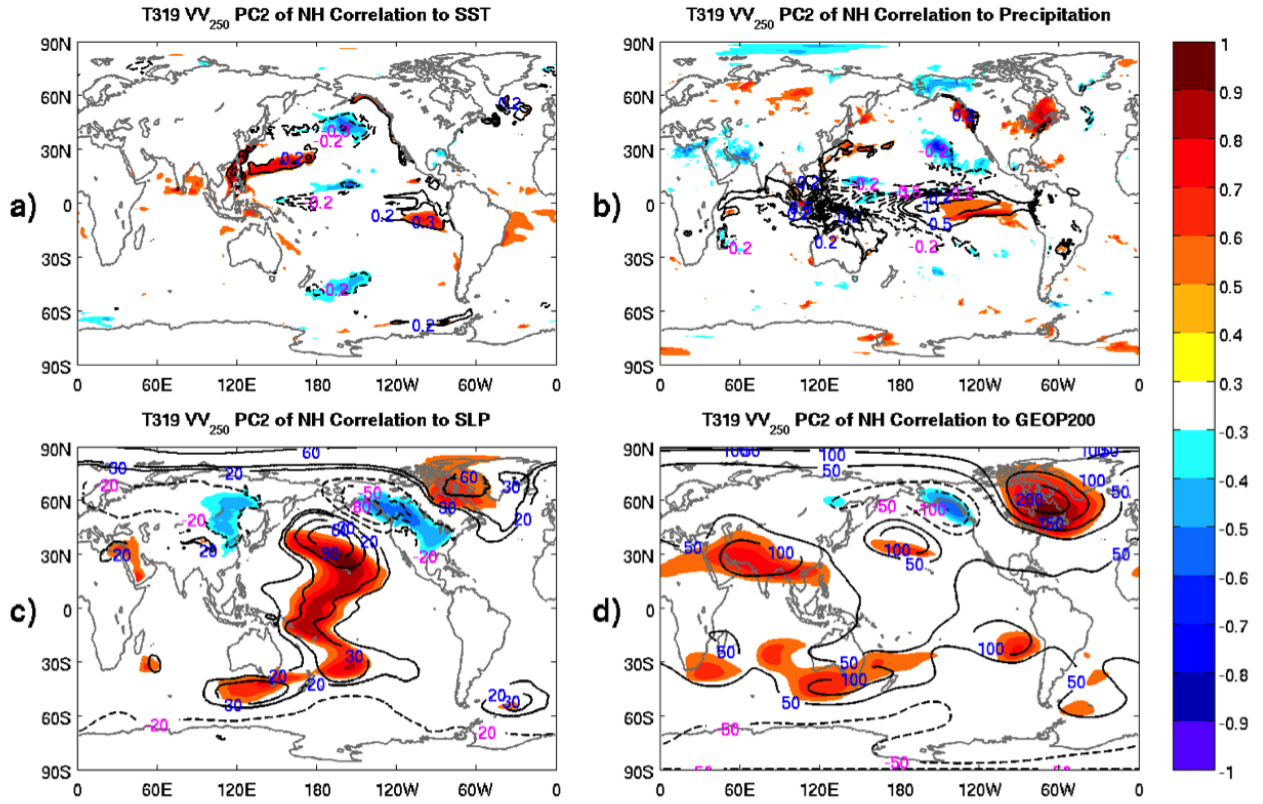


Figure 5.17: Correlation coefficients between Minerva T319 PC2 of NH DJF mean  $vv_{250}$  and SST in (a), between T319 PC2 and precipitation in (b), between T319 PC2 and SLP in (c), as well as between T319 PC2 and 250 hPa geopotential height in (d).

After analyzing the correlations of PC1 of T319, the same method is used for PC2. The correlation patterns between the T319 PC2 and the simulated variables from the T319 run are shown in Fig. 5.17. Analyses reveal that the second highest predictability mode is associated with another wave train (Figs. 5.17c and 5.17d), starting from the tropics and propagating northeastward to Greenland via the central North Pacific and North American

continent. The precipitation pattern (Fig. 5.17b) shows the latent heat source for this wave train is likely from the tropical eastern Pacific. However, the areas passing the significance tests are very limited, which obscures our understanding of this process. To confirm this relationship, further work is needed. Considering its relatively low predictability and small skillful regions, we do not discuss it extensively in this study. In addition, the correlations of PC2 to the observed variables are not shown because the significant regions are even less than the simulated panels (Fig. 5.17).

## 5.5 Summary

Using simulations from different climate models, we have investigated the sensitivity of extratropical NH storm track variability to the model horizontal resolutions by performing EOF analysis on the monthly variance of high-pass filtered meridional winds,  $vv_{250}$ , an indicator of storm track low-frequency variability. The analysis based on the NH domain shows an in-phase relationship of EOF1 and a seesaw relationship of EOF2 of  $vv_{250}$  over the North Pacific branch and North Atlantic branch. These two relationships are qualitatively simulated in the low-resolution run (T159) of the ECMWF IFS atmospheric model. However, when the atmospheric resolution increases, the in-phase relationship gradually disappears, leaving a single monopole structure over the North Pacific center in the highest resolution (T1279) simulation in one mode with the North Atlantic center in the other mode. Meanwhile, the seesaw relation present in observations and the T159 simulation also vanishes gradually with the pulsing signal over the North Pacific branch turning into a dipole in the highest resolution (T1279) run. This suggests both the in-phase relationship and seesaw relationship of storm track variability between two NH sectors are, consistent with (Wettstein and Wallace, 2010), not steady and predominantly “sectorial” rather than “hemispheric” in nature. In this sense, the hemispheric EOF analysis may not be the appropriate method to examine this relationship.

In the individual North Pacific and North Atlantic sectors, both the first EOFs of  $vv_{250}$  from observations show a monopole center over the mean state storm track, and

the second EOFs show that a dipole straddles the climatological mean storm track. The large amplitudes of the spatial patterns are mostly restricted in the defined sectors where EOF analyses are performed. In addition, detailed analyses show that all the correlation coefficients of the two leading PCs of  $vv_{250}$  between the North Pacific sector and North Atlantic sector are very small ( $<0.2$ ), which again suggests the variability over these two basins is largely independent from each other. The simulations from the ECMWF model are not sensitive to the atmospheric resolution either.

The correlation analyses of the PCs of  $vv_{250}$  to monthly geopotential height fields reveal the relationship between the storm track variability and low-frequency atmospheric variability. The observations based on EOF analysis of  $vv_{250}$  show that the pulsing signal corresponding to EOF1 of  $vv_{250}$  over North Pacific sector is associated with atmospheric WP pattern, while the latitudinal shift corresponding to EOF2 over this sector is related to a local atmospheric dipole pattern. In the North Atlantic sector, the pulsing of storm track variability corresponding to the EOF1 of observed  $vv_{250}$  is associated with the atmospheric NAO pattern, but the meridional shift structure corresponding to EOF2 is associated with the EA pattern. The broad features of the atmospheric Western Pacific pattern linked to the EOF1 (pulsing) of  $vv_{250}$  over the North Pacific sector are structurally captured by the ECMWF atmospheric model. In addition, the simulations from this atmospheric model show similar atmosphere low-frequency patterns to the observed connections of the 250 hPa geopotential height with the EOF2 of North Pacific  $vv_{250}$ . The simulations have one more positive center of weak magnitude in North America Intermountain Regions, suggesting the meridional shift of the North Pacific storm track position links to ENSO by a PNA-like wave train. Moreover, the atmospheric patterns (NAO and EA) associated with the North Pacific sector storm track variability are roughly simulated in the ECMWF atmospheric model, as well.

In general, the atmospheric anomalies induced by the underlying surface forcing, like ENSO, have higher predictability on seasonal time scales. In the light of the analysis above, we examine the seasonal predictability of extratropical NH DJF mean storm tracks

using the ECMWF coupled model ensemble hindcast runs with two different atmospheric resolutions. We define the high predictability components of the storm track variations as the two leading EOFs of the ensemble average of the DJF storm track variances from each ensemble member of the hindcasts. These two modes are highly correlated both temporally and spatially between the two sets of hindcasts. EOF1 shows a latitudinal shift of the storm track over the central North Pacific, as well as some downstream response over the North Atlantic. EOF2 is the pulsing signal exerting on the mean storm track background of North Pacific. Projection of observed data onto the corresponding PCs further reveals the model has prediction skill associated with these two modes, with higher skill and larger skillful regions of EOF1 than EOF2. Correlation analysis with respect to the hindcast monthly mean SST and atmospheric fields indicates that these predictable components are generated by the ENSO-induced wave trains. The source for the first mode is located in the tropical central Pacific. This process can also be traced using the atmospheric reanalysis data. The second mode is likely generated from the tropical eastern Pacific.

## Chapter 6: Summary

The earth's climate is a profoundly nonlinear system with different temporal and spatial scales interacting with each other (Palmer, 1999). However, numerical climate models always have limited resolutions in space and time. To explicitly resolve the dynamical interactions of climate variations on widely ranging space and time scales, the climate models need to adopt adequate resolutions so that they are able to accurately represent the major physical processes. Considering the crucial roles of model resolution in climate simulations, three climate processes are discussed with respect to model resolutions using long-term simulations from multiple models with varying horizontal resolutions.

Using climate simulations from coupled and uncoupled general circulation models (GCMs), we first investigate the influences of horizontal resolutions in both atmospheric and oceanic model components on the mean precipitation over the Gulf Stream (GS) region. For this purpose, three sets of model experiments are analyzed. These simulations include the atmospheric GCM runs and a set of coupled ocean-atmosphere seasonal hindcasts. These two simulations examine the effects of increasing the horizontal resolution of an atmospheric GCM gradually from around 100 to 10 km under fixed oceanic settings based on the ECMWF IFS model. Specifically, the AGCM is either forced with prescribed observed SST (Athena hindcasts) or coupled to a non-eddy-resolving ocean general circulation model at a fixed horizontal resolution near 100 km (Minerva hindcasts). Both sets of runs use different AGCM resolutions, the highest at 16 km. The third set of experiments examines the effects of the oceanic model resolution with a pair of long-term simulations by the CCSM coupled ocean-atmosphere general circulation model, in which the OGCM is run both at non-eddy-resolving (100 km) and eddy-resolving (10 km) resolutions, while the AGCM resolution remains fixed at around 50 km for both runs.

In general, all simulations qualitatively reproduce the gross features of the mean GS precipitation and its annual cycle. At similar AGCM resolutions, the uncoupled models more realistically produce a GS rain band in both structure and strength than the coupled models with non-eddy resolving oceans do. This is because the prescribed observed SST better represents the gradient near the oceanic front than the non-eddy-resolving OGCMs simulate. An increase from the baseline AGCM resolution yields enhanced GS precipitation climatology in both large scale and sub-scale precipitation in the North Atlantic, with the latter more tightly confined to the oceanic front. The enhancement, however, is modest, and further increase in resolution achieves diminishing results. On the other hand, an increase in oceanic resolutions from non-eddy-resolving to eddy resolving regimes results in more consistent simulations with observations in both intensity and structure of the rain band. The major increase is in the sub-scale precipitation near the much-tightened SST gradient associated with the oceanic front. Therefore, the intensity improvement caused by changes in oceanic resolution is more effective than the improvement caused by increases in atmospheric resolution. Further analyses show that the improvement of the Gulf Stream precipitation climatology due to increases in model horizontal resolution can be understood in terms of the atmospheric surface pressure adjustment to a sharper SST gradient near the oceanic front, which leads to stronger atmospheric surface convergence and upper level divergence. The associated ascending motion contributes to the precipitation band located in the Gulf Stream.

Another focus of this study is the Greenhouse Gas (GHG) warming impacts on changes in precipitation characteristics. We analyze the changes in global precipitation and large-scale features associated with GHG from simulations obtained from the AMIP and time-slice experiments based on ECMWF IFS runs at 6-hourly time resolutions and a 16-km grid (T1279) and 126-km grid (T159) over 47 years as part of the Athena Project. Rain is categorized into non-rain ( $=0$ ), drizzle ( $0-0.1\text{mm day}^{-1}$ ), light ( $0.1-1.2\text{ mm day}^{-1}$ ), moderate ( $1.2-15\text{ mm day}^{-1}$ ) and heavy rain ( $>15\text{ mm day}^{-1}$ ). The increase rates of the amount of globally averaged precipitation for the high and low resolution simulations are  $1.7\% \text{ K}^{-1}$

and  $1.8\% \text{ K}^{-1}$ , respectively, which are consistent with other estimates. The sensitivities for heavy, moderate, light and drizzle rain are 6.8, -1.2, 0.0,  $0.2\% \text{ K}^{-1}$  for low and 6.3, -1.5, 0.4,  $-0.2\% \text{ K}^{-1}$  for high resolution simulations, in that order. The number of rain days decreases from 317.5 to 309.8 days  $\text{year}^{-1}$  as resolution increases from T159 to T1279. The number of rain days decreases in a warming scenario, with decreases of 3.4 and 4.2 days  $\text{year}^{-1}$  for T159 and T1279, respectively. The sensitivity of the global rainfall of about  $2\% \text{ K}^{-1}$  is less than the sensitivity of columnar water vapor with constant relative humidity computed from models in (O’Gorman and Muller, 2010). The most sensitive response of  $6.3\text{-}6.8\% \text{ K}^{-1}$  for the heavy rain approaches that of the  $7\% \text{ K}^{-1}$  CC scaling limit. The increase in heavy rain and decrease in moderate rain is also consistent with CMIP5 results at the monthly and coarse grid scale. Our results show that the Athena model response is less sensitive in the high resolution (T1279) for heavy rain and more sensitive for moderate rain than in the lower resolution (T159) model.

During the twenty-first century simulation (time-slice), the increases in precipitation are larger over high latitude and wet regions in the low and mid-latitudes. Over the dry regions, such as the subtropics, the precipitation amount and frequency decrease. This increase in heavy precipitation and dehydration in dry regions is mostly attributed to a decrease of precipitation frequency in both categories. There is a higher occurrence of low and heavy rain from the tropics to the mid-latitudes at the expense of the frequency of moderate rain. In addition, under the anthropogenic GHG warming scenario, there is a significant latitudinal redistribution of rainfall with increase in precipitation at low latitude, decreased precipitation at subtropical latitudes, and increased precipitation at high latitudes, which is consistent with some of the observational analyses and simulations. Moreover, in different mean state rainfall areas, the frequency peak of the distribution with intensity linearly increases in climatological regions. The rainfall events within the scope of peak intensities are reduced in a warming climate, while the frequency of events at higher intensities increase in all climatological regions.

In addition to the mid-latitude mean state climate, we explore the high frequency climate of the mid-latitudes. Using the monthly variance of high-pass filtered daily 250 hPa meridional wind as a storm track indicator, the sensitivity of interannual variability of the Northern Hemisphere storm track to model horizontal resolution is investigated based on atmospheric Athena hindcasts. In the ECMWF simulations, the relatively low resolution (T159) simulations effectively reproduce the in-phase EOF mode and the seesaw EOF mode between the North Pacific sector and North Atlantic sector. However, these relationships are not steady with increases in atmospheric resolution, indicating the storm track variability of these two sectors is largely independent. On the other hand, the two leading EOF modes from observations, including pulsing and meridional displacement patterns, of the storm track variability over the individual North Pacific sector and North Atlantic sector can be structurally simulated in the atmospheric model. The simulations are also not sensitive to the atmospheric model resolutions. These two simulated leading modes of storm tracks in each basin are associated with corresponding major teleconnection patterns of the low frequency atmospheric variations. The model results are consistent with the Wettstein and Wallace (2010) observed relationships, and they are not sensitive to the atmospheric model resolutions. In particular, the meridional shift of the North Pacific storm track position is connected to ENSO by a PNA-like wave train.

The connections to ENSO with the meridional shift of the North Pacific storm tracks suggest that the low frequency variations of the storm track strength over the North Pacific have higher predictability on seasonal time scales. Considering this, we examine the seasonal predictability of extratropical North Hemisphere (NH) winter (DJF) mean storm track using the Minerva ensemble hindcasts with two different atmospheric resolutions. In this analysis, we define the high predictability components of the storm track variations as the two leading EOFs of the ensemble average of the DJF storm track variances from each ensemble member of the hindcasts, initialized at November 1 for 1979- 2012. These two modes are highly correlated both temporally and spatially between the two sets of hindcasts. EOF1 shows a latitudinal shift of the storm track over the central North Pacific, as well as

some downstream response over the North Atlantic. EOF2 is the pulsing signal acting on the mean storm track background of the North Pacific. Projection of observed data onto the corresponding PCs further reveals the model has prediction skill associated with these two modes, with higher skill and larger skillful regions of EOF1 than EOF2. Correlation analysis with respect to the hindcast monthly mean SST and atmospheric fields indicates that these predictable components are generated by ENSO induced wave trains, starting from the tropical Pacific, passing through the North Pacific, and propagating to North America. The source for the first mode is located in the tropical central Pacific. The second mode is likely generated from the tropical eastern Pacific.

## Bibliography

- Allen, M. R. and W. J. Ingram, 2002: Constraints on the future changes in climate and the hydrological cycle. *Nature*, **419**, 224–232.
- Barsugli, J. J. and D. S. Battisti, 1998: The basic effects of atmosphere ocean thermal coupling on mid-latitude variability. *J. Atmos. Sci.*, **55**, 477–493.
- Blackmon, M. L., 1976: A climatological spectral study of the 500 mb geopotential height of the Northern Hemisphere. *J. Atmos. Sci.*, **33**, 1607–1623.
- Brankovic, C. and D. Gregory, 2001: Impact of horizontal resolution on seasonal integrations. *Clim. Dyn.*, **18**, 123–143.
- Brayshaw, D. J., B. Hoskins, and M. Blackburn, 2008: The storm track response to idealized SST perturbations in an aquaplanet GCM. *J. Atmos. Sci.*, **65**, 2842–2860.
- Brown, A. R., 2004: Resolution dependence of orographic torques. *Quart. J. Roy. Meteor. Soc.*, **130**, 3029–3046.
- Bryan, F. O., M. W. Hecht, and R. D. Smith, 2007: Resolution convergence and sensitivity studies with North Atlantic circulation models. part i: The western boundary current system. *Ocean Model*, **16**, 141–159.
- Chang, E. K. M., 2004: Are the Northern Hemisphere winter storm tracks significantly correlated? *J. Clim.*, **17**, 4230–4244.
- Chang, E. K. M. and Y. Fu, 2002: Interdecadal variations in Northern Hemisphere winter storm track intensity. *J. Clim.*, **15**, 642–658.

- Chassignet, E. P. and D. P. Marshall, 2008: Gulf Stream separation in numerical ocean models. Ocean Modeling in an Eddy Regime. *Geophys. Monogr.*, **177**, 39–62.
- Chelton, D., 2005: The impact of SST specification on ECMWF surface wind stress fields in the eastern tropical Pacific. *J. Clim.*, **18**, 530–550.
- Chelton, D. B. and F. J. Wentz, 2005: Global microwave satellite observations of sea surface temperature for numerical weather prediction and climate research. *Bull. Amer. Meteor. Soc.*, **86**, 1097–1115.
- Chelton, D. B. and S. P. Xie, 2010: Coupled ocean-atmosphere interaction at oceanic mesoscales. *Oceanography*, **23**, 52–69.
- Collins, W., C. M. Bitz, and Coauthors, 2006: The Community Climate System Model version 3 (CCSM3). *J. Clim.*, **19**, 2122–2143.
- Craig, A., M. Vertenstein, and Coauthors, 2011: A new flexible coupler for earth system modeling developed for CESM4 and CESM1. *Int. J. High. Perf. Comput. Appl.*, **26**, 31–42.
- Egger, J., 1977: On the linear theory of the atmospheric response to sea surface temperature anomalies. *J. Atmos. Sci.*, **34**, 603–614.
- Eichler, T. and W. Higgins, 2006: Climatology and ENSO-related variability of North American extratropical cyclone activity. *J. Clim.*, **19**, 2076–2093.
- Emori, S. and S. J. Brown, 2005: Dynamic and thermodynamic changes in mean and extreme precipitation under changed climate. *Geophys. Res. Lett.*, **32**, L17706.
- Frankignoul, C., 1985: Sea surface temperature anomalies, planetary waves, and air-sea feedback in the middle latitudes. *Rev. Geophys.*, **23**, 357–390.
- Gao, S., L. S. Chiu, and C. L. Shie, 2013: Trends and variations of ocean surface latent heat flux: Results from GSSTF2c data set. *Geophys. Res. Lett.*, **40**, 1–6.

- Gent, P. R., S. G. Yeager, and Coauthors, 2010: Improvements in a half-degree atmosphere/land version of the CCSM. *Clim.Dyn.*, **34**, 819–833.
- Gordon, H. B., P. H. Whetton, and Coauthors, 1992: Simulated changes in daily rainfall intensity due to the enhanced greenhouse effect: implications for extreme rainfall events. *Clim. Dyn.*, **8**, 83–102.
- Graff, L. S. and J. H. LaCasce, 2012: Changes in the extratropical storm tracks in response to changes in SST in an AGCM. *J. Clim.*, **25**, 1854–1870.
- Gregory, J. M. and J. F. B. Mitchell, 1995: Simulation of daily variability of surface temperature and precipitation over Europe in the current and  $2\times\text{CO}_2$  climates using the UKMO climate model. *Quart. J. Roy. Meteor. Soc.*, **121**, 1451–1476.
- Hack, J. J., J. M. Carton, and Coauthors, 2006: CCSM-CAM3 climate simulation sensitivity to changes in horizontal resolution. *J. Clim.*, **19**, 2267–2289.
- Hawcroft, M. K., L. C. Shaffrey, and H. F. Dacre, 2012: How much Northern Hemisphere precipitation is associated with extra-tropical cyclones? *Geophys. Res. Lett.*, **39**, L24 809, doi:10.1029/2012GL053 866.
- Held, I. M. and B. J. Soden, 2006: Robust responses of the hydrological cycle to global warming. *J. Clim.*, **19**, 5686–5699.
- Herman, A., 2015: Trends and variability of the atmosphere-ocean turbulent heat flux in the extratropical Southern Hemisphere. *Scientific Reports*, **5**, 14 900.
- Horel, J. D. and J. M. Wallace, 1981: Planetary-scale atmospheric phenomena associated with the Southern Oscillation. *Mon. Wea. Rev.*, **109**, 813–829.
- Hoskins, B. J. and D. J. Karoly, 1981: The steady linear response of a spherical atmosphere to thermal and orographic forcing. *J. Atmos. Sci.*, **38**.
- Houghton, J. T., Y. Ding, and Coauthors, 2001: *Climate Change 2001: The Scientific Basis*. Cambridge University Press, Cambridge, UK.

- Jung, T., M. J. Miller, and Coauthors, 2012: High-resolution global climate simulations with the ECMWF model in Project Athena: Experimental design, model climate, and seasonal forecast skill. *J. Clim.*, **25**, 3155–3172.
- Kedem, B., L. S. Chiu, and Z. Karni, 1990: An analysis of the threshold method for measuring area-average rainfall. *J. Appl. Meteor.*, **29**, 3–20.
- Kiehl, J. T. and P. R. Gent, 2004: The Community Climate System Model, version 2. *J. Clim.*, **17**, 3666–3682.
- Kinter, J. I., B. Cash, and Coauthors, 2013: Revolutionizing climate modeling with Project Athena: A multi-institutional, international collaboration. *Bull. Amer. Meteor. Soc.*, **94**, 231–245.
- Kirtman, B. P., C. Bitz, and Coauthors, 2012: Impact of ocean model resolution on CCSM climate simulations. *Clim. Dyn.*, **39**, 1303–1328.
- Kobayashi, C. and M. Sugi, 2004: Impact of horizontal resolution on the simulation of the Asian summer monsoon and tropical cyclones in the JMA global model. *Clim. Dyn.*, **23**, 165–176.
- Krishnamurti, T. N., C. M. Kishtawal, and Coauthors, 2000: Multimodel ensemble forecasts for weather and seasonal climate. *J. Clim.*, **13**, 4196–4216.
- Lau, N. C., 1988: Variability of the observed midlatitude storm tracks in relation to low-frequency changes in the circulation pattern. *J. Atmos. Sci.*, **45**, 2718–2743.
- Lau, W. K. M., H. T. Wu, and K. M. Kim, 2014: A canonical response of precipitation characteristics to global warming from CMIP5 models. *Geophys. Res. Lett.*, **40**, 3163–3169.
- Leckebusch, G. C. and U. Ulbrich, 2004: On the relationship between cyclones and extreme windstorm events over Europe under climate change. *Global Planet. Change*, **44**, 181–193.

- Lin, S. J. and R. B. Rood, 1997: An explicit flux-form semi-Lagrangian shallow water model on the sphere. *Quart. J. Roy. Meteor. Soc.*, **123**, 2477–2498.
- Lindzen, R. S. and R. S. Nigam, 1987: On the role of sea surface temperature gradients in forcing low level winds and convergence in the tropics. *J. Atmos. Sci.*, **44**, 2418–2436.
- Madec, G., 2008: NEMO reference manual, ocean dynamics component: NEMO-OPA. preliminary version. *IPSL Note du Pole de modélisation*, **27**, 99.
- May, W. and E. Roeckner, 2001: A time-slice experiment with the ECHAM4 AGCM at high resolution: the impact of horizontal resolution on annual mean climate change. *Clim. Dyn.*, **17**, 407–420.
- Minobe, S., M. Miyashita, A. K. Yoshida, H. Tokinaga, and S. P. Xie, 2010: Atmospheric response to the Gulf Stream: Seasonal variations. *J. Clim.*, **23**, 3699–3719.
- Minobe, S., A. K. Yoshida, N. Komori, S. P. Xie, and R. J. Small, 2008: Influence of the Gulf Stream on the troposphere. *Nature*, **452**, 206–209.
- Molteni, F., T. Stockdale, and Coauthors, 2011: The new ECMWF seasonal forecast system (system 4). *ECMWF Technical Memorandum*, **656**, ECMWF: Reading, UK.
- Nakamura, H., T. Sampe, Y. Tanimoto, and A. Shimpo, 2004: Observed associations among storm tracks, jet streams, and mid-latitude oceanic fronts. Earth’s Climate: The Ocean-Atmosphere Interaction. *Geophys. Monogr.*, **147**, 329–345.
- Nakicenovic, N., R. Swart, and Coauthors, 2003: *Special report on emissions scenarios*, *International Panel on Climate Change*. American Geophysical Union monograph.
- Navarra, A., S. Aualdi, and Coauthors, 2008: Atmospheric horizontal resolution affects tropical climate variability in coupled models. *J. Clim.*, **21**, 730–750.
- O’Gorman, P. A. and C. J. Muller, 2010: How closely do changes in surface and column water vapor follow Clausius-Clapeyron scaling in climate change simulations? *Environ. Res. Lett.*, **5**, 025 207.

- O'Neill, L. W., D. B. Chelton, S. K. Esbensen, and F. J. Wentz, 2005: High-resolution satellite measurements of the atmospheric boundary layer response to SST variations along the AgulhasReturn Current. *J. Clim.*, **18**, 2706–2723.
- Palmer, T. N., 1999: A nonlinear dynamical perspective on climate prediction. *J. Clim.*, **12**, 575–591.
- Palmer, T. N., C. Brankovic, and D. C. Richardson, 2000: A probability and decision model analysis of PROVOST seasonal multimodel ensemble integrations. *Quart. J. Roy. Meteor. Soc.*, **126**, 2013–2033.
- Palmer, T. N., F. J. Doblas-Reyes, A. Weisheimer, and M. J. Rodwell, 2008: Toward seamless prediction: calibration of climate change projections using seasonal forecasts. *Bull. Amer. Meteor. Soc.*, **89**, 459–470.
- Pandergrass, A. and D. Hartmann, 2014: Changes in the distribution of rain frequency and intensity in response to global warming. *J. Clim.*, **27**, 8372–8383.
- Pfahl, S. and H. Wernli, 2012: Quantifying the relevance of cyclones for precipitation extremes. *J. Clim.*, **25**, 6770–6780.
- Pinto, J. G., E. L. Froehlich, G. C. Leckebusch, and U. Ulbrich, 2007: Changing European storm loss potentials under modified climate conditions according to ensemble simulations of the ECHAM5/MPI-OM1 GCM. *Nat. Hazards Earth Syst. Sci.*, **7**, 165–175.
- Pope, V. and R. Stratton, 2002: The processes governing horizontal resolution sensitivity in a climate model. *Clim. Dyn.*, **19**, 211–236.
- Rayner, N. A., D. E. Parker, and Coauthors, 2003: Global analyses of sea surface temperature, sea ice, and night marine air temperature since the late nineteenth century. *J. Geophys. Res.*, **108**, 4407.
- Reynolds, R. W., N. A. Rayner, and Coauthors, 2002: An improved In Situ satellite SST analysis for climate. *J. Clim.*, **15**, 1609–1625.

- Sampe, T., N. Hisashi, G. Atsushi, and O. Wataru, 2010: Significance of a midlatitude SST frontal zone in the formation of a storm track and an eddy-driven westerly jet. *J. Clim.*, **23**, 1793–1814.
- Schneider, E. K. and M. Fan, 2007: Weather noise forcing of surface climate variability. *J. Atmos. Sci.*, **64**, 33 265–3280.
- Schneider, E. K., M. J. Fennessy, and J. K. III, 2009: A statistical dynamical estimate of winter ENSO teleconnections in a future climate. *J. Clim.*, **22**, 6624–6638.
- Schneider, N. and B. Qiu, 2015: The atmospheric response to weak sea surface temperature fronts. *J. Atmos. Sci.*, **72**, 3356–3377.
- Schwierz, P., C., E. Z. Kollner-Heck, and Coauthors, 2010: Modelling European winter wind storm losses in current and future climate. *Clim. Change*, **101**, 485–514.
- Semenov, V. A. and L. Bengtsson, 2002: Secular trends in daily precipitation characteristics: greenhouse gas simulation with a coupled AOGCM. *Clim. Dyn.*, **19**, 123–140.
- Shapiro, M. A. and A. J. Thorpe, 2004: THORPEX International Science Plan, version iii: 2 November 2004. *WMO/TD*, **1246**.
- Shukla, J., R. Hagedorn, and Coauthors, 2009: Strategies: Revolution in climate prediction is both necessary and possible: A declaration at the World Modeling Summit for Climate Prediction. *Bull. Amer. Meteor. Soc.*, **90**, 175–178.
- Solomon, S., D. Qin, and Coauthors, 2007: *Climate change 2007: the physical science basis*. Cambridge University Press, Cambridge, UK and New York, NY, USA.
- Song, Q., D. B. Chelton, S. K. Esbensen, N. Thum, and L. W. O’Neill, 2009: Coupling between sea surface temperature and low-level winds in mesoscale numerical models. *J. Clim.*, **22**, 146–164.
- Song, Q., P. Cornillon, and T. Hara, 2006: Surface wind response to oceanic fronts. *J. Geophys. Res.*, **111**, C12 006.

- Stephens, G. L., T. L'Ecuyer, and Coauthors, 2010: Dreary state of precipitation in global models. *J. Geophys. Res.*, **115**, 1–13.
- Straus, D. M. and J. Shukla, 1997: Variations of midlatitude transient dynamics associated with ENSO. *J. Atmos. Sci.*, **54**, 777–790.
- Sweet, W. R., R. Fett, J. Kerling, and P. L. Violette, 1981: Air-sea interaction effects in the lower troposphere across the north wall of the Gulf Stream. *Mon. Wea. Rev.*, **109**, 1042–1052.
- Thibaux, J., E. Rogers, W. Wang, and B. Katz, 2003: A new high-resolution blended real-time global sea surface temperature analysis. *Bul. Amer. Meteorol. Soc.*, **84**, 645–656.
- Trenberth, K. E., 1999: Atmospheric moisture recycling: role of advection and local evaporation. *J. Clim.*, **12**, 1368–1381.
- Trenberth, K. E., A. Dai, R. M. Rasmussen, and D. B. Parsons, 2003: The changing character of precipitation. *Bull. Amer. Meteor. Soc.*, **84**, 1205–1217.
- Untch, A. and M. Hortal, 2004: A finite-element schemes for the vertical discretization of the semi-Lagrangian version of the ECMWF forecast model. *Quart. J. Roy. Meteor. Soc.*, **130**, 1505–1530.
- Wai, M. and S. A. Stage, 1989: Dynamical analysis of marine atmospheric boundary layer structure near the Gulf Stream oceanic front. *Quart. J. Roy. Meteor. Soc.*, **115**, 29–44.
- Wallace, J. M. and D. S. Gutzler, 1981: Teleconnections in the geopotential height field during the Northern Hemisphere winter. *Mon. Wea. Rev.*, **109**, 784–812.
- Warner, T. T., M. N. Lakhtakia, J. D. Doyle, and R. A. Pearson, 1990: Marine atmospheric boundary layer circulations forced by Gulf Stream sea surface temperature gradients. *Mon. Wea. Rev.*, **118**, 309–323.
- Wettstein, J. J. and J. M. Wallace, 2010: Observed patterns of month-to-month storm track variability and their relationship to the background flow. *J. Atmos. Sci.*, **67**, 1420–1437.

- Wilby, R. L. and T. M. L. Wigley, 2002: Future changes in the distribution of daily precipitation totals across North America. *Geophys. Res. Lett.*, **29**, 1135.
- Xie, S. P., 2004: Satellite observations of cool ocean-atmosphere interaction. *Bull. Amer. Meteor. Soc.*, **85**, 195–208.
- Yang, X. and E. K. M. Chang, 2006: Variability of the Southern Hemisphere winter split flow: A case of two-way reinforcement between mean flow and eddy anomalies. *J. Atmos. Sci.*, **63**, 634–650.
- Yang, X. and E. K. M. Chang, 2007: Eddy zonal flow feedback in the Southern Hemisphere winter and summer. *J. Atmos. Sci.*, **64**, 3091–3112.
- Zhang, X., F. W. Hederl, and Coauthors, 2007: Detection of human influence on twentieth-century precipitation trends. *Nature*, **448**, 461–465.
- Zhang, Y. and I. M. Held, 1999: A linear stochastic model of a GCM's midlatitude storm tracks. *J. Atmos. Sci.*, **56**, 3416–3435.
- Zhu, J., B. Huang, and Coauthors, 2015: ENSO prediction in Project Minerva: Sensitivity to atmospheric horizontal resolution and ensemble size. *J. Clim.*, **28**, 2080–2095.

## Curriculum Vitae

Xuelei Feng received his Bachelor in the field of Applied Meteorology from Lanzhou University in 2004. Then, he was employed as a Research Assistant in China Institute for Radiation Protection (CIRP), Taiyuan, Shanxi Province, China. In 2010, he came to United States to pursuit his Ph.D. in Climate Dynamics, George Mason University.